UNIVERSIDADE
BEIRA INTERIOR

Development of RNA-based nanoparticles for cancer therapy

Versão final após defesa

Pedro Miguel Baltazar Simões

Dissertação para obtenção do Grau de Mestre em
Ciências Biomédicas
(2º ciclo de estudos)

Orientadora: Prof.ª Doutora Carla Patrícia Alves Freire Madeira da Cruz
Co-orientadora: Prof.ª Doutora Cândida Ascensão Teixeira Tomaz
Co-orientadora: Mestre Jéssica Lopes Nunes

janeiro de 2023

Declaração de Integridade

Eu, Pedro Miguel Baltazar Simões, que abaixo assino, estudante com o número de inscrição M10729 do 2º ciclo de estudos de mestrado em Ciências biomédicas, declaro ter desenvolvido o presente trabalho e elaborado o presente texto em total consonância com o **Código de Integridades da Universidade da Beira Interior**.

Mais concretamente afirmo não ter incorrido em qualquer das variedades de Fraude Académica, e que aqui declaro conhecer, que em particular atendi à exigida referenciação de frases, extratos, imagens e outras formas de trabalho intelectual, e assumindo assim na íntegra as responsabilidades da autoria.

Universidade da Beira Interior, Covilhã 03/01/2022

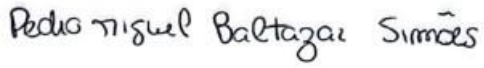

(assinatura conforme Cartão de Cidadão ou preferencialmente
assinatura digital no documento original se naquele mesmo formato)

Agradecimentos

A elaboração da dissertação de mestrado foi mais um grande objetivo concluído na minha vida e além disso um dos maiores desafios com que me deparei até hoje. Por estemotivo estou extremamente grato pela contribuição e toda a ajuda de todos aqueles queme acompanharam nesta jornada.

Em primeiro lugar, gostaria de agradecer à minha orientadora, a professora doutora Carla Cruz. Foi durante a licenciatura que conheci e comecei a trabalhar com a professora, e foi a primeira pessoa que me ajudou a despertar o gosto pela investigação. Muito obrigado por ter aceitado orientar-me e agradeço também pela confiança, paciência e tempo que despendeu para me auxiliar e por não me fazer baixar os braços quando tudo corria menos bem.

Quero agradecer também às minhas co-orientadoras, a Professora Doutora Cândida Tomaz e à Jéssica Nunes por toda a ajuda, sem a qual não seria possível realizar este trabalho. Obrigado também por toda a ajuda, paciência e por todos os ensinamentos que foram fulcrais para o desenvolvimento deste trabalho.

À Universidade da Beira Interior e ao Centro de Investigação em Ciências da Saúde pela disponibilização de todas as condições necessárias à realização desta dissertação.

Agradeço a todos os colegas de laboratório, à "G4 team", que sempre me ajudaram ao longo deste percurso e partilharam comigo o seu conhecimento e experiências no laboratório. Fora de trabalho, agradeço por todas as gargalhadas e momentos inesquecíveis que passámos juntos.
A todos os meus amigos, àqueles que sempre cá estiveram para tudo, um grande obrigado por todo o apoio.
Finalmente, deixo um agradecimento muito especial aos meus pais, irmão, avós e namorada, por todo o apoio, incentivo, paciência e motivação diária. Nunca me irei esquecer de vocês e obrigado por tudo o que têm feito por mim!

Muito obrigado a todos!

Resumo

O cancro oral é cada vez mais reconhecido como duas doenças distintas, o cancro da boca e da orofaringe. A sua incidência e mortalidade estão a aumentar, e espera-se no ano de 2040 553000 novos casos e um total de 263000 mortes, em todo o mundo. As opções terapêuticas dependem do estadio da doença, da localização do tumor, dos resultados cosméticos e funcionais, da idade, doenças associadas, entre outras. Para cancros em estadios iniciais, a terapia mais comum é a cirurgia, com o intuito de remover as camadas superiores de tecido maligno. Em fases mais avançadas, e quando ainda não existe metastização, as terapias mais utilizadas são a cirurgia e a radioterapia, isoladamente ou combinadas. Nos casos em que já ocorreu metastização, é usada uma abordagem combinada, integrando cirurgia e radioterapia com ou sem quimioterapia. Para alguns doentes, a imunoterapia, isolada ou com quimioterapia, pode ser uma opção. Embora existam várias opções terapêuticas, nenhuma delas é completamente eficaz e, além disso, existem vários efeitos secundários negativos associados. Para ultrapassar estas limitações, têm sido desenvolvidos sistemas de entrega de fármacos dirigidos para um determinado alvo com o intuito de melhorar a eficácia da entrega destas moléculas nas células cancerígenas.

Assim, nesta dissertação, procedeu-se à sintetese, caracterização e avaliação do potencial biológico de nanopartículas, nomeadamente lipossomas e nanopartículas de ouro, revestidas com RNA, para a entrega seletiva dos ligandos C_8, e dexametasona, às células do cancro oral.

Em primeiro lugar, a estrutura do RNA e a sua interação com os ligandos C_8, dexametasona e a proteína nucleolina (NCL) foram avaliadas por CD, TDS, NMR e titulações por fluorescência. Os ensaios biofísicos evidenciaram que o RNA adota uma estrutura em hairpin e duplex e que os ligandos C_8 e dexametasona não estabilizaram a sua estrutura. Foi também demonstrado que o RNA interage e tem um K_D para a proteína NCL de 1.8×10^{-6} M, e que a afinidade aumenta com a adição de C_8 e dexametasona, com um efeito mais pronunciado por parte do ligando C_8.

Seguidamente foram produzidas e caracterizadas as nanopartículas de ouro e lipossomas revestidos com RNA. As nanopartículas de ouro e os lipossomas funcionalizados apresentaram um tamanho próximo de 20 nm e 160 nm, respetivamente, como observado pela técnica de DLS. As técnicas de PAGE e NMR mostraram que os lipossomas e nanopartículas de ouro foram efetivamente revestidos com o RNA. Além disso, a espetroscopia UV-vis revelou que os ligandos C_8 e dexametasona foram encapsulados nos lipossomas.

Por último, foram avaliados os efeitos in vitro das nanopartículas de ouro e lipossomas revestidos com RNA e que carregam os ligandos C_8 e dexametasona na linha celular do cancro oral (SCC-154) versus células saudáveis (NHDF). Foi também avaliada a capacidade de internalização do RNA em células do cancro oral. Pelo ensaio de MTT, os lipossomas funcionalizados com RNA e que carregam C_8, ou dexametasona, apresentaram uma redução significativa na viabilidade celular das células malignas SCC-154, mantendo ao mesmo tempo viáveis as células não malignas NHDF. Relativamente aos ensaios de microscopia de fluorescência confocal, os resultados provaram que o RNA foi capaz de internalizar a maioria das células SCC-154 após 2 h de incubação, e localizando-se principalmente no núcleo e citoplasma das células. Verificou-se também que o RNA não internalizou as células através da NCL.

Resumidamente, os resultados obtidos nesta dissertação podem contribuir para o desenvolvimento de novos sistemas de administração de fármacos para uma terapia do cancro oral orientada de forma sustentada e eficaz.

Palavras-chave

Cancro oral; Lipossomas; Nanopartículas de ouro; RNA; Nanossistemas de entrega de fármacos; Nucleolina

Resumo Alargado

O cancro oral é cada vez mais reconhecido como duas doenças distintas, o cancro da boca e da orofaringe. A sua incidência e mortalidade estão a aumentar, e espera-se no ano de 2040 553000 novos casos e um total de 263000 mortes, em todo o mundo. O cancro oral pode ter diferentes estadios, nomeadamente tumor primário que não pode ser avaliado (Tx), nenhum tumor primário (T0), carcinoma in situ (Tis), um tumor com 0-2 cm na maior dimensão e profundidade de invasão (DOI) ≤ 5 mm (T1), tumor com 2-4 cm na maior dimensão e DOI ≤ 10 mm (T2), tumor>4 cm na maior dimensão e DOI ≥ 10 mm (T3), tumor que invade estruturas adjacentes como osso cortical e músculo profundo da língua (T4a) e um tumor muito avançado com diversas metástases (T4b). As opções terapêuticas dependem do estadio da doença, da localização do tumor, da idade, doenças associadas, entre outras. Para cancros em estadios iniciais, a terapia mais comum é a cirurgia, com o intuito de remover as camadas superiores de tecido maligno. Em fases mais avançadas, e quando ainda não existe metastização, as terapias mais utilizadas são a cirurgia e a radioterapia, isoladamente ou combinadas. Nos casos em que já ocorreu metastização, é usada uma abordagem combinada, integrando cirurgia e radioterapia com ou sem quimioterapia. Para alguns doentes, a imunoterapia, isolada ou com quimioterapia, pode ser uma opção. Embora existam várias opções terapêuticas, nenhuma delas é completamente eficaz e, além disso, existem vários efeitos secundários negativos associados. A cirurgia tem vários efeitos secundários, tais como dor, possibilidade de infeção pós-operatória, perda da função dos órgãos, hemorragia, formação de coágulos sanguíneos, além da elevada invasividade associada. Na quimioterapia, um dos maiores problemas é a falta de seletividade das células cancerígenas, porque os agentes terapêuticos também têm efeito citotóxico semelhante nas células saudáveis, causando toxicidade grave a estes tipos de células devido ao seu elevado volume de distribuição. A má solubilidade em água das moléculas é também outro problema, levando à embolização dos vasos sanguíneos quando administrados intravenosamente. A radioterapia também tem vários efeitos secundários, uma vez que a radiação não só mata ou retarda o crescimento do cancro, como também pode afetar as células saudáveis mais próximas. Alguns dos efeitos secundários relatados incluem fadiga, náuseas, vómitos, inchaço e problemas de fertilidade. A imunoterapia pode também causar alguns efeitos secundários, tais como, contagens sanguíneas reduzidas, que podem levar à anemia. Outros efeitos secundários incluem problemas de pele e do trato gastrointestinal, insuficiência renal e menos frequentemente pneumonite. Para ultrapassar estas limitações, têm sido desenvolvidos sistemas de entrega de fármacos

dirigidos para um determinado alvo com o intuito de melhorar a eficácia da entrega destas moléculas nas células cancerígenas.

Assim, nesta dissertação, procedeu-se à síntese, caracterização e avaliação do potencial biológico de nanopartículas, nomeadamente lipossomas e nanopartículas de ouro, revestidas com RNA, para a entrega seletiva dos ligandos C_8, e dexametasona, às células do cancro oral.

Em primeiro lugar, a estrutura do RNA e a sua interação com os ligandos C_8, dexametasona e a proteína nucleolina (NCL) foram avaliadas por CD, TDS, NMR e titulações por fluorescência. Os ensaios biofísicos evidenciaram que o RNA adota uma estrutura em hairpin e duplex e que os ligandos C_8 e dexametasona não estabilizaram a sua estrutura. Foi também demonstrado que o RNA interage e tem um K_D para a proteína NCL de 1.8×10^{-6} M, e que a afinidade aumenta com a adição de C_8 e dexametasona, com um efeito mais pronunciado por parte do ligando C_8.

Seguidamente foram produzidas e caracterizadas as nanopartículas de ouro e lipossomas revestidos com RNA. As nanopartículas de ouro e os lipossomas funcionalizados apresentaram um tamanho próximo de 20 nm e 160 nm, respetivamente, como observado pela técnica de DLS. As técnicas de PAGE e NMR mostraram que os lipossomas e nanopartículas de ouro foram efetivamente revestidos com o RNA. Além disso, a espetroscopia UV-vis revelou que os ligandos C_8 e dexametasona foram encapsulados nos lipossomas.

Por último, foram avaliados os efeitos in vitro das nanopartículas de ouro e lipossomas revestidos com RNA e que carregam os ligandos C_8 e dexametasona na linha celular do cancro oral (SCC-154) versus células saudáveis (NHDF). Foi também avaliada a capacidade de internalização do RNA em células do cancro oral. Pelo ensaio de MTT, os lipossomas funcionalizados com RNA e que carregam C_8, ou dexametasona, apresentaram uma redução significativa na viabilidade celular das células malignas SCC-154, mantendo ao mesmo tempo viáveis as células não malignas NHDF. Relativamente aos ensaios de microscopia de fluorescência confocal, os resultados provaram que o RNA foi capaz de internalizar a maioria das células SCC-154 após 2 h de incubação, e localizando-se principalmente no núcleo e citoplasma das células. Verificou-se também que o RNA não internalizou as células através da NCL.

Resumidamente, os resultados obtidos nesta dissertação podem contribuir para o desenvolvimento de novos sistemas de administração de fármacos para uma terapia do cancro oral orientada de forma sustentada e eficaz.

Abstract

Oral cancer is increasingly recognized as two distinct diseases, mouth and oropharyngeal cancer. Its incidence and mortality are increasing, and it is expected in the year of 2040 a number of 553000 new cases and a total of 263000 deaths, worldwide. Treatment options depend on the stage of cancer, the location of the tumor, patient age, associated illnesses, among others. The most common therapy for oral cancers in early stages is surgery, to remove the top layers of malignant tissue. In more advanced stages, when there is still no metastasis, the most used therapies are surgery and radiotherapy, either used alone or combined. When the cancer has already spread to other parts of the body, a combined modality approach integrating surgery, and radiotherapy with or without chemotherapy is the golden choice. For some patients, immunotherapy, alone or with chemotherapy can be also an option. Although there are several therapeutic options, none of them are completely effective and in addition, there are several side effects associated with the therapies. To overcome these limitations, researchers have been trying to reduce these drawbacks by using drug delivery systems that carry drugs to be delivered at cancer cells.

In this dissertation, we synthesized, characterized, and evaluated the biological potential of nanoparticles, namely liposomes and gold nanoparticles, coated with a RNA to selectively deliver the ligands C_8, and dexamethasone, to oral cancer cells.

Firstly, the RNA structure and binding interaction between the RNA sequence and ligands C_8, dexamethasone and nucleolin (NCL) were evaluated by CD, TDS, NMR and fluorescence titrations. The biophysical assays evidenced the formation of an RNA hairpin and duplex structure and the ligands C_8 and dexamethasone did not stabilize this structure. It was also shown that the RNA interacts and has a K_D to NCL of 1.8×10^{-6} M, which increases with the addition of C_8 and dexamethasone, and C_8 showing a more pronounced effect.

Then, RNA-coated gold nanoparticles and liposomes were produced and characterized. The functionalized gold nanoparticles and liposomes presented a size close to 20 nm and 160 nm, respectively, as observed by the DLS technique. The PAGE and NMR techniques showed that the liposomes were effectively coated with the RNA. Additionally, the UV-vis spectroscopy revealed that the ligands C_8 and dexamethasone were efficiently encapsulated in the liposomes.

Finally, in vitro effects on oral cancer cell line (SCC-154) versus healthy cells (NHDF) of RNA gold nanoparticles and liposomes loading the ligands C_8 and dexamethasone and the capacity of internalization of the RNA on oral cancer cells were evaluated. By MTT

assay the RNA functionalized liposomes loaded with C_8, or dexamethasone presented a significant reduction in the cell viability of malignant SCC-154 cells, while maintaining viable the non-malignant NHDF cells. With respect to the confocal fluorescence microscopy assays, the results proved that the RNA was able to internalize the majority of SCC-154 cells after 2 h of incubation, and mainly localize the nucleus and cytoplasm of cells. We also verified that the RNA did not internalize cells via NCL.
Overall, the results obtained in this dissertation can contribute to the development of new drug delivery systems for sustained and effective targeted oral cancer therapy.

Keywords

Oral cancer; Drug Delivery Systems; Liposomes; Gold Nanoparticles; RNA; Nucleolin

Index

List of Figures

List of Tables

List of Acronyms

5-FU	Fluoropyrimidine 5-fluorouracil
AF	Ammonium ferrothiocyanate
AFM	Atomic force microscopy
C_8	10-(8-(4-iodobenzamide) octyl)-3,6-bis (dimethylamine) acridinium iodide
CD	Circular dichroism
CIS	Cisplatin
CLL	Chronic lymphocytic leukemia
CHOL	Cholesterol
CXCL12	C-X-C chemokine ligand 12
D_2O	Deuterium oxide
DEPC	Diethyl pyrocarbonate
DLS	Dynamic light scattering
DMSO	Dimethyl sulfoxide
DNA	Deoxyribonucleic acid
DOX	Doxorubicin
DSC	Differential scanning calorimetry
DSPE-PEG	1,2- distearoyl-sn-glycero-3-phosphoethanolamine-N-[amino(polyethyleneglycol)-2000]
DTX	Docetaxel
EGFR	Anti-epithelial growth factor receptor
ESR	Electron spin resonance
FBS	Fetal bovine serum
Fc	Constant fragment
FDA	Food and drug administration
FFF	Field-Flow Fractionation
FITC-NHS	Fluorescein-5-EX N-hydrooxy-succinimide ester
FTIR	Fourier transform infrared spectroscopy
G4	G-quadruplex
GC-MS	Gas chromatography-mass spectroscopy
GUV	Giant unilamellar vesicle
$HAuCl_4$	Chloroauric acid
HPLC	High-performance liquid chromatography
HPV	Human papillomavirus

HSA	Human serum albumin
HSQC	Heteronuclear single quantum coherence
IL-8	Human interleukin-8
KCl	Potassium chloride
LC-MS	Liquid chromatography-mass spectroscopy
LDE	Laser Doppler electrophoresis
LUV	Large unilamellar vesicle
MDR1	Multidrug resistance gene 1
MLV	Multilamellar vesicle
MMP-9	Matrix metalloproteinase-9
MPA	3-mercaptopopionic acid
MSNPs	Mesoporous silica nanoparticles
MTT	(3-(4,5-Dimethylthiazol-2-yl)-2,5-Diphenyltetrazolium bromide
MTX	Methotrexate
MVV	Multivesicular vesicle
NaCl	Sodium chloride
NCL	Nucleolin
NMR	Nuclear magnetic resonance
NTA	Nanoparticle tracking analysis
OD	Optical density
OSCC	Oral squamous cell carcinoma
PAGE	Polyacrylamide gel electrophoresis
PCL	Polycaprolactone
PCR	Polymerase Chain Reaction
PDEA	2-(2-pyridinyldithio)ethaneamine hydrochloride
PDI	Polydispersity index
PEG	Polyethylene Glycol
PEI	Polymerpolyethylenimine
PG	1,2,-distearoyl-sn-glycero-3-phospho-(1´-rac-glycerol) (sodium salt)
PTX	Paclitaxel
Rb	Retinoblastoma
RNA	Ribonucleic acid
RNA-FITC	FITC-NHS labeled RNA-SH
RNA-SH	Reduced RNA
RT-PCR	Reverse Transcription Polymerase Chain Reaction
SAHA	Suberoylanilide hydroxamic acid
SAXS	Small-angle X-ray scattering

SCC	Squamous cell carcinoma
SEC	Size exclusion chromatography
SELEX	Systematic evolution of ligands by exponential enrichment
SEM	Scanning electron microscopy
SPR	Surface plasmon resonance
STD	Saturation transfer difference
SUV	Small unilamellar vesicle
TAE 1x	1× tris-acetate-EDTA
TCEP	Tris(2-carboxyethyl)phosphine hydrochloride
TDS	Thermal Difference Spectrum
TEM	Transmission electron microscopy
TGA	Thermogravimetric analysis
TiO_2	Titanium dioxide
T_m	Melting temperature
UCNs	Up-conversion nanoparticles
ULV	Unilamellar vesicles
UPLC	Ultra-performance liquid chromatography
UV-vis	Ultraviolet-visible
VEGF	Vascular endothelial growth factor
XRD	X-Ray diffraction

Chapter 1

1. Introduction

Cancer is defined as an uncontrolled abnormal cell division, replicative immortality, and resistance to death, that can arise as a consequence of spontaneous or environmentally induced mutation [1], [2]. GLOBOCAN 2020 estimated more than 19 million new cases and almost 10 million deaths worldwide for the year 2020 [3].

The most common types of cancer are breast, lung, colorectum, prostate, and stomach cancers [3]. Despite not being in the top five of the most common, oral cancer is one of the world's most incident and mortal cancers [4].

Therefore, oral cancer is a serious problem that affects the health of human societies and new therapeutic approaches are necessary to fight this disease.

1.1 Oral Cancer

The definition of oral cancer is still not consensual, and it is essential to define the location, morphology, and behavior of the tumor to characterize this disease. However, oral cancer is increasingly recognized as two distinct diseases, oral cavity cancer (mouth cancer) and oropharyngeal cancer (throat cancer) [5]. Most oral cancers are carcinomas with squamous differentiation arising from the mucosal epithelium, called oral squamous cell carcinoma (OSCC) [5].

Oral cancer incidence and mortality are increasing, and it is expected in the year of 2040 a number of 553000 new cases and a total of 263000 deaths, worldwide [6].

The most common site for intraoral cancer is the tongue, which accounts near 40% of all cases of oral cancer. Tongue cancers mostly occur on the posterior-lateral border and ventral surfaces of the tongue. Less common locations of oral cancer include the floor of the mouth (30% of cases), gingival, buccal mucosa, labial mucosa and hard plate [7], [8]. The most important structures of oral cavity are presented in Figure 1.

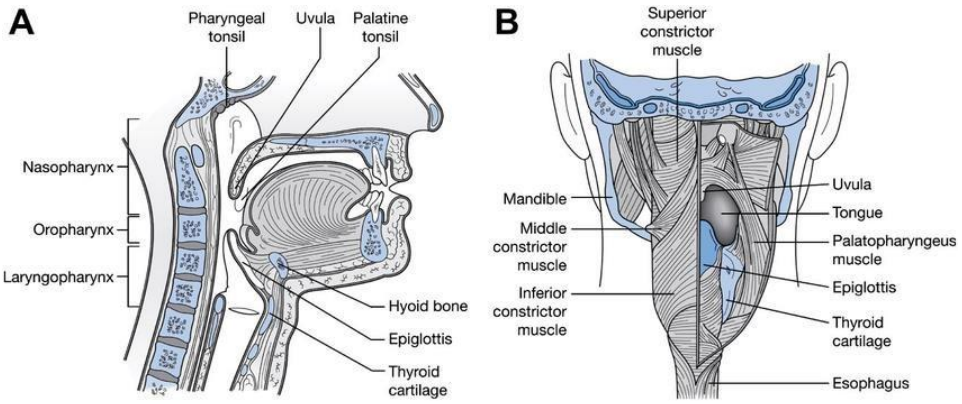

Figure 1 – Anatomy and structures of the oral cavity in A) the lateral view and B) posterior view. Used with permission from "Atlas of Clinical Gross Anatomy" by Kenneth Moses et al. Elsevier; 2005. ISBN 0323037445 P104, Fig 10.1 Divisions of the pharynx P105, Fig 10.3 Posterior view of the pharynx.

Oral carcinogenesis, represented in Figure 2, is a highly complex multifactorial process that occurs when epithelial cells are affected by various genetic alterations, leading to deregulation of cell proliferation and death. The genetic alterations include gene amplification, oncogene overexpression, mutations, deletions, and hypermethylation, leading to the inactivation of tumor suppressor genes, like p53 and p16, which are involved in the maintenance of genomic stability, cell cycle progress, cellular differentiation, deoxyribonucleic acid (DNA) repair, and apoptosis. Additionally, several oral tumors have been confirmed to have the expression of telomerase, which is strongly associated with malignancy in oral tissues. Telomerase activity has been identified in 80% of oral cancer patients, and it has been reported that most immortal oral cancer cell lines have high levels of telomerase and also have tumor radioresistance [9]–[11].

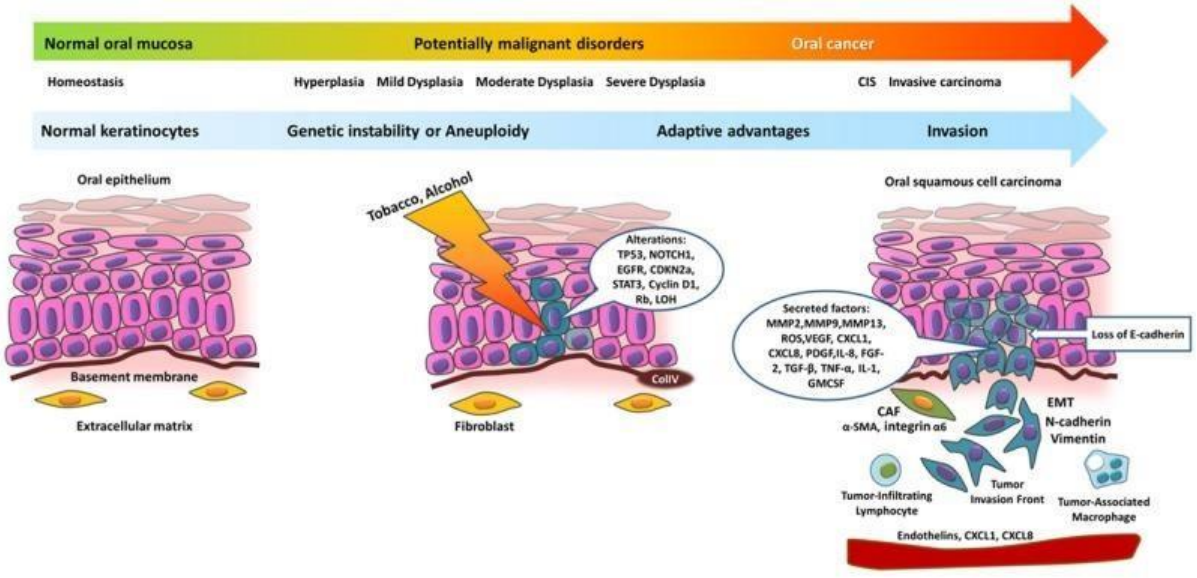

Figure 2 - Oral Cancer Development process. Adapted from [9].

The two main risk factors that influence oral cancer development are genetic and epigenetic factors. The development of oral cancer is influenced by both factors, being the most important tobacco and alcohol consumption, epigenetic factors that together have a synergistic effect, increasing the risk of developing oral cancer. There are other important risk factors, namely diet and nutrition, viruses, radiation, ethnicity, familial and genetic predisposition, oral thrush, immunosuppression, use of mouthwash, syphilis, dental factors and occupational risks[7], [12]. Human papillomavirus (HPV) is the most common virus associated with oral cancer.HPV is a DNA virus and epitheliotropic especially for squamous epithelia, present in the oral cavity. HPVs types 16, 18, 31, 33, 35 and 39 are the most associated with the development of oral premalignant lesions. HPV E6 and E7 proteins are capable of disturbing the cell cycle machinery, binding and destroying p53 and retinoblastoma (Rb) tumor suppressor genes, respectively, leading to loss of control on DNA replication, DNA repair and apoptosis [7].

After the onset of oral cancer, early carcinomas often go unnoticed because patients are asymptomatic. With the progression of the disease, the main symptom is pain and other symptoms include ear pain, bleeding, mobility of teeth, breath problems, difficulty in speech, dysphagia and problems using a prosthesis, trismus and paraesthesia [11].

Oral cancer diagnosis comprises a physical exam, which includes a close exam of the roof and floor of the mouth, the back of the throat, tongue, cheeks, and lymph nodes in the neck. If a tumor, or suspicious lesion is found, a brush biopsy or a tissue biopsy is performed. In addition, other tests can be performed, namely, X-rays, computerized tomography scans, positron emission tomography scans, magnetic resonance imaging and endoscopy [13]. Most patients with oral cancer are diagnosed with tumors already in an advanced stage and incur significant morbidity and mortality [14].

Oral cancer can have different stages, namely primary tumor that cannot be evaluated (Tx), no primary tumor (T0), carcinoma in situ (Tis), a tumor with 0-2 cm in greatest dimension and depth of invasion (DOI) ≤ 5 mm (T1), tumor with 2-4 cm in greatest dimension and DOI ≤ 10 mm (T2), tumor>4 cm in greatest dimension and DOI ≥ 10 mm (T3), tumor that invades adjacent structures like cortical bone and deep muscle of tongue (T4a) and a very advanced tumor with diverse metastasis (T4b) [15]. Treatment options depend on the stage of cancer, the location of the tumor, cosmetic and functional outcomes, age of the patient, associated illnesses, patient´s preference, and availability of expertise. For oral cancers in stage T0 and Tis, the most common therapy is surgery, to remove the top layers of malignant tissue. In stages T1 and T2, the most used therapies are surgery and radiotherapy, either used alone or combined. In stages T3 and T4, a combined modality approach integrating surgery, and

radiotherapy with or without chemotherapy is the golden choice. For some patients, immunotherapy, alone or with chemotherapy can be an option [16].

Currently, there are several drugs that are applied in oral cancer therapy. In chemotherapy are commonly used paclitaxel (PTX), cisplatin (CIS), doxorubicin (DOX), docetaxel (DTX), methotrexate (MTX) and fluoropyrimidine 5-fluorouracil (5-FU) [17]. PTX is usually administered intravenously and acts by cellular growth inhibition. Its distribution throughout the body is very extensive, causing severe side effects [17], [18]. CIS is a chemotherapeutic agent that causes apoptosis of cancer cells by interfering with DNA repair mechanisms and causing its damage. CIS administration is associated with severe side effects such as renal failure [17], [18]. DOX is a potent anticancer agent mainly due to its ability to rapidly target dividing cells, both cancerous and non-cancerous, causing severe side effects, such as, cell death in major organs, namely in heart, brain, liver and kidney [17], [18]. DTX is an anticancer drug used in chemotherapy and is a folate antagonist which inhibits synthesis of purines and pyrimidines, causing the inhibition of cancer cells proliferation [17], [18]. MTX is an antimetabolite agent and its oral administration causes low systemic bioavailability and is associated with significant side effects like diarrhea, ulcerative stomatitis, hemorrhagic enteritis and gastrointestinal perforation [17], [18]. 5-FU causes cancer cells death by inhibiting or interfering with the synthesis of DNA or ribonucleic acid (RNA) [17], [18].

Although there are several therapeutic options, none of them are completely effective and in addition, there are several negative side effects associated with the therapies. Cancer surgery has several side effects, such as pain, possibility of post-operative infection, loss of organ function, bleeding, formation of blood clots in addition to the associated high invasiveness [19]. In chemotherapy, one of the major problems is the lack of selectivity to cancer cells, because therapeutic agents also have similar cytotoxic effects on healthy cells, causing severe toxicity to these types of cells due to high volume of distribution of these drugs, which have low molecular weights and are rapidly cleared from human system [20]. Poor solubility in water of the molecules is also another problem, leading to embolization of blood vessels when administered through intravenous form [20]. Radiotherapy also has several side effects since radiation not only kills or slows the growth of cancer but can also affect nearby healthy cells [21]. Some reported side effects include fatigue, nausea, vomiting, swelling and fertility problems [21]. Immunotherapy can also cause some side effects, such as, lowered blood counts, that can lead to anemia [22]. Other side effects include skin and gastrointestinal tract problems, kidney failure and less often pneumonitis [22].

More recently, researchers have been trying to reduce these drawbacks by using drug delivery systems that carry drugs and can deliver with higher efficacy these molecules at cancer cells [23].

1.2 Targeted Drug Delivery Systems

A drug delivery system is usually composed of three basic units: the nanocarrier, the targeting molecule and the drug [18].

1.2.1 Nanocarriers

Nanocarriers present unique characteristics, namely enhanced biodistribution, pharmacokinetics, stability, solubility, reduction in toxicity and sustained and targeted drug delivery [24]. There are different types of nanocarriers, but they are generally grouped into three major groups, organic, inorganic, and hybrid nanocarriers. Organic nanocarriers include nanoparticles such as solid lipid, liposomes, dendrimers, polymeric, micelles, and viral nanocarriers. Inorganic nanocarriers include gold, magnetic, quantum dots and mesoporous silica nanocarriers. Hybrid nanocarriers combine two or more organic and inorganic nanocarriers together or individually. Some examples and characteristics of nanocarriers from the different groups are summarized in Table 1 [24].

Table 1 – Methods of synthesis, size, properties, and applications of different nanocarriers. Adapted from [24],[25],[34].

	Nanocarrier	Method of Synthesis	Size of carrier (nm)	Properties	Applications
Organic nanocarriers	Solid lipid nanocarriers	High shear homogenization, hot homogenization, cold homogenization, solvent emulsification, microemulsion, spray drying	50-100	Colloidal carrier, better stability, ease of upgradeability, biodegradability, low drug loading capacity, burst release	Drug delivery to liver cells, gene vector carrier, topical use, delivery to solid tumors, antitubercular chemotherapy
	Liposome	Thin film hydration, reverse phase evaporation, solvent injection, detergent removal, mechanical dispersion	25-2500	Phospholipid bilayer vesicle, biocompatibility, biodegradability, less toxicity	Trap hydrophilic and hydrophobic drug, optimal delivery of biologically active agent
	Dendrimer	Cascade reaction, convergent and divergent approach, self-assembly	1-10	Radially symmetric, homogenous, well defined, monodisperse hyperbranched molecules	Drug delivery, liver targeting, photodynamic therapy, neutron capture therapy, imaging, gene delivery
	Polymeric nanocarriers	Solvent evaporation, emulsification/solvent diffusion, nanoprecipitation, salting out, supercritical fluid technology, dialysis, polymerization	10-100	Effective cell membrane permeation, stability in blood stream, biodegradability	High concentration of drug delivery, active and passive drug delivery, maintains stability of volatile pharmaceutical agent
	Micelle	Supramolecular self-assembly, solvent/mechanical dispersion	10-100	Biostability, dynamic system, colloidal aggregate of amphiphilic molecule	Encapsulate either hydrophobic or hydrophilic drug
	Carbon tubes	Chemical vapour deposition, laser ablation, carbon arc discharge	0.4-3	Hexagonal pattern, crystalline, third allotropic carbon sheet, single or multi-layer, dynamic strength, unique electrical and elastic property	Gene and drug delivery, peptide delivery, artificial implants, tissue engineering, cancer cell identification
	Gold Nanoparticle (AuNP)	Two phase synthesis, biphasic reduction, micro and ultrasonic waves, laser ablation	1-100	Multi-surface functionality, versatility, excellent biocompatibility, less toxicity, surface plasmon resonance property, fluorescence resonance energy transfer phenomenon	Biosensing, functionalized AuNP improve drug delivery, imaging
	Magnetic nanocarriers	Metal alkoxide hydrolysis, coprecipitation in microemulsion, hydroxide coprecipitation,	1-100	Superparamagnetism, chemical stability, high colloidal stability, magnetic moment	Magnetic separation, magnetic resonance imaging, targeted drug

Inorganic Nanocarriers		glycothermal synthesis, citrate gel process, glass crystallization			delivery, hyperthermia, magnetic fluid, biosensing, thermal ablation
	Quantum Dot	X-Ray Lithography, molecular beam epitaxy, e-beam litography, ion implantation, self-assembly followed by chemical reduction	2-10	Unique electronic properties, luminescence characteristics, narrow emission spectra, continuous absorption spectra, light stability	Tracking macromolecules, labelling cells and organelles, bioimaging, biomarker detection
	Mesoporous Silica	Solid-gel method, self-assembly, hard and soft templating, aerogel approach, dissolving-reconstruction method	1-100	Hundreds of pores with honey-comb structure, biocompatibility, high loading capacity, thermal and chemical stability, controllable pore, high drug payload, versatility for drug loaded with hydrophilic and lipophilic characteristics	Sustained drug delivery, peptides, and protein delivery
Hybrid nanocarriers	Organic and inorganic nanocarriers	Miniemulsion copolymerization, nanoencapsulation, hydrolysis and condensation, spray pyrolysis, supercritical fluid-assisted metho	1-100	Enhanced chemical and physical properties based on nanostructure and spatial distribution of components	Synergetic therapy, targeted drug deliver, biosensing, imaging

1.2.2 Liposomes and Gold Nanoparticles

Liposomes and gold nanoparticles are one of the most used nanocarriers, possessing interesting characteristics, such as biocompatibility and low toxicity, that make them suitable to cancer therapy, and so they were used in this dissertation. This section will focus on more detail these two types of nanocarriers.

Liposomes, represented in Figure 3**,** are defined as a colloidal spherical structure composed of lipid bilayers enclosing an aqueous core and can be used to the delivery of both hydrophobic and hydrophilic drugs [25]. According to their structure, liposomes are classified based on the number of lipid bilayers and on the vesicle size. Based on their lamellarity, liposomes can be classified as unilamellar vesicles (ULV, all size range), presenting one single bilayer, multilamellar (MLV, >500 nm), presenting two or more concentric lipid bilayers and multivesicular vesicles (MVV, >1000 nm), including several small vesicles entrapped within a single lipid bilayer. ULVs are divided in three categories, small unilamellar vesicles (SUVs, 20-100 nm), large unilamellar vesicles (LUVs, >100 nm) and giant unilamellar vesicles (GUVs, >1000 nm) [20]. Liposomes can be produced by several techniques, which can influence their final properties, such as size, lamellarity and encapsulation efficiency [25]. The most common methods include thin film hydration, reverse phase evaporation, solvent injection techniques and detergent removal. In thin film hydration method, lipids are initially dissolved in an organic solvent, generally chloroform, and dried down to form a thin lipid film. The obtained thin lipid film is then hydrated using aqueous solvent and liposomes are formed. In reverse phase evaporation technique, phospholipids are dissolved in an organic solvent to form a film and then the solvent is removed by evaporation. The film is re-dissolved in an organic solvent and hydrated by an aqueous phase, resulting in the formation of an oil-water emulsion. The mixture is sonicated to produce inverted micelles and final evaporation of the organic solvent under reduced pressure forms a viscous gel, that results subsequently into a liposomal suspension [25]. Solvent injection techniques involve the quick injection of lipids, dissolved in an organic solvent, into an aqueous medium, resulting in liposomes formation. In detergent removal method, phospholipids are solubilized with detergents at the critical micelle concentration. Then the detergent is removed by column chromatography or dialysis, and with an adequate aqueous medium, phospholipids self-assemble to liposomes [24], [25].

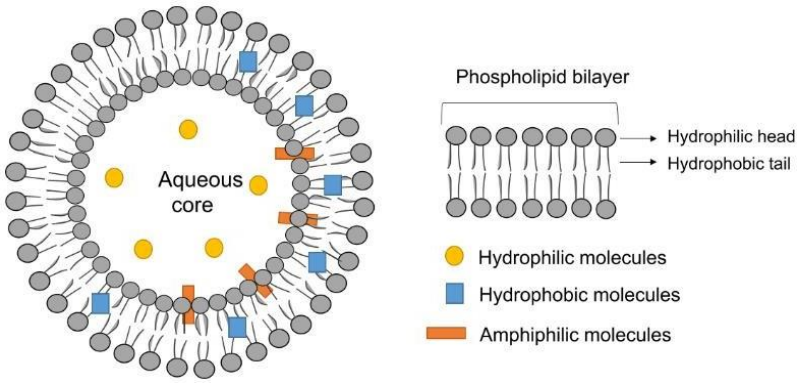

Figure 3 – Structure of liposomes. Adapted from [25].

Nowadays, liposomes have been widely used in several research as drug delivery systems due to their structural versatility, biocompatibility, biodegradability, non-toxic, non-immunogenicity nature, ability to carry large drug payloads and capacity for self-assembly [25]. Drug loaded into liposomes is protected against enzymatic, chemical and immunological degradation and fast plasma clearance, and also minimizing the exposure to healthy tissues, reducing the undesirable side effects compared with the free drug form [24]. Drugs can be loaded to liposomes by two distinct methods: passive loading method and active loading. In passive loading method the drug is encapsulated during liposome preparation. The encapsulation efficiency of drugs by this method depends on drug solubility, liposome size and charge, lipid concentration and production method [25]. Active loading method involves the creation of a transmembrane pH or ion gradient, that drives the drug through the lipid bilayer. The ideal loading efficiency is achieved when the drug is an amphipathic weak base ($pKa \leq 11$) or weak acid ($pKa > 3$). Nowadays there are several liposomal formulations approved for clinical applications. Table 2 summarizes some marketed liposomes used for cancer therapy [25].

Table 2 – Currently Marketed Liposomal Formulations for Cancer Therapy. Adapted from [25].

Product	Drug	Indication	References
Doxil	Doxorubicin	Ovarian, breast cancer, Kaposi´s sarcoma	[26]
DaunoXome	Daunorubicin	AIDS-related Kaposi´s sarcoma	[27]
Depocyt	Cytarabine/Ara-C	Neoplastic meningitis	[28]
Lipusu	Paclitaxel	Solid tumors	[29]
Mepact	Mifamurtide	Non-metastatic osteosarcoma	[30]
Marqibo	Vincristine	Acute lumphoblastic leukaemia	[31]
Myocet	Doxorubicin	Metastatic breast cancer	[32]
Onivyde	Irinotecan	Metastatic adenocarcinoma of the pancreas	[33]

Gold nanoparticles, represented in Figure 4**,** have attracted the attention of researchers due to their versatile properties and diverse applications in clinical chemistry, imaging and therapy of cancer, as well in targeted drug delivery systems [34]. There are several gold nanoparticles synthesis techniques, such as the reduction of chloroauric acid ($HAuCl_4$) by trisodium citrate at 100 ºC, forming spherical nanoparticles with a size ranging from 15 to 150 nm [34]. To obtain gold nanoparticles in different shapes, like rods, cages or tubes, the most suitable technique is based on seed-mediated growth, that consists basically in the reduction of gold salts with a strong reduction agent, leading to the production of seed particles, that are added to a solution of gold salt in the presence of a weak reducing agent and a structure directing agent, resulting in the production of gold nanoparticles in different shapes [34]. Recently, methods involving micro and ultrasonic waves, laser ablation and electrochemical and photochemical reduction as also been used to produce gold nanoparticles [34]. Gold nanoparticles have different general properties, such as size, shape, and dimensions, due to highly optimized synthesis methods [34], [35]. The size and shape of nanoparticles have a profound impact on stability, mobility, and compatibility of this nanocarriers. Gold nanoparticles designed for drug delivery on cancer should be small enough to cross physiological barriers and enter in the target cells and at the same time large enough to carry an appropriate amount of drug [35]. The physical and chemical characteristics of bulk gold,like fluorescence, electrical conductivity, or chemical reactivity, are different from the characteristics in gold nanoparticle form, with the color being the best example of this, since gold in bulk form is yellow and gold in nanoparticle is red (for particles smaller than 100 nm) or blue/purple (for bigger particles) [35]. Size of spherical gold nanoparticles also influences the cellular uptake and toxicity. It has been shown that for

gold nanoparticles with diameters in a range of 10 to 100 nm, the maximum uptake occurs for nanoparticles of 50 nm [34], [35]. Functionalization of gold nanoparticles is another key aspect besides size and shape and can be achieved either by physical adsorption or covalent attachment of ligands on the surface of the nanoparticles, usually through thiol linkages [34]. Functionalization has several advantages, providing protection against aggregation, enhanced biocompatibility, specific interactions with cells, targeted transport and accumulation in target places, increase in gold nanoparticle blood half-life time and preventing removal by cells of the mononuclear phagocytic system [34]–[36].

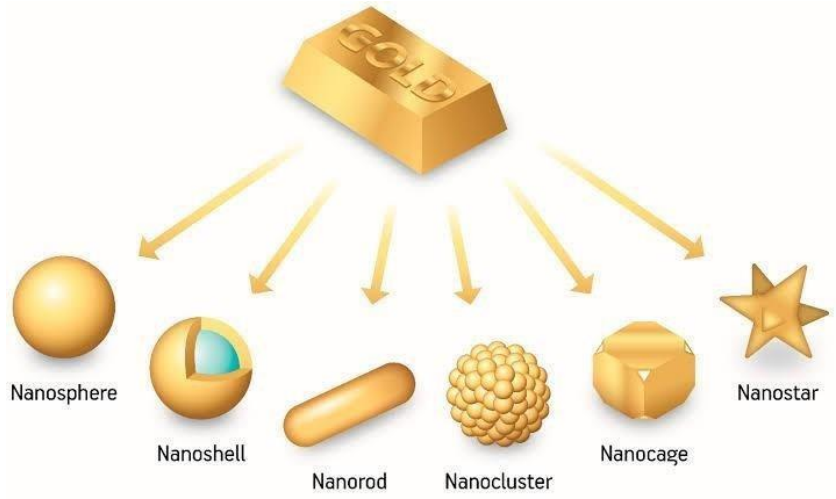

Figure 4 – Types of gold nanoparticles. Adapted from [36].

Gold nanoparticles can be used in anticancer therapy, namely in photothermal therapy, radiofrequency therapy and as drug nanocarriers. In photothermal therapy, and due to the unique properties of gold nanoparticles, such as absorption and scattering of electromagnetic radiation, gold nanoparticles can be used to the therapy of cancer [34]. This treatment strategy involves the use of electromagnetic radiation on the nanoparticles, generating thermal radiation (heat) that causes the destruction of cancer cells. Radiofrequency therapy is one of the least invasive methods currently used for cancer therapy and basically consists of promoting the damage of cancer tissue by nanoparticles heat generated by an alternating current of medium frequency [34]. As drug nanocarriers, gold nanoparticles can provide efficient transport of drugs and overcome the limitations of standard treatments, like chemotherapy [34]. Nowadays, several drugs delivered by gold nanoparticles with or without targeting molecules are being investigated for the therapy of cancer, being summarized in Table 3 [34].

Table 3 – Anticancer drug-gold nanoparticles drug delivery systems. Adapted from [34].

Nanoparticle type	Targeting Molecule	Drug	References
Spherical Gold Nanoparticle	Polyethylene Glycol (PEG), folate	Doxorubicin	[37]
	thioalkyl tetra(ethylene glycol)lyated trimethyl ammonium or thioalkyl tetra(ethylene glycol)lyated carboxylic acid doxorubicin	Doxorubicin	[38]
	PEG	Doxorubicin	[39]
	Poly(L-aspartate), PEG, folate	Doxorubicin	[40]
	PEG	Doxorubicin	[41]
	3-mercaptopopionic acid (MPA)	Daunorubicin	[42]
	PEG, tumor necrosis factor alpha	Paclitaxel	[43]
	PEG	Tamoxifen	[44]
	Not modified	Methotrexate	[45]
	Cetuximab	Gemcitabine	[46]
	Not modified	6-mercaptopurine	[47]
	photocleavable and zwitterionic thiol ligands (alkyl and tetra(ethylene glycol) components with terminally anchored 5-fluorouracyorthonitrobenzyl (ONB) group)	5-fluorouracil	[48]
	Not modified	Dodecylcysteine	[49]
	Not modified	Sulfonamide	[50]
	Not modified	Kahalalide F	[51]
	Amine-terminated oligonucleotide	Platinum (IV) complex	[52]
	Not modified	Phthalocyanine	[53]
Gold nanorods	Not modified	Rose Bengal	[54]

1.2.3 Nanosystems for Oral Cancer Therapy

After describing some examples of drug delivery systems developed for the therapy of various types of cancer, it is necessary to further explore the topic of developed nanosystems specifically for oral cancer therapy, which have been developed as an alternative method for the therapy of this disease, aiming to improve the benefits of current therapeutic agents and minimizing their cytotoxic effect on healthy cells [18].

The most common nanocarriers investigated in oral cancer therapy include gold

nanoparticles, liposomes, magnetic nanoparticles and polymeric micelles, capable of killing cancer cells by delivering therapeutic agents [10], [18].

Polymeric nanoparticles, which are composed of natural or synthetic polymers, are being used as targeted drug delivery systems for the therapy of oral cancer, due to their improved biocompatibility and drug controlled release [18]. Endo et al. developed polymeric nanoparticles based on poly(ethylene glycol)-poly(glutamic acid) block copolymer to increase the anti-tumor effects and reduce the toxicity of CIS [55]. In vitro results have shown that CIS was able to inhibit oral cancer cell lines growth (OSC-19, OSC-20, HSC-3 and HSC-4 cell lines), with 50% inhibitory concentration values lower than 30 μM [55]. The antitumor activity of the developed drug delivery system in oral carcinoma-bearing mice was 4.4–6.6-fold higher compared to the control group and the controlled release of CIS resulted in a decreased nephrotoxicity and neurotoxicity compared with administration of cisplatin in solution [55]. On the other hand, Mazzarino et al. developed polycaprolactone (PCL) nanoparticles coated with the polysaccharide chitosan for curcumin delivery into oral cavity [56]. The cytotoxic effect of these nanoparticles was evaluated in vitro using an OSCC-derived cell line, squamous cell carcinoma (SCC)-9 and showed induction of apoptosis in tumoral cells and improved curcumin bioavailability and stability [56].

Inorganic nanoparticles, composed of noble metals (e.g., gold), have been extensively used in treatment of cancer due to their lower toxicity, higher tolerance towards organic solvents, and better bioavailability compared with the free drug [18]. Sayed et al. developed anti-epithelial growth factor receptor (EGFR) antibody-conjugated gold nanoparticles for oral cancer photothermal therapy [57]. The results showed that the malignant cells required less energy to produce photothermal destruction compared to healthy cells, due to the targeting of the gold nanoparticles on the surface of EGFR-overexpressing malignant cells (JSC-313 cell line) [57]. Moreover, Lucky et al. developed up-conversion nanoparticles (UCNs) loaded with PEGylated titanium dioxide (TiO_2) conjugated with anti-EGFR-antibody for targeting EGFRs on the surface of cancer cells [58]. In vivo studies investigating anti-EGFR-PEG-TiO2-UCNs showed no toxic side effects, whereas in vitro studies using CAL-27, H596 and H460 cell lines, showed enhanced apoptosis and tumor growth inhibition [58]. Furthermore, Wang et al. developed mesoporous silica nanoparticles (MSNPs) modified by cationic polymerpolyethylenimine (PEI) to carry multidrug resistance gene 1 (MDR1)- small interfering RNA and DOX [59]. The results showed that the drug delivery system could effectively decrease gene expression of MDR1 and induce the apoptosis of human oral squamous carcinoma DOX-resistant cell line (KBV) in vitro [59].

Lipid-based nanoparticles can enhance penetration on cancer cells and provide higher stability, controlled drug release and drug protection from chemical degradation [18].

Paulo et al. developed a liposomal formulation prepared by dimyristoyl phosphatidylcholine in the presence and absence of additives such as cholesterol (CHOL) or cardiolipin to release aluminum phthalocyanine chloride, a photosensitizer, in tongue tumors induced by topic 4-nitroquinoline-1-oxide administration in Swiss mice [60]. The results showed that the liposomes induce intense necrosis in the tumor tissue accompanied by the infiltration of polymorphonuclear cells and thrombi formation on tumor-associated blood vessels [60]. As well, Muehlmann et al. produced a liposomal aluminum phthalocyanine chloride-based photodynamic therapy that inhibit the phosphatidylinositol 3-kinase/Akt/mammalian target of rapamycin (PI3K/Akt/mTOR) signaling pathway, a major regulator of cell growth, proliferation, migration, differentiation, and survival in cultured human OSCC cells (OSCC-3 cell line) [61].

Hydrogels are a mesh of hydrophilic polymeric chains dispersed in water that is swellable and can release drugs for dissolution and disintegration through the spaces in their mesh. Hydrogels are attractive for oral administration because their polymeric chains can closely interact with saliva glycoproteins, causing a mucoadhesion phenomenon [18]. Moura et al. developed a chitosan hydrogel cross-linked with glycerol phosphate disodium salt incorporating CIS [62]. Their results demonstrated that cisplatin could be quickly released with an initial burst reaching a maximum concentration at approximately 2 to 3 hours, making it attractive for the treatment of oral cancers [62]. Additionally, Li et al. have tested a system composed of a heat sensitive copolymer formed by PEG-poly(ε-caprolactone)-PEG (PECE) for the incorporation of suberoylanilide hydroxamic acid (SAHA) with CIS and evaluated the in vitro release profile of these drugs against oral carcinoma [63]. Their results demonstrated that carrier system had a sustained release of SAHA and CIS in vivo, and could improve therapeutic effects compared with a simple additive therapeutic effect of SAHA and CIS on mouse model, making it a useful method for the treatment of oral cancer and other solid tumors [63].

1.2.4 Liposomes and Gold Nanoparticles Characterization

For the characterization of gold nanoparticles and liposomes, there are several techniques that are currently used by researchers that guarantee their in vitro and in vivo performance [64]. The most investigated properties to characterize gold nanoparticles and liposomes are size and its distribution (reported using the polydispersity index (PDI)), surface charge, shape, lamellarity, phase behavior, encapsulation efficiency and in vitro drug release [25], [65].

The size and PDI are the most important characteristics in nanoparticles liposomes and gold nanoparticles characterization, and can are usually obtained by dynamic light scattering (DLS) technique [25], [65]. DLS is a simple, easy, and reliable method that analyses the continuous motion of the dispersed particles in solution, resulting in scattering of the incident light, allowing the evaluation of the mean size of the nanoparticles present in solution [25], [65]. Besides that, the PDI value reveals the degree of sample heterogeneity in terms of size, that can be monodisperse or polydisperse [25], [65]. The DLS technique also allows the determination of the surface charge, measuring the zeta potential of the nanoparticle samples. More recently, another size characterization technique, called nanoparticle tracking analysis (NTA) was also introduced to determine the size of nanoparticles in a sample [25], [65]. NTA technique is a good approach to verify the sizes determined by DLS and allows a direct estimation of particle concentration [25], [65].

The analysis of morphological characteristics, namely the shape, is necessary for an adequate characterization of liposomes and gold nanoparticles. Electron microscopy, namely scanning (SEM) and emission (TEM) electron microscopy are the most used techniques that provide a direct observation of liposomes and gold nanoparticles, respectively [64].

Lamellarity and phase behavior are characteristics that have impact only on liposomes since gold nanoparticles do not have a lipid bilayer [25]. Cryogenic-TEM is the most used method and provides useful information regarding liposome, such as their bilayer thickness [25]. The determination of transition temperature of phospholipids allows the study of phase behavior of liposomes under heating, cooling, or isothermal treatment, and can be determined by differential scanning calorimetry (DSC), which analyses the differences in heat flow, between a sample reference and a study sample [25].

Encapsulation efficiency and drug release are also important characteristics that must be evaluated in gold nanoparticles and specially in liposomes since the load of the proper amount of a drug and a controlled release is necessary to achieve therapeutic efficacy [25]. Encapsulation efficacy is often determined by ultraviolet-visible (UV-vis) and fluorescence spectroscopy [25]. Less used techniques include more sophisticate equipment such as chromatography techniques and nuclear magnetic resonance (NMR) [25]. Drug release kinetics can be studied using dialysis conditions, in which the sample is placed into the dialysis bag with an adequate molecular weight cut off and at defined time points, an aliquot of the sample is taken, and the quantity of the drug is calculated

by the methods mentioned above [25]. Table 4 summarizes the main techniques used for assessment of gold nanoparticles and liposomes characteristics [25], [65].

Table 4 – Techniques used for evaluation of gold nanoparticles and liposomes properties. Adapted from [25], [65].

Properties	Analytical Techniques
Size	DLS, NTA, NMR, Field-Flow Fractionation (FFF), Size exclusion chromatography (SEC), TEM, SEM, Cryogenic-TEM, Atomic force microscopy (AFM), visual color (in case of gold nanoparticles)
Zeta Potential	Laser Doppler electrophoresis (LDE) and Capillary electrophoresis
Shape	TEM, Cryogenic-TEM and AFM, SEM
Lamellarity	Cryogenic-TEM, ^{31}P NMR, Small-angle X-ray scattering (SAXS) and Trapped volume determination techniques
Phase Behaviour	DSC, Thermogravimetric analysis (TGA), Fluorescence probe polarization, NMR, Electron paramagnetic resonance, Fourier transform infrared spectroscopy (FTIR) and X-Ray diffraction (XRD)
Encapsulation Efficacy	UV-vis spectroscopy and Fluorescence spectroscopy, enzyme or Protein-based assays, High-performance liquid chromatography (HPLC), Ultra-performance liquid chromatography (UPLC), Liquid chromatography-mass spectroscopy (LC-MS), Gas chromatography-mass spectroscopy (GC-MS), Electron spin resonance (ESR) and ^{1}H NMR
Drug Release	Spectrophotometry methods, HPLC and UPLC

1.2.5 Aptamers: Novel Approach for Cancer Cells Targeting

Another important unit of a drug delivery system is the targeting molecule, that allows the targeting of cancer cells due to specificity to molecules that only exist in cancer cells and thus reducing the cytotoxic effect on normal cells, improving the selectivity of the delivery of therapeutic molecules to cancer cells. The targeting molecules can be antibodies, peptides, or nucleic acids. Among these molecules, some attention should be given to aptamers, namely nucleic acid aptamers, because they can function as targeting

and delivering agents that can target cancer cells, reducing side effects on other types of cells [66], [67].

Nucleic acid aptamers are DNA or RNA oligonucleotides, normally with a length of 20 to 80 bases. Aptamers fold into tertiary conformations and bind to the targets through van der Waals forces, hydrogen bonding and electrostatic interaction [25]. The binding is also done by shape complementarity. Aptamers can have different roles, namely function modulation by interfering with protein interaction with natural targets, recognition, and binding to large targets, such as proteins, cells, or entrance on target cells via receptor-mediated endocytosis upon binding to cell surface ligands [66], [67].

Although aptamers are recently being used by researchers, antibodies remain one of the most used molecules for specific target recognition. However, aptamers have several advantages when compared to antibodies [66]. Both aptamers and antibodies can be generated in vitro, but the production of aptamers via systematic evolution of ligands by exponential enrichment (SELEX) has a much lower cost [66]. Another advantage of aptamers is that once selected, they can be chemically synthesized instead of being produced in animals, bacteria or cells, like most antibodies [66], [67]. Aptamers can penetrate tumor cores more efficiently than antibodies due to their 20-25-fold smaller size compared with full-sized monoclonal antibodies. In addition to these advantages, aptamers do not have a constant fragment (Fc) region, which stimulates the response from the immune system [67]. Although aptamers have advantageous characteristics for cancer therapy, they also have some limitations, namely susceptibility to enzyme degradation by exonucleases or endonucleases [68]. This limitation can be overcome by introducing modifications on nucleotides, namely fluoro nucleotides, or capping the aptamer ends, minimizing the susceptibility to endo and exonucleases and increasing at least 1000-fold longer half-lives of aptamers in blood [68]. Short blood residence time is another drawback of aptamers, due to the fast removal from blood circulation of aptamers with a molecular mass lower than 40 kDa. To increase blood residence time, aptamers can be conjugated with terminal PEG or inverted dT on 3´of aptamer [69]. Chemical modifications currently used to increase its stability and optimize the pharmacokinetic and pharmacodynamic properties are displayed in Figure 5.

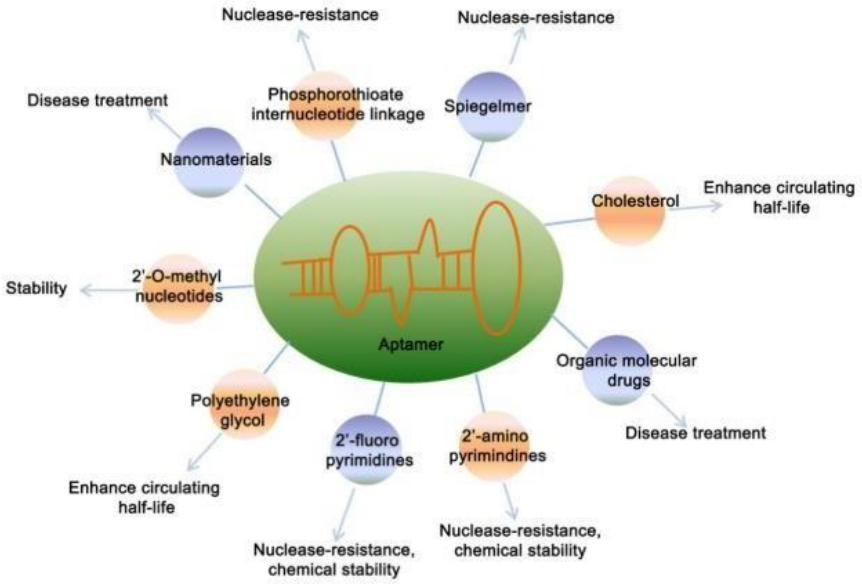

Figure 5 – Chemical modifications of aptamers. Used with permission from "Application and development of aptamer in cancer: from clinical diagnosis to cancer therapy" by Han et al. J. Cancer, vol. 11, no. 23, pp. 6902–6915, 2020, doi: 10.7150/JCA.49532.

Aptamers are produced in vitro by a process known as SELEX, represented in Figure 6, that can be performed with the target in study on live cells or isolated mouse cells [66]. The selection of an aptamer specific to a target of interest can be achieved, starting from a large pool ($< 1 \times 10^{14}$) of single-stranded oligonucleotides with random sequences. Initially, the oligonucleotide pool is incubated with the target, bound aptamers are recovered, and non-binding aptamers are removed. The recovered aptamers are amplified with Polymerase Chain Reaction (PCR) or Reverse Transcription Polymerase Chain Reaction (RT-PCR), depending on if the aptamer is DNA or RNA, respectively. Amplified PCR or RT-PCR pool of binders are used in selection rounds (6-10 rounds generally). At the last round of SELEX, the resulting pool of aptamers are cloned or sequenced, followed by characterization by other methods [70]. Thus, SELEX enables the generation of specific aptamers against a target, that can be expressed on cancer cells [70].

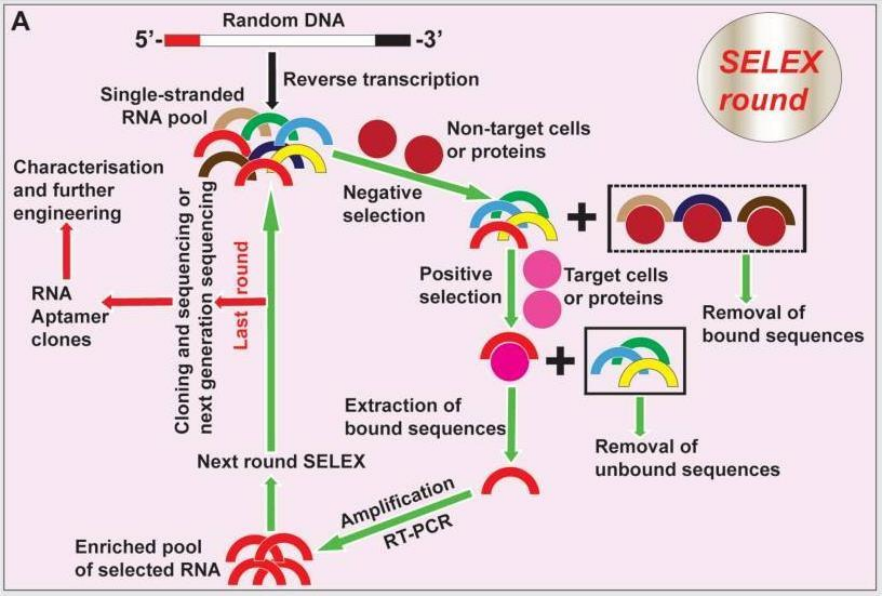

Figure 6 – Schematic illustration of RNA aptamer generation by SELEX. Adapted from [71].

Aptamers can have different applications, specifically in the diagnostic and therapy of cancer. In diagnostic, aptamers can be used for the detection of cellular and proteomic biomarkers of cancer and imaging, being able to recognize oncoproteins, cancer metabolites and even cancer cells, which makes them an important tool for cancer diagnosis, especially when antibodies cannot be applied [68], [71]. In therapy, aptamers can act as therapeutic agents, or in the delivery of drugs [68]. As a cancer therapeutic agent, aptamers can generally have four different functions: inhibition of cancer cell adhesion and invasion, modulation of the immune system, blocking of signaling pathways by inhibiting kinases and binding to target proteins that have a close connection with tumor development [72] [73].

An example of an aptamer is AS1411, developed by Antisoma (NCT00881244) [66]. AS1411 is a DNA guanine-rich aptamer, that forms a G-quadruplex structure (G4), with an anticancer effect against a broad range of cancer cells in vitro [66]. AS1411 possesses high binding specificity to a protein that is overexpressed in numerous types of cancer, nucleolin [66], [74]. Nucleolin is a phosphoprotein with 76-kDa that is very abundant in eukaryotic cells. It contains about 707 amino acids and 3 main structural domains, the N-terminal domain, the central domain and the C-terminal domain [75]. Nucleolin comprises different functions in the cell, namely ribosome biogenesis, DNA replication and recombination, transcription, mRNA stabilization and protein trafficking. Nucleolin function depends on its location in the cell and the structural domain. It is mainly found in the nucleolus, cytoplasm, nucleoplasm, and cell membrane [75]. Nucleolin has been described to play an active role in the development of various types of cancer,

contributing to their proliferation, invasion and angiogenesis, triggering oncogenic signaling pathways and preventing apoptosis [76]. Macugen, is an RNA aptamer, developed by Eyetech Pharmaceuticals/Pfixer (NCT00788177), approved by food and drug administration (FDA), that targets vascular endothelial growth factor (VEGF) [77]. This RNA aptamer has shown in clinical trials to be effective in treating choroidal neovascularization associated with age-related macular degeneration [77]. Another example of an RNA aptamer used in cancer therapy is NOX-A12, developed by Noxxon Pharma (NCT01521533) [78]. NOX-A12 aptamer is a C-X-C chemokine ligand 12 (CXCL12) antagonist that binds to this chemokine and disrupts the accumulation of chronic lymphocytic leukemia (CLL) associated cells in the bone marrow, sensitizing these cells to cytotoxic drugs [78].

As far as oral cancer, to date there are a few aptamers that specifically target this disease. In 2014, Simmon et al. developed anti-heparanase aptamers [79]. Heparanase is an β-1,4-endoglycosidase enzyme that takes part in extracellular matrix degradation and remodeling. It is involved in tumor metastasis and tissue invasion and its expression has been linked to tumorigenesis in different cancers, namely acute myeloid leukaemia, bladder, brain, breast, colon, gastric, esophageal, oral, pancreatic, and cervical cancer. The aptamers developed by this research team, targeting heparanase were capable of inhibiting tissue invasion of tumor cells associated with oral cancer. After that, in 2016, Wang et al. developed a DNA aptamer targeting shared tumor-specific MAGE-A3 peptide antigen [80]. The results showed that the developed aptamer bound to different types of cancer cells, namely oral cancer, indicating that this DNA aptamer can be used in oral cancer cell targeting and in the developing of new forms of diagnosis and therapy. In addition, the 2´fluoro modified RNA aptamer 8A-35, developed by Sung et al. targets human interleukin-8 (IL-8), which is a proinflammatory chemokine that has been associated with the promotion of neutrophil chemotaxis, degranulation and pathogenesis of several neutrophil-infiltrating chronic inflammatory diseases, namely oral cancer. The results showed that 8A-35 aptamer binds to IL-8 with high specificity and affinity, neutralizing IL-8 activity [81]. The aptamers used in oral cancer, their targets and used cell lines are presented in Table 5.

Table 5 – Aptamers used in oral cancer diagnosis and therapy.

Aptamer	Target	Cells Line	References
Anti-heparanase	β-1,4-endoglycosidase enzyme	Human tongue squamous carcinoma cells, HSC-3	[79]
Ap16 and Ap52	MAGE-A3 peptide antigen	Tongue carcinoma cell line, Cal-27	[80]
8A-35	Human interleukin-8	Neutrophils	[81]

1.2.6 Aptamers characterization

For an aptamer to be successfully applied in a drug delivery system, it is necessary to evaluate its characteristics, namely its structure and its interaction with the other molecules integrating the drug delivery system. Currently there are several techniques that are used in the characterization of aptamers, namely the UV-visible (UV-vis) Absorption spectroscopy, circular dichroism (CD), nuclear magnetic resonance (NMR) and surface plasmon resonance (SPR).

1.2.6.1 UV-vis Absorption spectroscopy

Spectroscopy is a technique that measures the interaction of molecules with electromagnetic radiation. Nucleic acids, as other biomolecules, absorb light. Absorption spectroscopy is usually performed with molecules dissolved in a transparent solvent, such as in aqueous buffers. The absorbance of a solute depends linearly on its concentration, accordingly with Lambert- Beer Law, and therefore absorption spectroscopy is ideally suited for quantitative measurements [82].

UV-vis spectroscopy can also be used to distinguish nucleic acids and their secondary structure. Nucleic acids show a broad and strong absorbance peak near 260 nm, but, at 210 nm, RNAs present a negative band, while DNAs have a positive band at this wavelength [82]. Thermal Difference Spectrum (TDS) allows studying temperature effect on secondary structure. TDS is obtained for a nucleic acid by simply recording the ultraviolet absorbance spectra of the unfolded and folded states at temperatures above and below its melting temperature (T_m), which is the temperature at which half the nucleic acids has denatured. The difference between these two spectra is the TDS [83].

UV-vis spectroscopy has been used to characterize several aptamers. For example, and as described earlier in Section 1.2.4, Simmon et al. developed and characterized an anti-heparanase aptamer, which target is important in the development of oral cancer. To achieve that, anti-heparanase short and long aptamers were characterized by UV spectroscopy to study the interaction with human serum albumin (HSA). To accomplish this, increasing concentrations of short and long aptamers were added to HSA. The results showed that the addition of both aptamers to HSA increased the overall absorbance and the HSA characteristic bands shifted, suggesting a conformational change in the protein structure and therefore interaction with the aptamers [79].

By other hand, Santos et al. developed a DNA aptamer named AT11-B1, as a possible targeting aptamer of nucleolin, which is an important protein overexpressed in several types of cancer. In order to evaluate AT11-B1 structure, TDS spectra was recorded. The TDS spectra exhibit two positive peaks at 242 and 273 nm, and two negative peaks at 262 and 295 nm, which indicated the formation of G4 structures [84].

1.2.6.2 Circular Dichroism

CD spectroscopy is method used in biochemistry, structural biology, and pharmaceutical chemistry [85], [86]. CD analyses structure, conformation changes, interaction between proteins, nucleic acids, and ligands, or analyse the thermal denaturation (CD melting) of nucleic acids. CD melting involves temperature control upon spectra acquisition, enabling thermal studies and Tm determination. [85]–[88]. CD spectroscopy has several advantages when compared with higher resolution structural techniques such as crystallography, electron microscopy, and NMR, in that it requires relatively small amounts of sample under conditions (temperature, concentration and components present) that may be more comparable to those found in cells [85].

CD spectroscopy is also a technique widely used in the characterization of aptamer with therapeutic applications, although none of the developed aptamers targeting oral cancer was characterized by this technique.

However, one example of an aptamer characterized by CD spectroscopy is AT11-B1, developed by Santos et al. CD technique was used to understand the structure of AT11-B1 under different concentrations of potassium chloride (KCl). The results showed the formation of different G4 topologies (hybrid and parallel) when KCl concentrations varied [84]. CD-melting experiments were also carried out to elucidate the ability of various ligands to bind and stabilize the AT11-B1 G4 structure [84]. The melting

temperature of AT11-B1 sequence was 49.3 ºC and the ligand 360A was the most stabilizing ligand, with an increase in melting temperature of more than 30ºC [84].

1.2.6.3 Nuclear magnetic resonance

NMR is defined as the interaction of magnetic moments of nuclei of various atoms with magnetic fields [89].

NMR spectroscopy is a powerful tool for studying the structure and dynamics of nucleic acid molecules in solution and their interactions with ligands such as proteins, other nucleic acids, molecules of low molecular weight, ions, and solvent molecules. NMR technique can provide various information about the nucleic acids, namely base-pairing pattern, conformational equilibria, such as those between hairpin and duplex structures, site-specific information about ion binding and resonance assignment of nucleic acids, delineation of secondary structure motifs, such as hairpins and bulges and mapping the interaction surfaces of nucleic acids with ligands [90].

The 8A-45 aptamer developed by Sung et al., is an example of an aptamer developed for oral cancer therapy, characterized by the NMR technique, more specifically to elucidate the interaction of the aptamer with IL-8. To achieve this, $^{1}H - ^{15}N$ 2D heteronuclear single quantum coherence (HSQC) spectra were used for titration experiments of IL-8 with the 8A-35 aptamer. The results suggested that 8A-35 interacts and binds to IL-8 inthe loop or center regions of the IL-8 dimer [81].

1.2.6.4 Surface Plasmon Resonance biosensors

SPR biosensors employ surface plasmons, which are special electromagnetic modes that exist at the surface of metals. In SPR biosensors, the interacting molecules are immobilized on to the surface of the sensor and a solution containing the target molecule is brought into contact with the sensor, resulting in the binding of the molecules. Some applications of SPR biosensors include the investigation of the interaction of nucleic acids with other nucleic acids and with DNA/RNA-binding proteins, enzymes, and small molecules [91].

SPR technique was also performed to elucidate 8A-35 aptamer binding affinity to IL-8. For the assay, an HTG sensor chip containing a Tris - nitrilotriacetic acid complex to capture histidine tagged IL-8. The results showed that the obtained K_D of 8A-35, with a value of 1.72 pM, demonstrated a strong affinity to IL-8 [81].

1.2.7 Drugs: acridine orange derivative and dexamethasone

The last, but not less important unit of a drug delivery system is the anticancer agent, which should be capable of target cancer cells with the minimum activity and losses in blood circulation. After reaching the target site, these molecules should have the capacity to eradicate cancer cells without affecting healthy cells [23]. In this work will be used two different drugs, dexamethasone and an acridine orange derivative.

Dexamethasone, represented in Figure 7, is a synthetic glucocorticoid that is widely used in clinical due to its multiple pharmacological effects [92]. More recently, dexamethasone is increasingly being utilized as an anti-cancer agent [93]. It is also frequently used to prevent side effects of chemotherapy such as nausea, vomiting and pain, as well as to increase the anti-tumor activity of the chemotherapeutic agents as a chemosensitizer and to inhibit tumor growth as an anti-cancer agent [93]. Dexamethasone exerts its anti-inflammatory, anti-angiogenic and control of estrogen activity, by binding to glucocorticoid receptor to regulate gene expression of some important bio-signal molecules, interfering with the transcription of various factors which can regulate proliferation, invasion and metastasis of tumors [92], [93]. Regarding oral cancer, dexamethasone has shown some promising results. Beppu et al. tested the dexamethasone capacity to inhibit matrix metalloproteinase-9 (MMP-9), which is produced by tumor cells and is known to be implicated in the invasion of OSCC [94]. The results showed that dexamethasone could inhibit protein production as well as gene expression of MMP-9 in tumor necrosis factor K (TNFK)-stimulated SCC cells, suggesting that dexamethasone suppress not only immunological reactions, but also tumor invasion [94]. In addition, Shiratsuchi et al. reported the inhibition of extracellular proteases by dexamethasone, including urokinase type plasminogen (uPA) and plasmin, responsible for degradation of extracellular matrix in SCC, showing a potential application in oral cancer treatment [95].

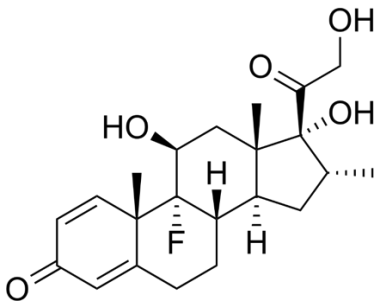

Figure 7 – Dexamethasone chemical structure. Adapted from [96].

10-(8-(4-iodobenzamide) octyl)-3,6-bis (dimethylamine) acridinium iodide (C_8), represented in Figure 8, is an acridine orange derivative, that exerts anticancer effects with high toxicity (IC_{50} values between 0.9 uM and 5.7 uM) in both malignant and normal cell lines [97]. Pereira et al. observed that most acridine orange derivatives presented remarkably high cellular internalization and nuclear uptake, thus suggesting C_8 as a chemotherapeutic candidate for cancer treatment [98].

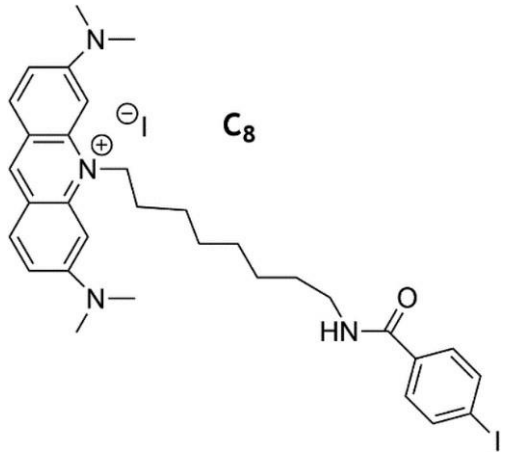

Figure 8 – C_8 chemical structure. Adapted from [53].

Chapter 2

2. Aims of Work

The objectives are delineated in chapter 2 – Aims of Work. The principal aim of this dissertation is to produce, characterize and evaluate the biological potential of nanoparticles, namely liposomes and gold nanoparticles, coated with an RNA aptamer to selectively deliver the ligands C_8, and dexamethasone, to oral cancer cells. In order to reach this study purpose, this dissertation has the following objectives:

1. To evaluate the binding interaction between an RNA sequence and ligands C_8 and dexamethasone by different biophysical techniques; The nucleolin binding to RNA and ligand complexes is also evaluated;
2. To produce and characterize the RNA gold nanoparticles and liposomes and its complexes with C_8 and dexamethasone;
3. To evaluate in vitro the effects on oral cancer cell line versus healthy cells of RNA gold nanoparticles and liposomes loading the ligands C_8 and dexamethasone.

Chapter 3

3. Materials and Methods

The following section, chapter 3- Materials and Methods, will describe the detailed methodology applied in the research work, as well as all the reagents, solution and equipment used.

3.1 Materials

The water used to prepare the solutions was ultrapure grade, purified with a Milli-Q system from Millipore (Burlington, MA, USA). Oligonucleotide sequence (5-(C6SSC6) UfGCfGAAUfCfCfUfCfUfAUfCfCfGUfUfCfUfAAACfGCfUfUfUfAUfGAUfUfCfGCfA(invd T)-3´) designated as RNA, was kindly provided freeze dried by Andrew Ellington, from Department of Chemistry and Biochemistry, University of Texas, Austin, Texas, USA.

Stabilized gold nanoparticles (5 nm diameter) suspension in citrate buffer at concentration of 5.5×10^{13} particles/mL, dexamethasone, fluorescein-5-EX N-hydrooxy-succinimide ester (FITC-NHS) and tris(2-carboxyethyl) phosphine hydrochloride (TCEP) were purchased from Sigma Aldrich (St. Louis, MO, USA). Compound 10-(8-(4-iodobenzamide)octyl))-3, C_8 was synthesized as described before [97]. Hoechst 33342, CyTRAK Orange and (3-(4,5-Dimethylthiazol-2-yl)-2,5-Diphenyltetrazolium bromide (MTT) were purchased from Thermo Scientific (Waltham, MA, USA).). CHOL, 1,2-distearoyl-sn-glycero-3-phosphoethanolamine-N-[amino(polyethyleneglycol)-2000] (DSPE-PEG), 1,2,-distearoyl-sn-glycero-3-phospho-(1´-rac-glycerol) (sodium salt) (PG) and extruder were purchased from Avanti Polar Lipids, Inc (Alabaster, AL). Thiol coupling kit and 2-(2-pyridinyldithio) ethaneamine hydrochloride (PDEA) were purchased from Cytiva (Marlborough, MA, USA).

3.2 Methods

3.3 Preparation of solutions

The freeze-dried oligonucleotide in study was resuspended in diethyl pyrocarbonate (DEPC)-treated water, obtained from Thermo Fisher Scientific (Waltham, MA, USA). The concentration of RNA sample was determined from the absorbance at 260 nm, with an integration time of 0.10 s, a data interval of 1, scan speed of 600 nm/min in a UV-vis

spectrophotometer (Thermo Scientific™ Evolution 220) using the molar extinction coefficient (ε=403600 L/mol.cm^{-1}).

The RNA solutions were stored at - 80ºC.

For confocal microscopy, RNA was labeled with FITC-NHS. Firstly, 2.3 mg of RNA, which has a disulfide bond at the 5´end, was reduced (RNA-SH) by adding 242 µL of TCEP, according to Eq. (I).

$$\mu l \text{ of TCEP} = \frac{\text{mg RNA}}{1\frac{\text{mg}}{\text{mL}} \text{of TCEP}} \times \frac{\text{MW TCEP}}{\text{MW RNA}} \times x \times 1000 \qquad \text{Eq. (I)}$$

where MW TCEP=286.7 g/mol, MW RNA= 13606 g/mol and x is the desired stoichiometry reaction (5 TCEP:1 RNA). Then, five washes were done in centricons with a MWCO=2000 Da at 200 RCF for 40 min, with a prewash of the centricons with H_2O Milli-Q at 1000 RCF for 30 min, to remove TCEP in excess.

Afterwards, to activate FITC-NHS and make it reactable with RNA-SH, a solution of FITC-NHS, dissolved in dimethyl sulfoxide (DMSO), was incubated with a PDEA solution, dissolved in a 0.1 M sodium tetraborate pH=8.5, in a 1:2 stoichiometry, respectively.

Then, 100 µg of RNA-SH was incubated overnight with agitation, with 1.5 equivalents of activated FITC-NHS in a 0.1 M sodium tetraborate pH=8.5 solution. After overnight incubation, FITC-NHS labeled RNA-SH (RNA-FITC) was recovered by precipitation at 16000 g and 4 ºC, using 1 volume of 3 M NaCl and 2.5 volumes of 100% frozen ethanol and followed by 3 washes with 75% ethanol at 14080 g.

The ligands used were C_8 and dexamethasone. The solutions were prepared in DMSO, with the following concentrations: C_8 (10 mM; 1 mM) and dexamethasone (10 mM; 1 mM).

3.4 Biophysical Evaluation of RNA with ligands

3.4.1 Circular Dichroism (CD) spectroscopy

CD spectroscopy was used to characterize the secondary structure of RNA. CD melting was used to study the stabilization or destabilization of the oligonucleotide structure in the presence of C_8 and dexamethasone.

CD experiments were performed on a Jasco J-815 CD spectropolarimeter, equipped with temperature controller Peltier (model CDF-426S/15). Readings were performed in a 1 mm path-length quartz cuvettes at 20 ºC. Spectral width was set to 200–340 nm, with a scan speed of 100 nm/min, 1 nm bandwidth, and 1 s integration time over 4 averaged accumulations.

Firstly, 10 µM of RNA samples were prepared under different conditions in order to study its secondary structure. The studied conditions were: (1) with annealing (incubation for 10 min at 95 ºC and cool down at 10 ºC for 10 min) and 65 mM KCl + 20 mM KPi; (2) without annealing and 65 mM KCl + 20 mM KPi; (3) with H_2O DEPC-treated water.

CD-melting assays were also performed to study the interaction of RNA with different equivalents of C_8 and dexamethasone (0; 0.25; 0.50; 0.75; 1; 1.50 and 2). Ellipticity was analyzed across different temperatures, ranging from 20-100 ºC, with a heating rate of 0.5 °C/min, while monitoring the ellipticity at 260 nm. Readings were done considering all parameters above defined for Jasco J-815 CD spectropolarimeter.

Data were converted into fraction folded (f) plots according to Eq. (II) and fitted to a Boltzmann distribution using Origin2018:

$$f = \frac{CD_{\lambda} - CD_{\lambda}^{min}}{CD_{\lambda}^{max} - CD_{\lambda}^{min}} \qquad \text{Eq. (II)}$$

where CD is the ellipticity of the monitored wavelength at each temperature and CD_{min} and CD_{max} are the lowest and highest ellipticity, respectively. The T_m of RNA were determined using a Boltzmann distribution (Origin 2018).

3.4.2 Thermal Difference Spectroscopy (TDS)

TDS experiments were performed on a UV-vis spectrophotometer (Thermo Scientific™ Evolution 220), from 220 to 335 nm, with an integration time of 0.10 s, a data interval of 1 nm, and a scan speed of 200 nm/min. Firstly, a 2 mL with 6 µM sample of RNA was prepared and the spectrum at 20 ºC was measured. After that, the solution was heated up to 90 ºC and another spectrum was taken. This procedure was performed in triplicate. TDS spectra were obtained by analyzing the difference in absorbance from spectra obtained at 90 ºC and 20 ºC, using GraphPad Prism 8 software.

3.4.3 Nuclear Magnetic Resonance (NMR)

Standard ^{1}H NMR spectra were acquired on a 600 MHz Bruker Avance III spectrometer with a QCI cryoprobe at 25 °C. Water signals were suppressed with an NMR zgesgp pulse sequence.

To evaluate RNA structure, a 200 µL sample was prepared in DEPC-treated water, containing 80 µM of RNA and 10% of deuterium oxide (D_2O). NMR titration with nucleolin was performed by adding increasing amounts, 0, 1, and 2 equivalents of nucleolin to 200 nM RNA sample. Saturation transfer difference (STD) spectra were also recorded to study the interaction of nucleolin with RNA. All solutions were prepared in 3 mm NMR tubes. Chemical shifts (δ) were measured in part per million (ppm) and spectra were acquired and processed with the Topspin 4.0 software.

3.4.4 Surface Plasmon Resonance (SPR)

SPR technique was performed to determine the affinity between RNA and C_8, dexamethasone, and nucleolin, using a Biacore T200 (Cytiva, USA).

Firstly, a desorb and sanitize protocol was performed to clean the flow systems, followed by an instrument stabilization period of about 4 h. Then, a normalization procedure was performed with the CM5 chip. Several primes were carried out with HBS-N (0.1 M HEPES, 1.50 M NaCL) running buffer before experiments. Then, the surface of the CM5 surface was activated with a 2 min pulse of a mixture of EDC/NHS (1:1) followed by a 4 min pulse of 80 mM PDEA, 0.10 M sodium borate (pH 8.5). After activation of the surface, 25 µg of thiolated RNA were immobilized onto flow cells of a research-grade CM5 chip using a standard thiol coupling chemistry with a flow rate of 5 µL/min and HBS-N as running buffer. Finally, a pulse of 50 mM cysteine, 1 M NaCl, 0.10 M sodium acetate, and pH 4.00 (4 min) was used to deactivate excess of reactive groups and remove non-specifically bound molecules from the surface. The amount of immobilized thiolated RNA was 220.60 RU.

After that, solutions of C_8, dexamethasone and nucleolin were injected under RNA surface and the binding constants determined using the 1: 1 binding mode.

3.4.5 Fluorescense Spectroscopy

Fluorescence titrations were performed to determine the affinity of RNA for C_8, dexamethasone and NCL.

Fluorescence titrations were conducted on a FluoroMax 4 fluorometer (HORIBA, Japan) equipped with a Peltier-type temperature control system, defined to 20 ºC.

For fluorescence titration experiments, two fluorescent molecules were used, FITC and C_8. The FITC was coupled to reduced RNA as described in section 2.1.

The ligand C_8 is fluorescent (excitation = 492 nm, and emission range scan = 505-700 nm), and it was associated with RNA via supramolecular. Briefly, 1 µM of the RNA was added to 5 µM of C_8 and allowed to react 15 minutes before the start of the experiments.

After that, both solutions (RNA-FITC and RNA-C_8) were prepared at 1 µM 100 mM KCl + 20 mM KPi. The solutions were then loaded to a high-precision quartz suprasil cuvette (light path 10 mm × 4 mm) with a final volume of 700 µL.

The spectra measurement settings were applied in accordance with fluorophore FITC-NHS (excitation = 498 nm, and emission range scan= 505-700 nm) or C_8, at 25 ºC, with an integration time of 0.5 s, an emission and excitation slit fixed at 3 nm (when following FITC-NHS fluorescence) or 1 nm (when following C_8 fluorescence) and step size of 1 nm, averaged over 3 scans.

Firstly, the RNA affinity for C_8 was assessed. To achieve this, C_8 was titrated with increasing concentrations of RNA. Then, to evaluate the affinity of RNA for dexamethasone and NCL, RNA-FITC was titrated with increasing concentrations of dexamethasone and NCL respectively. Finally, to evaluate if RNA in presence of 5 equivalents of C_8 or dexamethasone increased the affinity to NCL, C_8 or RNA-FITC were titrated with increasing concentrations of NCL. Moreover, C_8 was titrated with increasing concentrations of NCL. Changes in fluorescence were measured. After each addition, the mixture was left for 10 min for equilibration and then acquired. The obtained data was converted into a fraction of bound ligand (α) plots using the following equation (Eq. III):

$$\alpha = \frac{I_{\lambda} - I_{\lambda}^{free}}{I_{\lambda}^{bound} - I_{\lambda}^{free}} \qquad \text{Eq. (III)}$$

where I is the fluorescence intensity at 520 nm when using RNA-FITC fluorophore, and 524 nm, when using C_8 fluorophore, at each ratio, and I_{free} and I_{bound} are the fluorescence intensity of the free and fully bound NCL, C_8, or dexamethasone, respectively. Data points were then fitted according to the most suitable model (two site bind, Michaelis Menten or Hill model), using Origin Pro 2016.

K_D (apparent equilibrium dissociation constant) was calculated according to the equations presented in Table 6.

Table 6 – Equations to proceed to fit data points in fluorometric assays.

Methods	Equations
Two site bind	$\alpha = \frac{B_{Max1}[\mathrm{FLUO}]^h}{K_{D1} + [\mathrm{FLUO}]^h} + \frac{B_{Max2}[\mathrm{FLUO}]^h}{K_{D2} + [\mathrm{FLUO}]^h}$
Michaelis-Menten	$\alpha = \frac{[\mathrm{FLUO}]}{K_D + [\mathrm{FLUO}]}$
Hill	$\alpha = \frac{[\mathrm{FLUO}]^h}{K_D + [\mathrm{FLUO}]^h}$

Where [FLUO] is the concentration of the FITC-NHS labeled RNA or C_8 and h is the Hill constant.

3.4.6 Agarose gel electrophoresis

Agarose gel electrophoresis technique allowed the study of the efficacy of labeling RNA-SH with FITC-NHS, based on their respective length.

Initially, the gel electrophoresis apparatus was set up and a 1% agarose gel was prepared, by mixing a solution of 50 mL of 1× tris-acetate-EDTA (TAE 1×) buffer with 1% agarose and heating up in a microwave until agarose was totally dissolved. Then, the solution was cooled under running water and 1% of Xpert Green DNA Stain 20000× (GRiSP, Portugal) was added to the mixture and placed in the gel crib until complete polymerization. Afterwards, 1 µg of FITC-NHS, RNA-SH, 4 µL of molecular weight GRS ladder 1 kb, and GRS ladder 25 kb were loaded into the wells. The gel ran at 120 V for 30 min. After that, the gel was visualized using UV light exposure in UVITEC Cambridge UV chamber (UVITEC Cambridge, United Kingdom).

3.5 Synthesis and characterization of drug delivery systems

3.5.1 RNA/ligands-coated gold nanoparticles synthesis

Functionalization of gold nanoparticles with thiolated RNA containing C_8 or dexamethasone was achieved using a method adapted from the one previously described by Malik et al. [99].

Thiolated RNA was first reduced by incubating overnight, at room temperature, with a filtrated solution of 10 mM TCEP, in a 100× molar excess. After that, RNA-SH was added to 5 nm colloidal gold nanospheres to give a final oligonucleotide: gold nanoparticle ratio of 200:1. The mixture was incubated overnight with stirring.
After overnight incubation on a rotator, a filtered solution of 20 mM potassium phosphate (KPi) was added until reaching a final concentration of 10 mM. Four hours later, filtrated 3 M sodium chloride (NaCl) was added to the solution until reaching a final concentration of 100 mM. The solution was left in rotation for 4 h. To finish, more filtrated NaCl solution was added until reaching a final concentration of 300 mM and it was incubated overnight in rotation, at room temperature.

To remove excess salts in the solution, the sample was inserted in a D-Tube Dialyzer Maxi (Millipore, Burlington, Massachusetts; MWCO 3.50 KDa). Dialysis was performedfor 2 days, and the H_2O Milli Q was replaced two times a day.

Finally, and after determining the concentration of functionalized RNA gold nanoparticles by reading the absorbance at 260 nm in UV-vis spectrophotometer, supramolecular assembly of C_8 or dexamethasone was obtained by incubation with these ligands, with ratios of 15:1 of RNA:C_8 and 15:5 RNA: dexamethasone.

3.5.2 Liposomes Drug Delivery System Synsthesis

Liposomes based nanoparticles of RNA with C_8 or dexamethasone were synthesized from CHOL, PG, and DSPE-PEG at a molar ratio of 2:1:0.16.

Firstly, solutions of CHOL, PG, and DSPE-PEG were prepared in chloroform with concentrations of 100 mg/mL, 25 mg/mL, and 25 mg/mL, respectively. Then, the lipids were mixed in a 2 mL eppendorf, previously weighed, according to the defined molar ratio inside a laminar flow chamber, allowing the chloroform to evaporate overnight. Afterward, and after measuring the weight of lipids present in the eppendorf, the lipids

were resuspended in a PBS solution containing C_8 or dexamethasone, in 1 lipids : 0.025 C_8 or 1 lipids: 0.10 dexamethasone ratios, at 65°C for 10 min. Subsequently, five cycles of freeze (liquid nitrogen) and thaw (40°C) were performed to form the liposomes encapsulating C_8 or dexamethasone. After liposome formation, the solution was passed 11 times in an Avanti Mini Extruder (Avanti Polar Lipids), in order to standardize the size of the liposomes. After extrusion, 5 washes were carried out in a centricon centrifugal filter with an MWCO=2000 kDa at 200 RCF for forty minutes, with a prewash with H_2O Milli-Q at 1000 RCF for 30 min.

To associate C_8 or dexamethasone with liposomes-based RNA, the RNA was firstly reduced as described in Section 2.1. Then, to activate liposomes and allow the functionalization with RNA-SH, liposomes were incubated for 2 h with PDEA in a 1:5 stoichiometry dissolved in PBS at pH=8.50. After this, RNA-SH was incubated overnight in a rotator with the activated liposomes. Finally, the liposomes-based nanoparticles of RNA with C_8 or dexamethasone were washed 5 times as described before in this section.

Encapsulation studies of C_8 and dexamethasone on liposomes were carried out via UV-vis spectroscopy.

To calculate the encapsulated concentration of C_8 or dexamethasone, a standard curve was constructed by measuring the absorbance of different standardized concentrations of C_8 (10 µM, 15 µM, 20 µM, 25 µM, and 30 µM) at 496 nm and dexamethasone (25 µM, 50 µM, 75 µM, and 100 µM) at 245 nm. Then, obtained optical density (OD) data versus concentration of C_8 or dexamethasone standard solutions curve was plotted in Excel software and a standard curve for each therapeutic agent was obtained. The concentration of encapsulated C_8 or dexamethasone were extrapolated from the equation ($y=142.93x-6.30$ for C_8 and $y=58.786x+16.71$ for dexamethasone) of the standard curve.

3.5.3 Stewart Assay

The amount of lipids (CHOL, DSPE-PEG and PG) in a liposome formulation were determined by the Stewart Assay.

Firstly, an ammonium ferrothiocyanate (AF) solution was prepared by dissolving 27.03 g of ferric chloride hexahydrate and 30.40 g of ammonium thiocyanate in 1 L of deionized distilled water. Then calibration samples were prepared by pipetting off 0.1 up to 1 ml of a 10 mg/100 mL DSPE-PEG solution, adding 2.00 ml of AF and then adding chloroform for a final volume of 4.00 mL. Calibration samples were vortexed for 1 minute and

allowed to sit for at least 15-20 min. Liposome sample preparation was achieved by diluting to about 100x a 20 μL liposome sample in phosphate buffer. Then, to 0.2 mL of the prepared solution was added 2 mL of chloroform and 2 mL of AF. Afterwards, lower chloroform phase was removed from calibration and liposome prepared solutions and added to a cuvette. Finally, a standard curve (OD vs mg of lipid) of the calibration samples was constructed, by measuring the optical density of the calibration samples at 470 nm (maximum absorbance of DSPE-PEG). Liposome prepared solution was measured at the same wavelength and mg of DPSE-PEG was extrapolated from the equation of the standard curve. Blank was set with pure chloroform. Quantity of other lipids present in liposome solution was calculated based on the ratio used in Section 3.5.2.

3.5.4 Nanoparticle tracking analysis (NTA)

NTA technique was used to characterize the size and concentration of a liposome liquid sample suspension. This technique combines laser light scattering microscopy with a charge-coupled device camera, which enables the visualization and recording of nanoparticles in solution. NTA software is able to identify and track individual nanoparticles moving under Brownian motion and relates the movement to a particle size according to the following formula derived from the Stokes-Einstein equation (IV):

$$(x, y)^2 = \frac{2k_B T}{3r_h \pi y} \qquad \text{Eq. (IV)}$$

where k_B is the Boltzmann constant and $(x, y)^2$ is the mean squared speed of a particle at a temperature T, in a medium of viscosity η, with a hydrodynamic radius of r_h [100].

NTA measurements were performed with a NanoSight LM20 (NanoSight, Amesbury, United Kingdom), equipped with a sample chamber with a blue 488 nm laser. All measurements were performed at 22.50 ºC. The software used for capturing and analyzing the data was the NTA 3.2 Build 3.2.16. Five measurements of each sample were performed for all liposome solutions.

3.5.5 Dynamic Light Scattering (DLS)

The nanoparticles previously synthesized were characterized by size distribution and PDI using a Zetasizer Nano ZS equipment (Malvern Instruments, Worcestershire, UK). Briefly, the average size and PDI were evaluated by placing 1 mL of liposomes or gold nanoparticles solution into a quartz glass cuvette. Data was collected at constant temperature of 25 ± 1 ºC. Each value was obtained by averaging measurements of three samples.

3.5.6 Electron microscopy

SEM and TEM techniques were used to characterize the morphology and size of synthesized liposomes and gold nanoparticles.

For SEM sample preparation, 10 µL of liposomes sample were pipetted to a glass coverslip and left to air for drying overnight at room temperature. Afterwards, the coverslip containing the liposomes sample was mounted on an aluminum board using a double-sided adhesive tape and covered with gold using a Emitech K550 sputter coater (London, England). Finally, the samples were placed properly in the interior of a VP SEM Hitachi S- 3400N scanning electron microscope (Tokyo, Japan), and liposome images were taken at an acceleration voltage of 20 kV.

For TEM the gold nanoparticle samples were placed on a formvar-coated copper grid and allowed to dry at room temperature. The images were acquired using a Hitachi-HT7700 (Tokyo, Japan) transmission electron microscope.

3.5.7 Native polyacrylamide gel electrophoresis (PAGE)

Native PAGE was used to study the interaction of RNA with NCL through molecular mass separation and to evaluate the efficacy of liposome functionalization with RNA using the following protocol.

A 15% polyacrylamide gel was prepared and placed in the electrophoresis chamber with a gel holder and a comb to polymerize and form the wells. Then the chamber was filled with running buffer (Tris-borate-EDTA 1×). Before sample loading, the gel ran for 20 min at 120 V to clean the wells. To study RNA interaction with NCL, 11 samples were prepared, each with 200 nM of RNA and with increasing concentrations of NCL, specifically 0, 25 nM, 50 nM, 100 nM, 200 nM, 400 nM, 800 nM, 1600 nM, 3200 nM, and 6400 nM, in appropriate protein buffer (100 mM KCl+20 mM KPi). To all solutions

was added 20% of sucrose. After sample preparation, 15 µL of each sample was loaded to the gel, followed by electrophoresis running at 150V for 40 min. After that, the gel was separated from the holder and emerged in staining solution (Sybr Gold) for 40 min. After staining, the gel was revealed in ChemiDoc XRS+.

3.6 In Vitro Studies

For cellular studies, two cell lines were used. Normal Human dermal fibroblasts (NHDF; ref. PCS-201-012™, ATCC) cells were grown in RPMI medium, supplemented with 10% fetal bovine serum (FBS), 1% streptomycin– penicillin antibiotic, 0.01 M HEPES, 0.02 M L-glutamine and 0.001 M sodium pyruvate. Squamous cell carcinoma of the tongue (SCC154; ref. CRL-3241™, ATCC) cells were grown in EMEM medium, supplemented with an additional 2 mM L-glutamine and heat-inactivated fetal bovine serum to a final concentration of 10%.

3.6.1 Cell viability assay

Upon confluence, cells were seeded into 96-well culture plates (5×10^4 cells/mL) in 100 µL of medium. Cells were treated with 100 µL of medium with different stimuli. Firstly, IC_{50} of C_8 or dexamethasone in both cell lines were determined. Then, cells were treated with different conditions: C_8-RNA (5 µM), dexamethasone-RNA (5 µM), RNA gold nanoparticles with C_8, RNA gold nanoparticles with dexamethasone, RNA liposomes with C_8 and RNA liposomes with dexamethasone.

After 72 h of incubation under controlled humidified atmosphere at 37 ◦C and 5% CO2, 100 µL of 1 mg/mL, MTT solution, dissolved in 20% of PBS and 80% of incomplete medium, was added into each well and were further incubated for 4 h. The resulting formazan crystals were dissolved in 100 µL of DMSO and the OD was recorded at 570 nm. Cell viability was determined using wells without compounds as the control.

3.6.2 Confocal Microscopy

For fluorescence confocal microscopy assays, NHDF and SCC-154 cells were seeded at 50×10^3 per well in a treated µ-slide eight well (IBIDI, Gräfelfing, Germany) in 200 µL of medium and grown at 37 ºC under a 95% air and 5% CO_2 humidified atmosphere.

Initially, to verify if RNA internalizes the cells and how long it takes, SCC-154 cells were firstly incubated with a 2 µM nuclear probe Hoechst 33342 for 15 min. After incubation,

cells were washed with PBS 3 × and treated with 10 μM of RNA-FITC. Cells were imaged using a Zeiss AxioObserver LSM 710 microscope (Oberkochen, Germany) with a 405 and 488 nm laser excitation for Hoechst 33342 and RNA-FITC, respectively.

Then, in order to understand if RNA could internalize via NCL, SCC-154 cells were firstly incubated with the NCL antibody (1:100) for 2 h and a secondary antibody (Alexa Fluor 647®, 1:1000) for 1 h. Then, cells were treated with RNA-FITC for 2 h. Finally, cell nuclei were stained with 2 μM nuclear probe Hoechst 33342 for 15 min. Between incubations, cells were washed with PBS 3 ×. Cells were imaged using a Zeiss AxioObserver LSM 710 microscope (Oberkochen, Germany) with a 405, 488, and 555 nm laser excitation for Hoechst 33342, RNA-FITC, and NCL, respectively.

Finally, SCC-154 cells were incubated with 2 μM nuclear probe Hoechst 33342 for 15 min. Then, the wells were washed 3 × with PBS and treated with 10 μM of RNA-FITC for 2 h. Finally, cells were washed again 3 × with PBS and incubated with 10 μM CyTRAK Orange for 30 min. Cells were imaged using a Zeiss AxioObserver LSM 710 microscope with a 405, 488, and 555 nm laser excitation for Hoechst 33342, RNA-FITC, and CyTRAK orange, respectively.

3.6.3 Statistical analysis

Data are presented as the mean ± standard deviation (s.d.). Multiple t tests- one per row with Holm-Sidak method was used for multiple groups comparison. A p-value lower than 0.05 ($p<0.05$) was considered to be statistically significant. Statistical analysis was performed using GraphPad Prism v.8.0.1 software (GraphPadSoftware, USA).

Chapter 4

4. Results and Discussion

In chapter 4 – Results and Discussion, the obtained data are presented and discussed. This section is divided into three parts, starting with the biophysical evaluation of the used RNA and interaction studies with nucleolin, dexamethasone and C_8. The second part of the chapter focuses on the characterization of produced nanosystems, namely RNA functionalized gold nanoparticles and liposomes carrying dexamethasone or C_8 supramolecular assembled or encapsulated. The final part accounts for the in vitro evaluation of the nanosystems, namely the viability assays, in non-malignant (NHDF) and malignant oral cancer cells (SCC-154), and confocal microscopy to evaluate RNA internalization, whether or not via nucleolin and localization.

All obtained data is arranged, displayed, and further analyzed to find and explain the reasons behind each outcome, based on literature review. Thus, the connection between results and exploited paths allows us to logically understand the work sequence.

4.1 Biophysical Evaluation of Oligonucleotide and Interaction Studies

4.1.1 Evaluation of RNA structure

The RNA used in this dissertation is a nucleic acid constituted by 41 bases developed by SELEX technique in University of Texas, USA. The RNA used in this dissertation results from a previous work developed by Magalhães et al. that used a SELEX method aiming the selection of a pool of oligonucleotides that were capable of internalizing different cells and tissues [101].

The sequence of the RNA used in this dissertation is (5-(C6SSC6) UfGCfGAAUfCfCfUfCfUfAUfCfCfGUfUfCfUfAAACfGCfUfUfUfAUfGAUfUfCfGCfA(invd T) 3´), which has several modifications, giving special characteristics to this RNA. The 3´inverted dT residue enhances the serum stability, 5´thiol modification makes possible the connection to the gold nanoparticles, liposomes and labeling with FITC-NHS and the 2´-fluoro modifications confer resistance to cellular nucleases [101]. It was found that the RNA was capable of internalizing several types of cells, namely Min6B1, BTC3, Bend.3, Sol8, C2C12, A549, HEK293, HeLa, PC3 and LnCAP cells [101]. Additional

studies regarding the mechanism of uptake into cells suggested that the RNA internalized by a clathrin-mediated endocytosis [101].

Although the pathway of internalization needs to be further explored, this RNA presents unique characteristics, namely the capacity of internalization into a variety of cells, that may be advantageous for being applied in drug delivery systems for cancer therapy.

4.1.1.1 Circular Dichroism (CD) studies

Firstly, the structural arrangement of RNA under different conditions was studied by CD spectroscopy. To achieve this, 10 μM of RNA was prepared under different conditions: (1) with annealing (incubation for 10 min at 95°C and cool down at 10°C for 10 min) and 65 mM KCl + 20 mM KPi; (2) without annealing and 65 mM KCl + 20 mM KPi; (3) with H_2O DEPC-treated water. The obtained CD spectra for the studied conditions are presented in Figure 9.

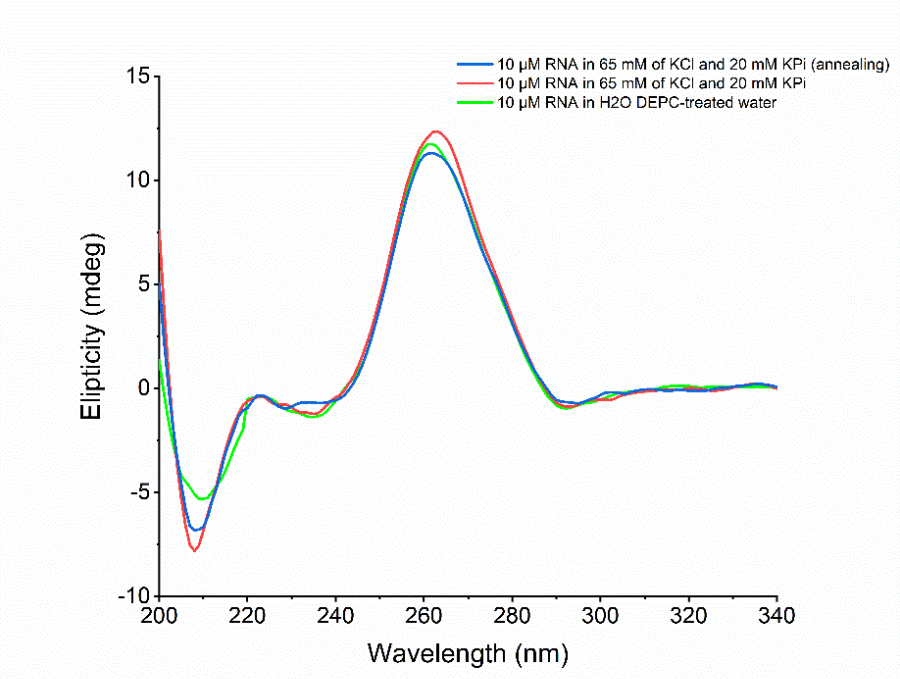

Figure 9 – CD spectra of RNA under different conditions: blue line (1) with annealing (incubation for 10 min at 95°C and cool down at 10°C for 10 min) and 65 mM KCl + 20 mM KPi; red line (2) without annealing and 65 mM KCl + 20 mM KPi; green line (3) with H_2O DEPC-treated water.

By analyzing Figure 9, it is visible that the spectra of all the studied conditions show a RNA signature CD profile, represented by positive wavelength band around 260 nm and a negative band around 210 nm. The RNA, in 65 mM of KCl and 20 mM KPi with annealing, does not present the signatures of a G4 structure. The CD bands characteristic

of G4 topologies are: parallel (maximum at around 264 nm and minimum at around 254 nm), antiparallel (maximum at around 295 nm and minimum at around 260 nm) or hybrid (maximum at around 295 and 260 nm and minimum at around 245 nm) [102].

In the different experimental conditions, the characteristic RNA bands are retained and the ellipticity does not change, suggesting that the RNA structure does not form a G4 structure.

Then, the thermal denaturation temperature of the RNA was determined by monitoring the wavelength of maximum ellipticity (260 nm) at increasing temperatures. Figure 10 and Table 7 represents the obtained CD melting curves and respective thermal denaturation temperature of 10 μM of the RNA.

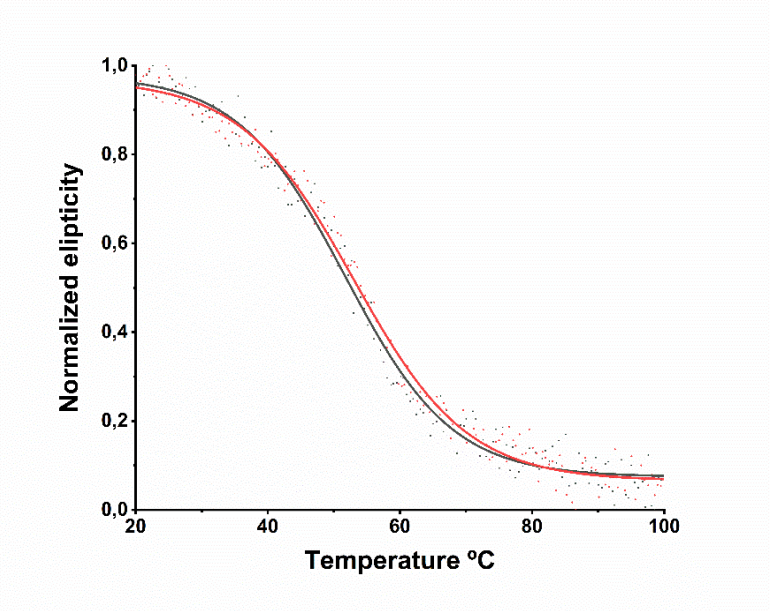

Figure 10 – CD melting spectra of the RNA. The experiment was performed in duplicate.

Table 7 – Melting temperatures of RNA obtained by CD melting experiments.

	T_m (°C)		T_m (°C)
First Experiment	51.69 ± 0.33	**Second experiment**	53.05 ± 0.31

After obtaining the melting temperatures presented in Table 7, the mean with standard deviation was calculated and the obtained value corresponded to the thermal denaturation temperatures of the RNA, which was 52.37 ± 0.96 °C.

4.1.1.2 TDS

TDS allow the study of the effect of temperature on secondary structure of RNA, namely the presence of folding or unfolding state.

Figure 10 shows the UV absorbance spectra at temperatures above (90 °C) and below (20 °C) the previously determined thermal denaturation temperature of the RNA (52.37 ± 0.96 °C) by CD technique. Figure 11 represents the TDS spectra obtained by subtracting the spectrum from 20°C (coiled state) to 90°C (denatured state).

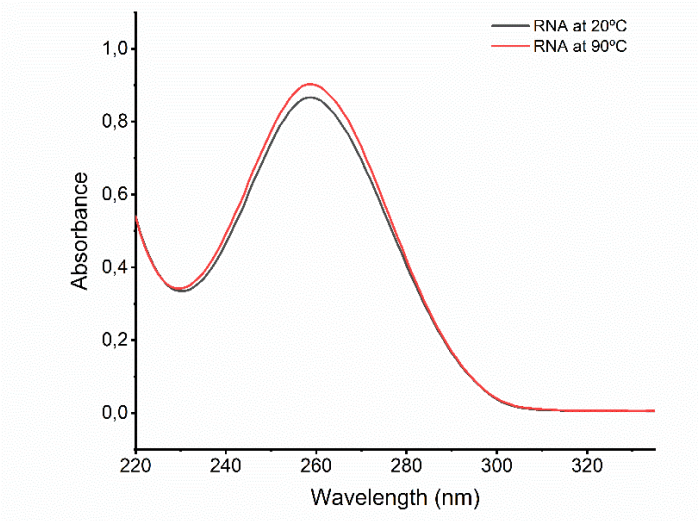

Figure 11 – RNA UV absorbance spectra at 90 °C and 20 °C.

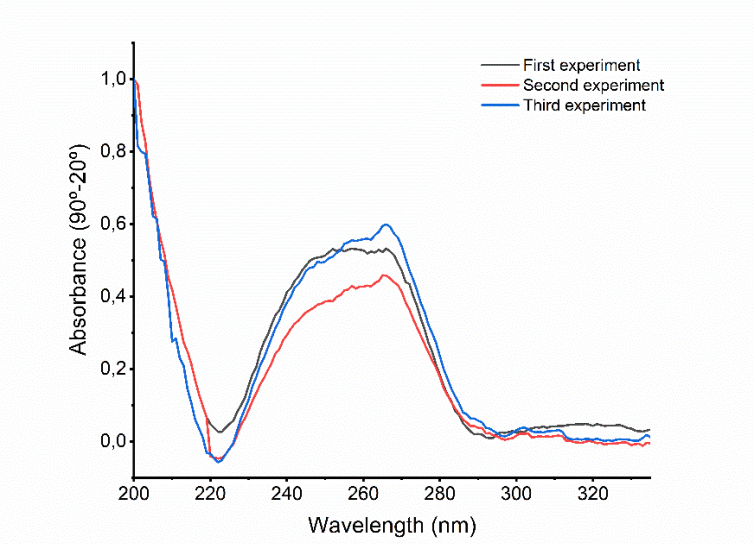

Figure 12 – TDS spectra of RNA.

Although there are several studies that use TDS to evaluate the secondary structure of nucleic acids, most of them focus on nucleic acids that form G4 structures [83].

Through the analysis of the TDS spectra, we can observe that the obtained spectra are characteristic of a duplex since it presents a maximum peak at about 266 nm. The obtained results also corroborate the ones obtained with the circular dichroism technique, demonstrating that this RNA does not fold in a G4 structure. Otherwise, G4 TDS characteristic positive peaks at about 243 nm and 273 nm and a negative peak at about 295 nm should be visible [83].

4.1.1.3 NMR Spectroscopy

NMR spectroscopy assays were conducted for RNA to analyze its structure, at a temperature of 25 º C. Figure 13 depicts the obtained RNA spectrum.

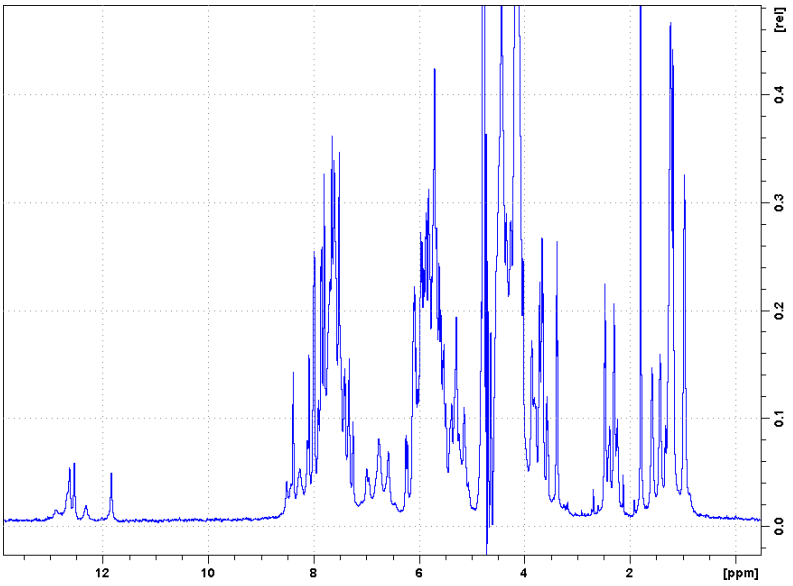

Figure 13 – RNA NMR spectrum.

The ^{1}H spectrum shows one well defined set of signals, in the imino region, corresponding to the RNA duplex and hairpin profile (12.5 - 14 ppm) [103]. This result is in agreement with what was described by Magalhães et. al, since the describedstructure of the RNA presents a duplex and hairpin regions [101]. Additionally, no G4 structure characteristic signals (10 - 12 ppm) are observed, which also proves the resultsobtained by CD and TDS techniques, that demonstrated that RNA did not form a G4 structure. Moreover, at around the range of 6.0 – 8.0 ppm, there are present signals corresponding to the aromatic portions of the RNA. It is important to note that the

above-mentioned regions will be important in subsequent assays to evaluate the interaction of the RNA with the different studied molecules.

4.1.2 Evaluation of RNA interaction with C_8, dexamethasone and nucleolin

4.1.2.1 CD Melting studies

CD spectroscopy, namely CD melting, was also used to evaluate RNA interaction with C_8, dexamethasone and nucleolin.

The T_m of RNA in absence and presence of increasing amounts of C_8 and dexamethasone was determined by monitoring the wavelength of maximum ellipticity (260 nm) at increasing temperatures. Figure 14 represents the obtained CD melting curves with increasing amounts of C_8 and dexamethasone.

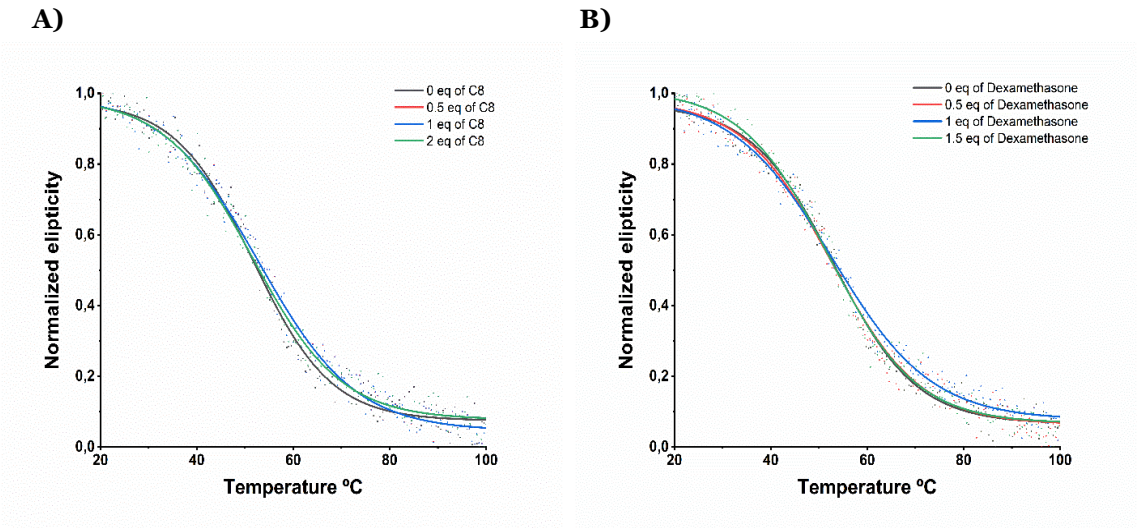

Figure 14 – CD melting spectra of the RNA. A) CD melting curves in the presence of increasing amounts of C8. B) CD melting curves in the presence of increasing amounts of dexamethasone.

By analyzing the CD melting data presented in Figure 14, C_8 and dexamethasone seems to not stabilize or destabilize the RNA structure, as suggested by the obtained T_m values presented in Table 8.

Table 8 – Melting temperatures of RNA obtained upon titration with increasing amounts of C_8 and dexamethasone.

Equivalents of C_8	T_m (ºC)	Equivalents of dexamethasone	T_m (ºC)
0	51.69 ± 0.33	0	53.05 ± 0.31
0.5	52.91 ± 0.38	0.5	52.59 ± 0.36
1	52.91 ± 0.38	1	52.72 ± 0.38
2	51.63 ± 0.37	2	52.07 ± 0.33

Taking these data into account, we can conclude that C_8 and dexamethasone do not stabilize RNA structure, so they will be used in developed nanosystems as therapeutic agents, due to their anticancer potential.

4.1.3 RNA with NCL interaction studies

The Native PAGE experiment, presented in Figure 15, was used to study the interaction of RNA with NCL through molecular mass separation.

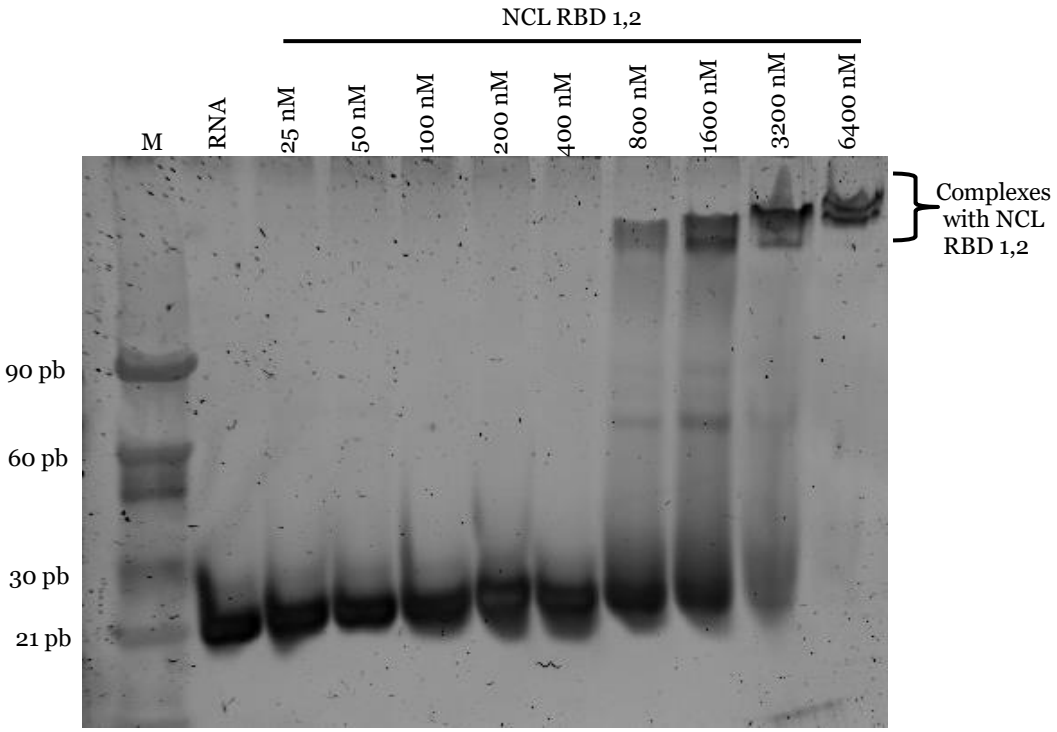

Figure 15 – Native PAGE of 200 nM of RNA in 100 mM KCl+20 mM KPi with increasing concentrations of NCL in each lane.

The native PAGE experiment, presented in Figure 15, shows the molecularity of RNA and RNA-NCL RBD1,2 complexes. The upper band found in the gel corresponding to higher molecular weight represents the complex RNA-NCL RBD1,2 and its dependent on NCL concentration, since at 800 nM of NCL the complex starts to form and the formation of the RNA-NCL complex is maximum at a protein concentration of 6400 nM.

NMR titrations of RNA with NCL were also performed in order to elucidate the interaction of these two molecules. The ^{1}H NMR spectra of the RNA upon NCL titrations are displayed in Figure 16.

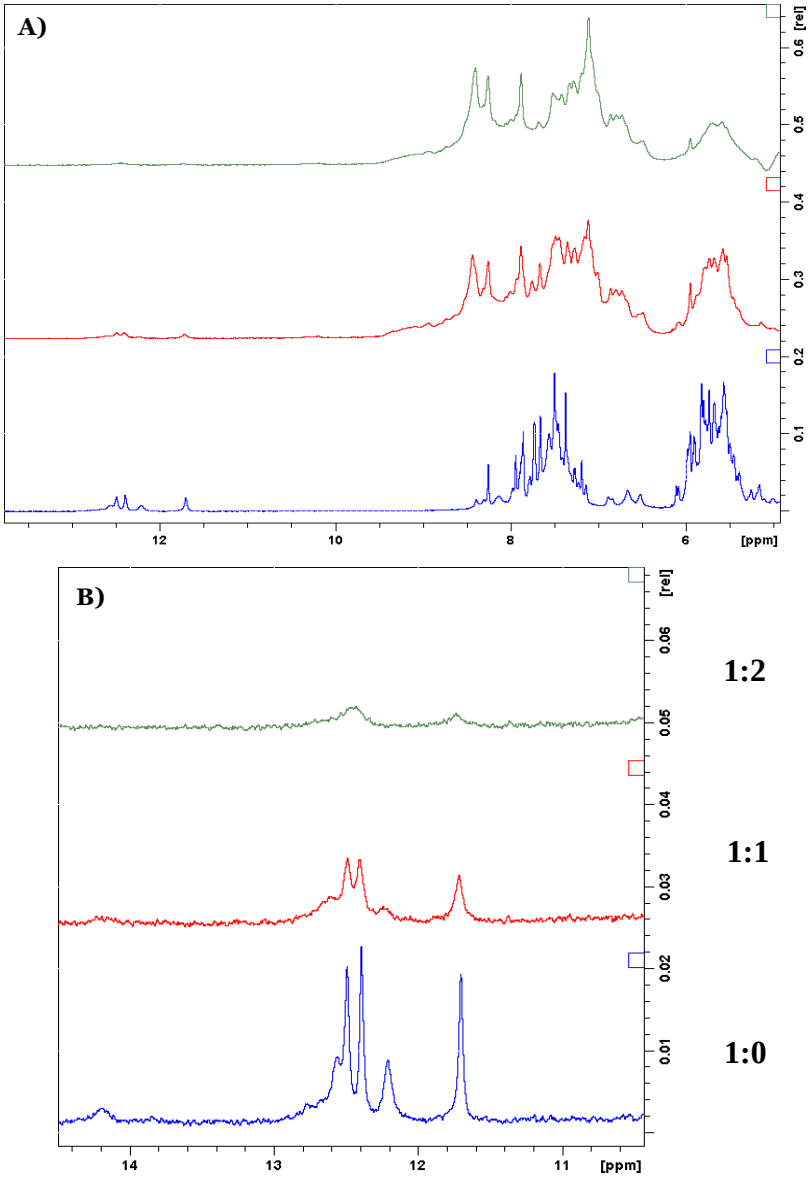

Figure 16 – NMR titration of RNA (80 μM) with increasing concentrations of nucleolin. A) Full spectra. B) Hairpin and duplex region. The blue lines correspond to the spectra of 80 μM of RNA, the red lines to 80 μM of RNA and 80 μM of NCL and the green lines to 80 μM of RNA and 160 μM of NCL.

By analyzing Figure 16, when NCL is not present, two well defined set of signals can be observed, in the imino region, corresponding to the RNA duplex and hairpin (12.5 - 14 ppm) and in the aromatic regions of the RNA (6.0 – 8.0 ppm). Upon titration with 1 molar equivalent of NCL, the NMR spectra showed a pronounced effect on the RNA structure, since the intensity of the peaks in these two regions decreased, especially in hairpin/duplex region, and became broader, in aromatic region of the RNA. Furthermore, after addition of 2 molar equivalents of NCL, the signals related to duplex and hairpin are not detectable. These results suggest interaction of RNA and NCL, which was also proved by native PAGE results.

RNA interaction with nucleolin was further assessed by the acquisition of a ^{1}H STD-NMR spectra, represented in Figure 17.

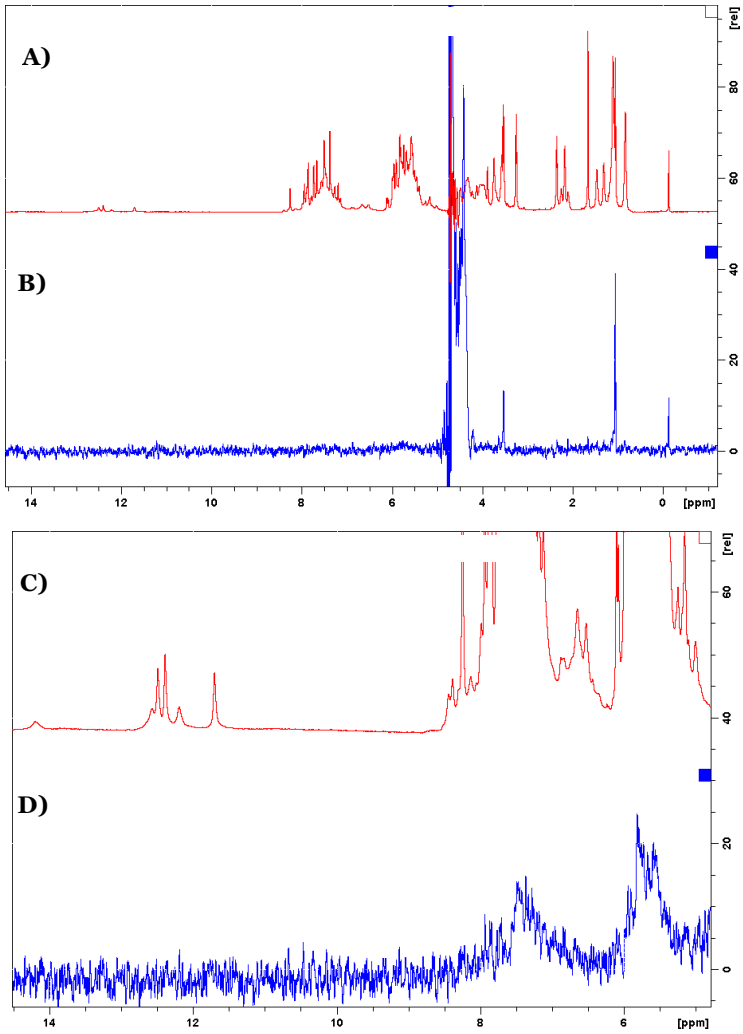

Figure 17 – Saturation transfer difference spectra of RNA (300 µM). A) Reference ^{1}H NMR spectrum of 300 µM RNA. B) ^{1}H STD-NMR of 300 µM RNA + 30 µM NCL. C) Reference ^{1}H NMR of 300 µM RNA + 30 µM of NCL. D) ^{1}H STD-NMR of 300 µM RNA + 30 µM NCL.

The ^{1}H NMR spectra of RNA and RNA+NCL are presented in Figure 17A and 17C, respectively. Figure 17B and 17D corresponds to the STD-NMR spectra of the RNA and RNA+NCL, respectively. The STD experiment of the complex RNA and NCL shows two signals, near the aromatic region of the RNA (6.0 – 8.0 ppm) (Figure 17D) that are not present in the STD spectra of free RNA (Figure 17B), which can indicate interaction of the RNA with NCL.

Overall, the results obtained by NMR and native PAGE suggest that the RNA can interact with NCL, however this interaction only starts occurring when NCL is in high concentration (1 RNA: 4 NCL) relatively to the RNA.

4.1.3.1 Agarose gel electrophoresis

Agarose gel electrophoresis technique allowed the study of the efficacy of labeling RNA-SH with FITC-NHS, which was used in confocal microscopy and fluorescence experiments. Briefly, to synthesize RNA-FITC, the RNA was reduced with TCEP and several washes were performed to remove TCEP in excess. Then, FITC-NHS was activated with PDEA and incubated overnight with RNA-SH. After overnight incubation, RNA-FITC was recovered by precipitation with NaCl and ethanol. The gel is presented in Figure 18.

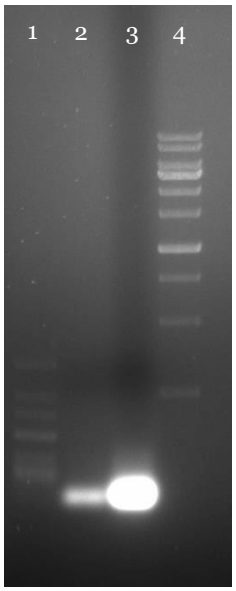

Figure 18 – Agarose gel electrophoresis to prove the efficacy of labeling of RNA-SH with FITC-NHS. Lane 1: 25 kb marker. Lane 2: 1 µg of RNA. Lane 3: 1 µg of RNA-FITC. Lane 4) 1 kb marker.

The results show two bands in lanes 2 and 3, in the same weight, both corresponding to the RNA. This result suggests that the labeling of the RNA-SH with FITC-NHS was successfully achieved. In addition, the band in lane 3 is more intense than the band on

lane 2, which can be explained by the fluorescence of FITC-NHS, also proving the efficacy of labelling technique.

4.1.3.2 Fluorescence Spectroscopy

After confirming that the RNA interacts with NCL, binding affinity of RNA to C_8, dexamethasone and NCL was first attempted by SPR technique; however during immobilization of the RNA via thiol coupling was lower (the final response was 220.6 RU with RNA concentration of 25 µg/mL), not allowing binding affinity calculation with NCL. So, to determine binding affinity of the RNA to C_8, dexamethasone and NCL, fluorescence titrations were employed.

These experiments were performed following fluorescence emission of RNA-FITC or C_8, at 520 nm and 522 nm, respectively, in the absence and presence of increasing amounts of the titrated molecule. The binding plots were acquired by a non-linear regression analysis, using Graphpad Prism software, using the best fit possible between Hill, Michaelis-Menten or two site-bind equations.

Firstly, RNA affinity to C_8 and dexamethasone were determined. The obtained results are represented in Figure 19A and 19B, respectively.

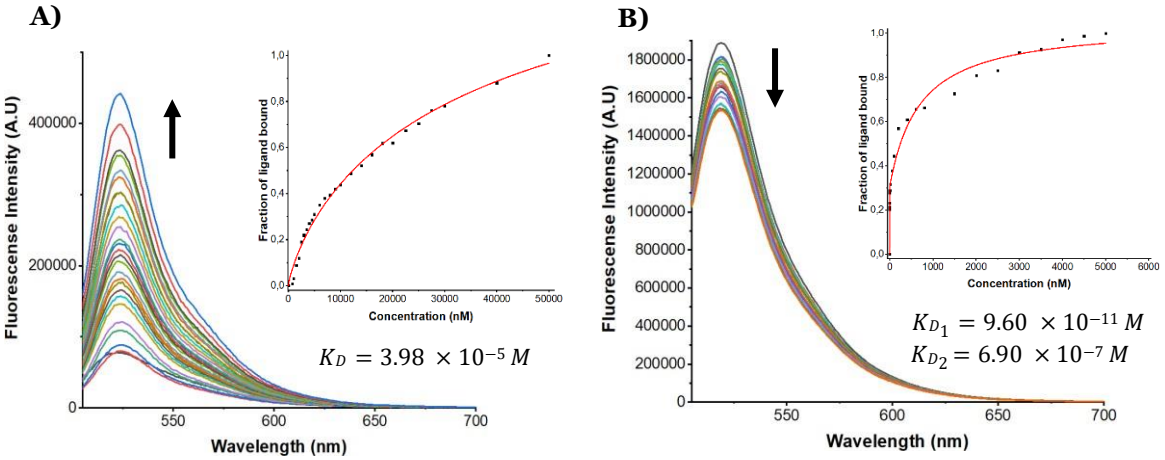

Figure 19 – Fluorescence titrations to determine RNA affinity to C_8 and dexamethasone. A) Fluorescence emission spectra of C_8 (5 µM) with increasing concentration of RNA in 100 mM KCl and 20 mM KPi, pH 7.1. The fraction of ligand-bound plots fitted to the saturation binding equation (Hill equation). B) Fluorescence emission spectra of RNA-FITC (1 µM) with increasing concentration of dexamethasone in 100 mM KCl and 20 mM KPi, pH 7.1. The fraction of ligand-bound plots fitted to the saturation binding equation (two site bind equation).

By analyzing Figure 19A, we can notice an increase in the fluorescence units. However, at saturating levels of RNA, there is no stabilization of fluorescence values, indicating a low affinity of RNA to C_8, showed by obtained K_D of 3.98×10^{-5} M. In Figure 19B, we can observe a decrease in fluorescence units at saturating levels of dexamethasone, generating two dissociation constants: $K_{D1} = 9.60 \times 10^{-11}$ M and $K_{D2} = 6.90 \times 10^{-7}$ M, respectively. Thus, the results indicate a higher affinity of RNA to dexamethasone, when compared to C_8.

Then, RNA affinity to NCL was calculated in the absence and presence of C_8 and dexamethasone. The results are depicted in Figure 20A, 20B and 20C.

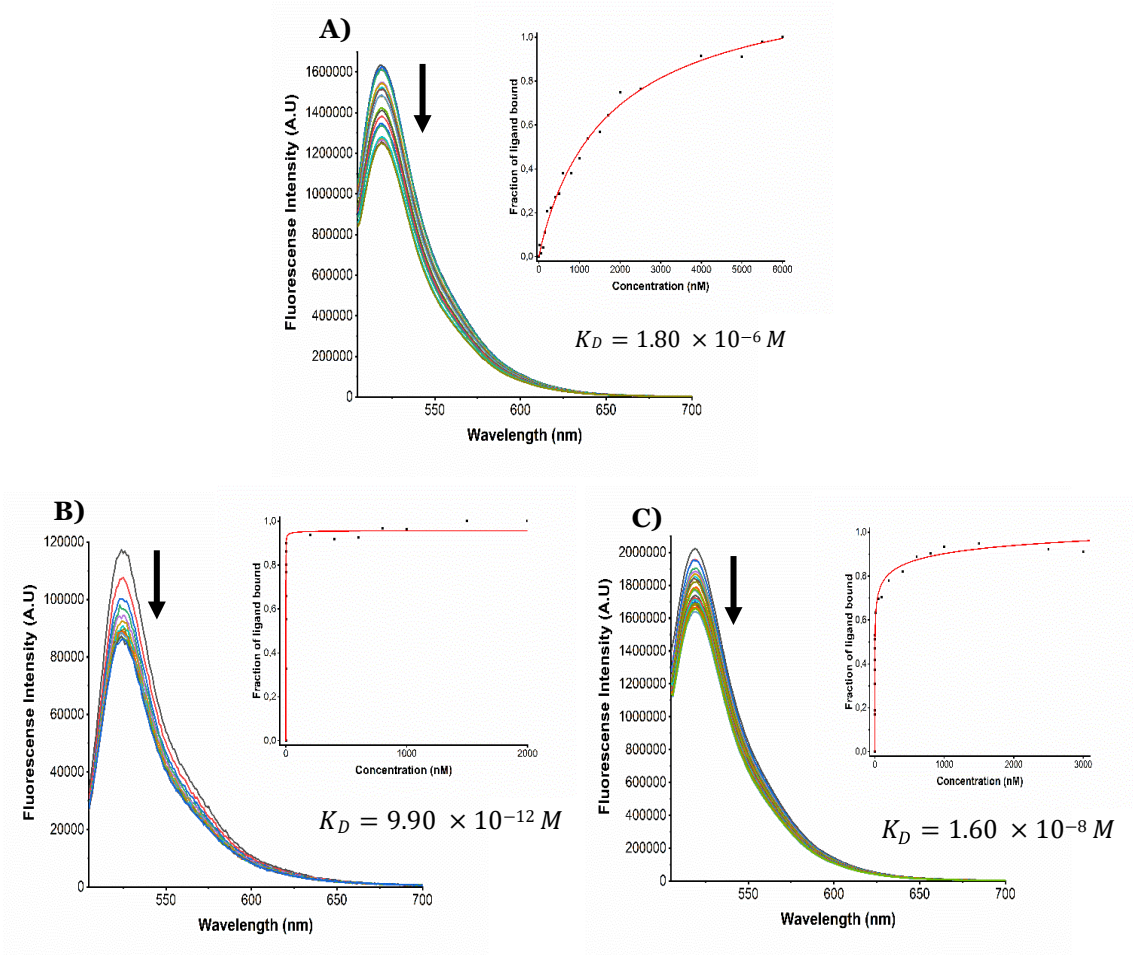

Figure 20 – Fluorescence titrations to determine RNA affinity to NCL in absence and presence of C_8 and dexamethasone in 100 mM KCl and 20 mM KPi, pH 7.1. A) Fluorescence emission spectra of RNA-FITC (1 µM) with increasing concentration of NCL. The fraction of ligand-bound plots fitted to the saturation binding equation (Hill equation). B) Fluorescence emission spectra of C_8 (5 µM) conjugated with 1 µM of RNA-FITC with increasing concentration of NCL. The fraction of ligand-bound plots fitted to the saturation binding equation (Hill equation). C) Fluorescence emission spectra of RNA-FITC (1 µM) conjugated with 5 µM of dexamethasone with increasing concentration of NCL. The fraction of ligand-bound plots fitted to the saturation binding equation (Hill equation).

Relatively to Figures 20A, 20B and 20C, we can observe that RNA has an affinity to NCL with a K_D of 1.80 × 10^{-6} M, at saturating levels of protein and that dissociation constant decreases when C_8 and dexamethasone are present, with K_D 9.90 × 10^{-12} M and 1.60 × 10^{-8} M, respectively. These results suggest that RNA has a higher affinity to NCL when is interacting with C_8 and dexamethasone, more pronounced in the case of C_8.

Finally, and to elucidate the obtained results, C_8 affinity to NCL was calculated, being the results represented in Figure 21.

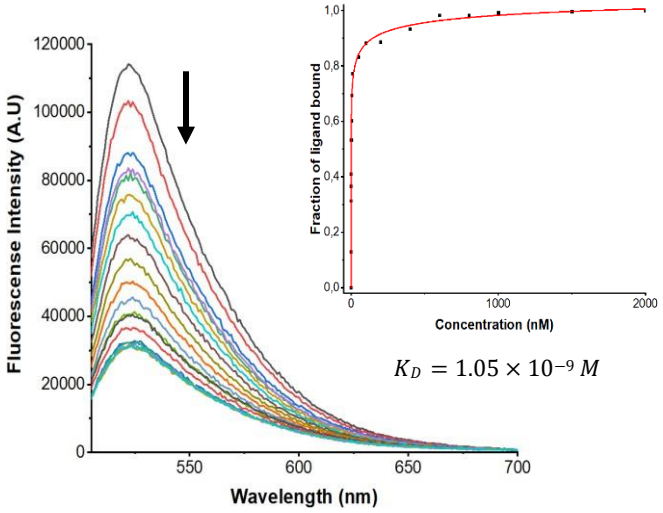

Figure 21 – Fluorescence titrations to determine C_8 affinity to NCL. Fluorescence emission spectra of C_8 (5 uM) with increasing concentration of NCL in 100 mM KCl and 20 mM KPi, pH 7.1. The fraction of ligand-bound plots fitted to the saturation binding equation (Hill equation).

By analyzing Figure 21, we can observe that C_8 has an affinity to NCL with a K_D of 1.05 × 10^{-9} M, at saturating levels of protein. This result suggests that C_8 has higher affinity to NCL when compared to the RNA, since the obtained dissociation constant of C_8 when titrated with NCL is lower than the obtained in the titration of the RNA with NCL (K_D = 1.80 × 10^{-6} M). However, and although C_8 showed higher affinity to NCL, we can not conclude that the affinity to NCL when both C_8 and the RNA are present is due to C_8, since the dissociation constant is lower when compared to free C_8 (K_D = 9.90 × 10^{-12} M).

4.2 Characterization of Drug Delivery Systems

Functionalization of gold nanoparticles with thiolated RNA containing C_8 or dexamethasone was achieved using a method adapted from the one previously described by Malik et al. [99]. Thiolated RNA was first reduced with 10 mM TCEP. After that, the reduced RNA was added to 5 nm colloidal gold nanospheres. After overnight incubation, salt ageing was performed by adding NaCl. To remove excess salts in solution dialysis was performed. Then, C_8 or dexamethasone were supramolecular assembled in the RNA functionalized gold nanoparticles.

RNA functionalized liposomes with C_8 or dexamethasone encapsulated were formulated using three lipids, CHOL, DSPE-PEG and PG. Firstly, the lipids were mixed, and chloroform was allowed to evaporate overnight. Afterwards, the lipids were solubilized in PBS containing C_8 or dexamethasone. Subsequently, five cycles of freeze and thaw were performed, followed by multiple extrusion steps (11 times) to uniformize the size of liposomes encapsulating C_8 or dexamethasone. Then, five washes were carried. To functionalize liposomes with RNA, liposomes were activated with PDEA and incubated with TCEP reduced RNA. Finally, the RNA- functionalized liposomes encapsulating C_8, or dexamethasone were washed five times.

4.2.1 Dynamic Light Scattering (DLS) and Nanoparticle Tracking Analysis (NTA)

DLS was performed to assess the size and PDI of liposomes and gold nanoparticles, as presented in Tables 9 and 10. PDI is a measurement of the heterogeneity of a sample based on size, and the lower its the value, the better the quality of the sample [104].

Table 9 – Hydrodynamic diameter and PDI of the gold nanoparticles.

	Hydrodynamic Diameter (nm) ± Standard Error	**PDI**
Gold Nanoparticles	11.70 ± 1.20	0.30
RNA– Gold Nanoparticles	21.04 ± 4.99	0.40
RNA– Gold Nanoparticles with C_8	21.66 ± 7.46	0.40
RNA– Gold Nanoparticles with dexamethasone	20.74 ± 6.48	0.42

By examining Table 9, the starting gold nanoparticles, in citrate buffer, as expected, showed the smallest size. When RNA was attached to the surface of gold nanoparticles, the size increased, from a hydrodynamic diameter of 11.70 ± 1.20 nm to 21.04 ± 4.99 nm. Finally, after washes and supramolecular assembly of C_8 and dexamethasone, the hydrodynamic diameter increased to values of 21.66 ± 7.46 nm and 20.74 ± 6.48 respectively. Additionally, PDI of the gold nanoparticles was measured. We can verify that after each step, the PDI of gold nanoparticles increase, due to the addition of reagents used during synthesis and the small size of the nanoparticles.

The synthesis of RNA gold nanoparticles containing C_8 or dexamethasone was achieved using a similar method from the one previously described by Malik et al., who developed and characterized AS1411 coated gold nanoparticles [99]. A commercial solution of colloidal 5 nm gold nanoparticles was used, such as in this dissertation. The AS1411 functionalized gold nanoparticles were characterized for hydrodynamic diameter and displayed a size of 33.0 ± 3.4 nm, a value similar to the obtained for RNA coated gold nanoparticles (21.04 ± 4.99) [99]. In addition, Lopes-Nunes et al. developed AS1411 functionalized 5 nm gold nanoparticles to deliver C_8, using the same method present in this dissertation [105]. The results showed that the starting gold nanoparticles presented a size of 12.00 ± 1.20 nm [105]. After functionalization with AS1411, the size of the gold nanoparticles increased to 15.76 ± 1.64 nm [105]. Finally, after the supramolecular assembly with C_8, the gold nanoparticles presented a hydrodynamic diameter of 21.16 ± 2.68 nm [105]. Comparing the values obtained with those of this dissertation, we can see that they are quite similar, there being only a greater difference after functionalization with the aptamer AS1411, which can be possibly explained by differences in the used RNA and the AS1411.

Table 10 – Hydrodynamic diameter and PDI of the liposomes.

	Hydrodynamic Diameter (nm) ± Standard Error	**PDI**
Liposomes	164.20 ± 60.28	0.13
Liposomes with C_8	160.30 ± 52.80	0.13
Liposomes with dexamethasone	161.40 ± 59.95	0.14
RNA-Liposomes with C_8	157.50 ± 70.30	0.24
RNA-Liposomes with dexamethasone	156.50 ± 63.76	0.20

Regarding the hydrodynamic analysis achieved by DLS technique, the starting liposomes showed a hydrodynamic diameter of about 164.20 ± 60.28 nm. When C_8 or dexamethasone were encapsulated in the liposomes and washes were done, the size changed to 160.30 ± 52.80 and 161.40 ± 59.95 nm respectively. Finally, after functionalization with RNA, the hydrodynamic diameter was 157.50 ± 70.30 and 156.50 ± 63.76 nm, respectively. Concerning the PDI of the liposomes, we can verify that after each step, the PDI is almost constant at values lower than 0.25, and the data meet the quality criteria.

Previously, Yu Li et al. developed AS1411 derived aptamer functionalized liposomes containing CIS. The liposomes were formulated from phosphatidylcholine (HSPC), CHOL, and (mPEG2000-DSPE) at a molar ratio of 2:1:0.16, very similar to the ones developed in this dissertation. constituted by HSPC, CHOL, and DSPE-PEG at a molar ratio of 2:1:0.16 [106]. They reported that the aptamer functionalized liposomes presented a size close to 200 nm of diameter, a value in the same range of the liposomes developed in this dissertation, 164.20 nm [106]. Later, the same group, developed aptamer functionalized liposomes containing DOX, with the same constitution and lipid ratio as those previously developed, for targeted anticancer chemotherapy with a final size of about 190 nm, a value closer to the developed liposomes when compared to the previous work [107].

Moreover, Liao et al. developed and characterized AS1411 conjugated liposomes containing DOX and a bubble generating agent to target DOX-resistant breast cancer cells [108]. The liposomes, constituted by dipalmitoylphosphatidylcholine (DPPC), CHOL and DSPE-PEG, were prepared by film hydration method followed by sequential extrusion, a method similar to the applied in this dissertation [108]. The DLS technique was used to evaluate the size of the liposomes, and the results showed that functionalization with AS1411 increased the size of the liposomes from 127.10 ± 31.80 nm to 172.20 ± 43.90 nm. The size of the AS1411 liposomes obtained in this work is also very similar to the RNA coated liposomes developed in this dissertation [108].

NTA technique was used to characterize the size and concentration of liposome samples. The mean sizes and concentration obtained by NTA results are displayed in Table 11.

Table 11 – Mean size and concentration of liposomes obtained by NTA technique.

	Mean size ± standard error	**Concentration (particles/mL)**
Liposomes (100x dilution)	157.50 ± 2.80	$5.64 \times 10^8 \pm 4.10 \times 10^8$
RNA-Liposomes with C8 (100x dilution)	154.40 ± 1.60	$5.71 \times 10^7 \pm 5.85 \times 10^6$

By analyzing Table 11 and comparing the obtained mean sizes to the obtained by the DLS technique, we can conclude that the mean size values obtained by NTA are slightly smaller. The standard error obtained by NTA technique was smaller than the obtained by the DLS. Moreover, the number of particles *per* mL obtained for the RNA functionalized liposomes with C_8 sample was lower than the concentration of particles per mL obtained for the liposomes sample, which can be explained by the greater number of steps involved in the purification of the sample containing C_8 and RNA, leading to a possible loss of particles. While DLS measurements are faster, NTA technique requires several optimization steps, that allow the identification of the most suitable settings for the video capture and analysis. In addition, DLS can automatically adjust the attenuator to adapt to a wide range of sample concentrations, while in NTA, the search for the right sample concentration for a successful measurement may need more time and require various dilution steps [100].

4.2.2 SEM and TEM imaging

SEM and TEM allowed the study of the morphology of liposomes and gold nanoparticles, respectively, as represented in Figures 22 and 23.

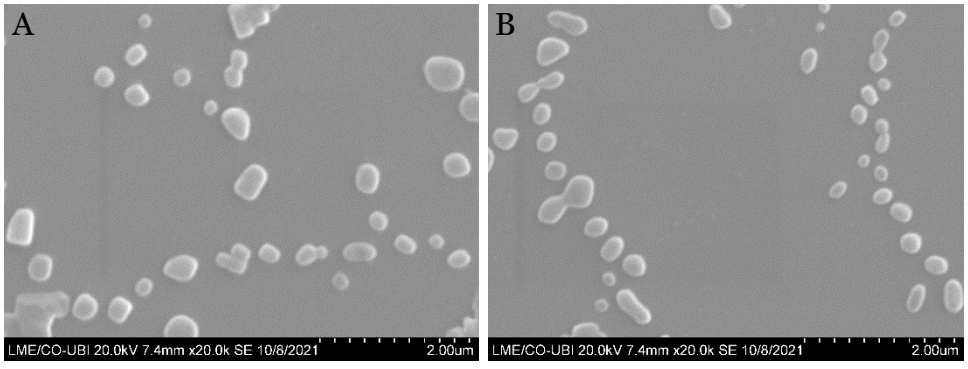

Figure 22 - SEM images of (A) RNA-liposomes carrying C_8 and (B) RNA liposomes carrying dexamethasone.

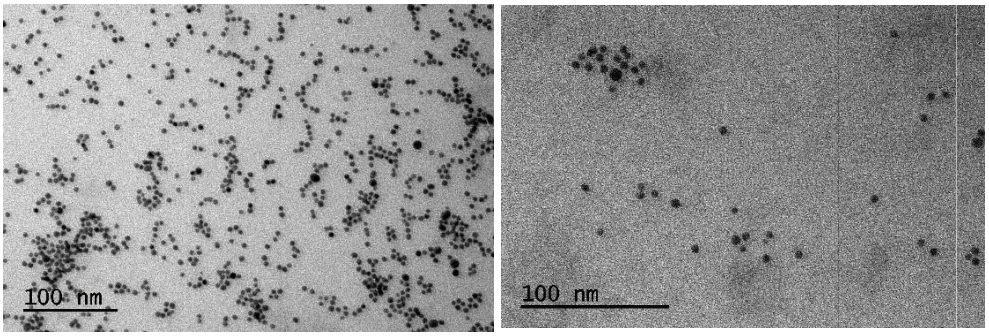

Figure 23 - TEM imaging of gold nanoparticles.

As observed in Figure 22, the liposomes present a uniform size and are not aggregated. When C_8 and dexamethasone were encapsulated, the liposomes with C_8 (Figure 22A) and with dexamethasone (Figure 22B) also presented a uniform size and distribution, without any aggregation. In Figure 23, the gold nanoparticles also present a uniform size and no aggregation, with 100x dilution. When the solution is concentrated, the gold nanoparticles showed some aggregation.

4.2.3 Stewart Assay

Stewart Assay provides a fast and easy method to determine phospholipids in solution [109], [110]. The mechanism involved in this technique involves the formation of a soluble 1:1 complex between the phospholipid and AF [109], [110]. There are several phospholipids that react with AF and thus can be quantified by this technique, namely L-3-lecithin, sphingomyelin, lysolecithin, phosphatidyl ethanolamine, and phosphatidyl serine[110]. However, phospholipids like PG do not react with AF, therefore, cannot be quantified by this method [110]. It is important to note that when two quantifiable lipids are present, the absorbance readings may be incorrect [109], [110].

The amount of DSPE-PEG, a quantifiable phospholipid by this technique, present in a liposome solution was determined by the Stewart Assay. Figure 24 represents the standard curve of concentration of DSPE-PEG vs absorbance at 488 nm of DSPE-PEG chloroform layer of standard solutions.

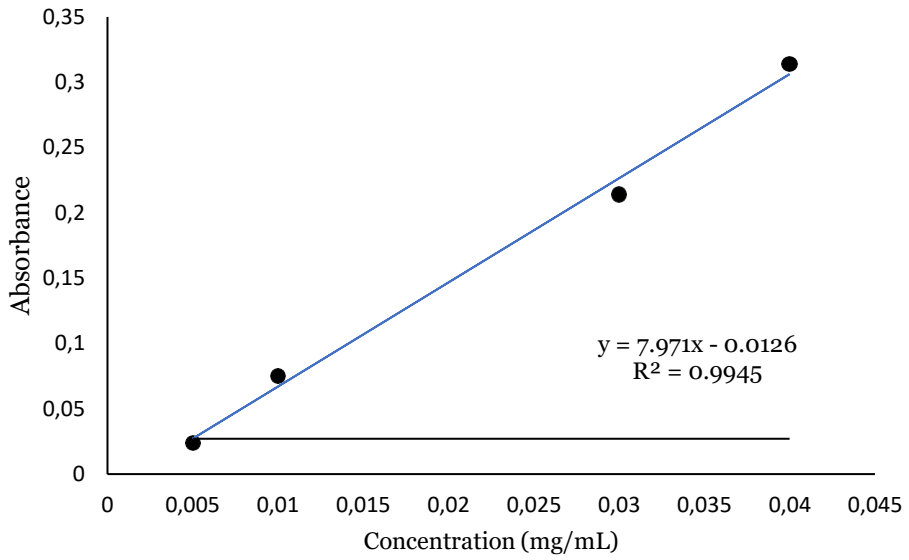

Figure 24 – Changes in absorbance (488 nm) of the chloroform phase upon increasing concentrations of DSPE-PEG (0.005-0.004 mg/mL). Plotted standard curve (optical density vs mg of DSPE-PEG).

Figure 24 reveals a linear relation between the absorbance of the chloroform layer and the concentration of DSPE-PEG in the studied range of solutions (0.005 mg/mL to 0.04 mg/mL), obtaining the equation y=7.971x – 0.0126, used to extrapolate the concentration of DSPE-PEG present in liposome formulations, present in Table 12.

Table 12 – Concentration of lipids (DSPE-PEG, CHOL and PG) in liposome formulations.

	Absorbance (488 nm)	**[DSPE-PEG] (mg/mL)**	**[CHOL] (mg/mL)**	**[PG] (mg/mL)**
RNA-Liposomes	0.026	9.66×10^{-2}	1.21	6.05×10^{-1}
RNA-Liposomes with C_8	0.022	8.68×10^{-2}	1.09	5.43×10^{-1}
RNA-Liposomes with dexamethasone	0.021	8.43×10^{-2}	1.05	5.27×10^{-1}

After having determined the DPSE-PEG concentration in the liposomes, the concentration of CHOL and PG was obtained based on the ratio used in liposomes formulation, CHOL 1: PG 2: DSPE-PEG 0.16.

4.2.4 Encapsulation Efficiency

The quantity of encapsulated C_8 and dexamethasone on liposomes was determined by UV-vis spectroscopy. Firstly, standard curves were constructed by measuring the absorbance of different standardized concentrations of C_8 (10 μM, 15 μM, 20 μM, 25 μM and 30 μM) at 496 nm and dexamethasone (25 μM, 50 μM, 75 μM and 100 μM) at 245 nm, represented in Figures 25 and 26.

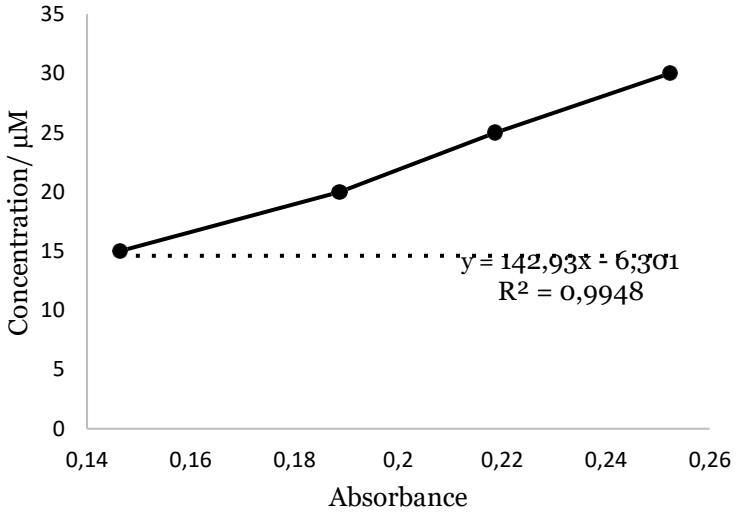

Figure 25 – C_8 calibration curve with different standardized concentrations (10 μM, 15 μM, 20 μM, 20 μM, 25 μM and 30 μM).

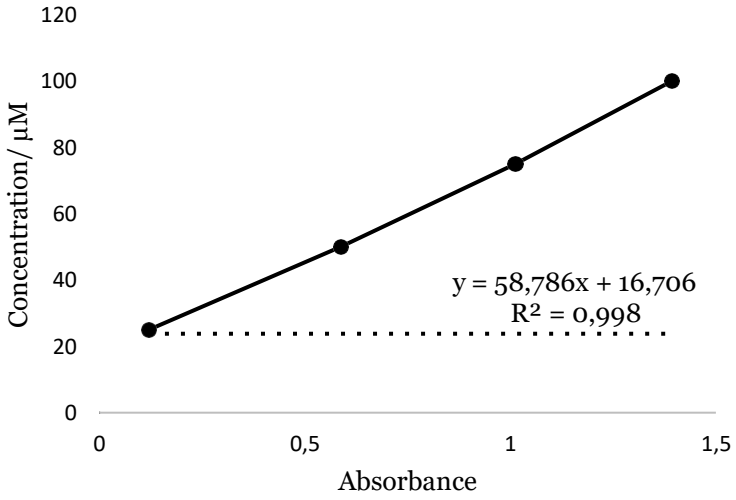

Figure 26 – Dexamethasone calibration curve with different standardized concentrations (25 μM, 50 μM, 75 μM, 100 μM).

After obtaining standard curves, the concentration of encapsulated C_8 and dexamethasone were extrapolated. The obtained concentrations are represented in Tables 13 and 14.

Table 13 – Extrapolated concentrations of C_8 encapsulated in liposomes.

	Absorbance (496 nm)	**[C_8] (µM)**
RNA-Liposomes with C_8 (first synthesis)	0.466	60.30
RNA-Liposomes with C_8 (second synthesis)	0.565	74.45

Table 14 – Extrapolated concentrations of dexamethasone encapsulated in liposome.

	Absorbance (496 nm)	**[Dexamethasone] (µM)**
RNA-Liposomes with dexamethasone (first synthesis)	0.873	68.03
RNA-Liposomes with dexamethasone (second synthesis)	0.752	26.11

4.2.5 Native PAGE

Native PAGE technique was also used to evaluate the efficacy of liposome functionalization with RNA, being the results displayed in Figure 27.

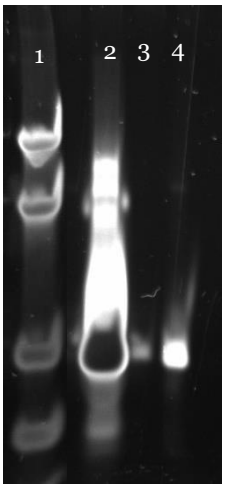

Figure 27 – Native PAGE experiment to evaluate efficacy of liposome functionalization with RNA. Lane 1: Marker (90,60,30,21 nt). Lane 2: 203.17 nM of RNA. Lane 3: 203.17 nM of RNA-SH. Lane 4: RNA functionalized liposomes.

We can observe that in lane 4 the band corresponding to RNA functionalized liposomes, has the same molecular weight as those presents in lanes 2 and 3, where the RNA and the RNA-SH were injected, respectively. These results suggest that the liposomes were effectively functionalized with the RNA, since the band corresponding to the RNA is present in the lane were liposomes after purification and washes process were injected.

4.2.6 NMR spectroscopy

^{1}H NMR spectra were acquired to evaluate the efficacy of liposomes functionalization with RNA. The results are presented in Figure 28.

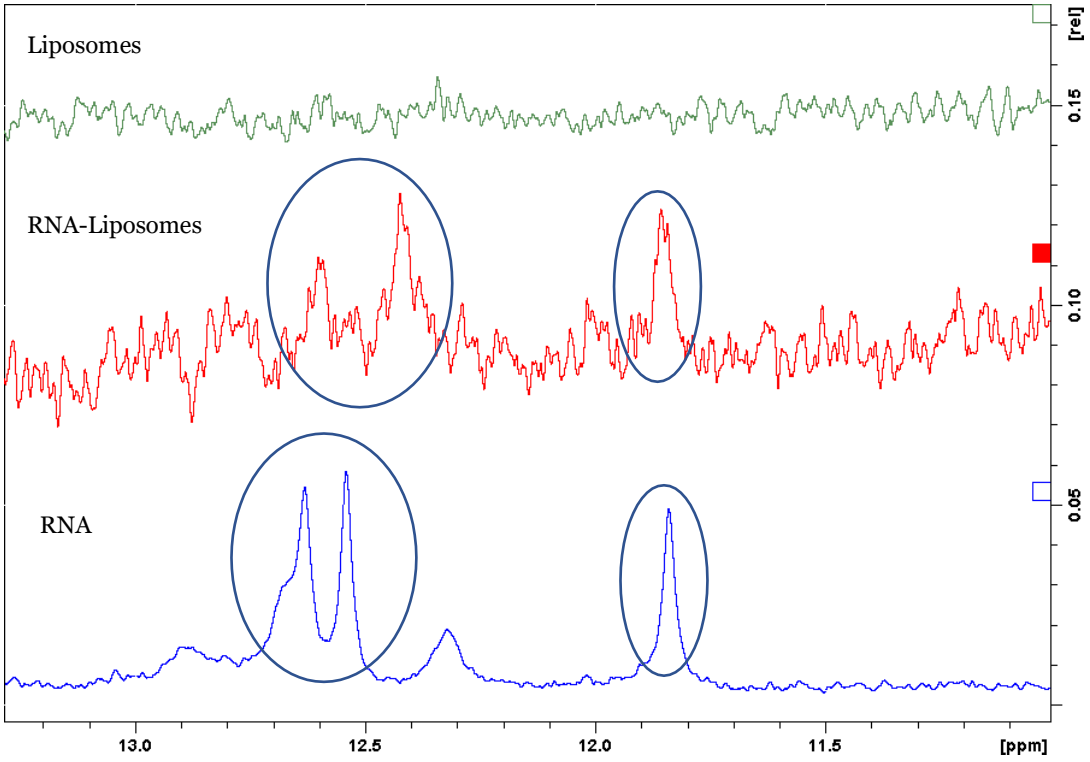

Figure 28 – NMR spectra of liposomes, RNA-coated liposomes, and RNA.

The result obtained by NMR confirmed the obtained by the native PAGE technique, since in the spectrum of the corresponding to the liposomes functionalized with RNA, we can see peaks corresponding to the RNA hairpin and duplex region that are not visible in the NMR spectrum of the non-functionalized liposomes, thus proving the effectiveness of the functionalization.

4.3 In vitro Studies

4.3.1 Cell Viability Assays

The effects of C_8, dexamethasone, and RNA on cell viability were assessed by MTT assays performed after 72 h of incubation using two cell lines, the non-malignant NHDF and malignant SCC-154 cells, as mentioned in section 2.4.1. The results are displayed in Table 15 and Figure 29.

Both ligands decreased the viability of SCC-154 cancer cells, being C_8 with the highest cytotoxic potential (IC_{50} = 0.22 μM), which was able to decrease cell viability at lower concentrations than dexamethasone (IC_{50} = 88.01 μM). Regarding NHDF cells, the results are different for each ligand. Regarding C_8, a similar effect to the one obtained in SCC-154 malignant cells (IC_{50} = 0.31 μM) was observed. However, dexamethasone presents a greater selectivity for cancer cells, since the IC_{50} value is higher in non-malignant NHDF cells (IC_{50} = 153.80 μM). Relatively to the RNA, as observed in Figures 24A and 24B, it does not have relevant cytotoxic activity, so it was not possible to calculate the IC_{50} value.

Previous studies, performed with C_8, demonstrated that this molecule is highly toxic to both normal and cancer cell lines [111]–[113]. After three days of incubation, the obtained IC_{50} values of free C_8 were 0.26 μM, 0.10 μM and 0.27 μM for HeLa, HEC-1-A and NHDF cells, respectively. These values are similar with those presented in this dissertation (Table 14). Regarding dexamethasone, there are not many studies in cancer cell lines since this drug is mostly used as an anti-inflammatory [93]. However, Wang et al. assessed the IC_{50} of this glucocorticoid in non-small cell lung cancer (NSCLC) cell lines A549 and H1299. Dexamethasone displayed mild cytotoxicity to the NSCLC cancer, with IC_{50} values higher than 500 μM, after 48h of incubation [114]. In addition, Pantea et al. investigated the anti-proliferative effects of dexamethasone on human cancer HT-29 cell line after 48 h of incubation. The results showed that the IC_{50} value of dexamethasone was 1000 μM [115].

Thus, the IC_{50} values calculated in this work demonstrate that C_8 and dexamethasone have cytotoxic potential to be applied in a drug delivery system, which can enhance their activity in malignant cells, with reduce effect in non-malignant cells.

Table 15 – IC_{50} calculated values for C_8 and dexamethasone on NHDF and SCC-154 cell lines.

	IC_{50} NHDF (μM)	**IC_{50} SCC-154 (μM)**
C_8	0.31	0.23
Dexamethasone	153.80	192.80

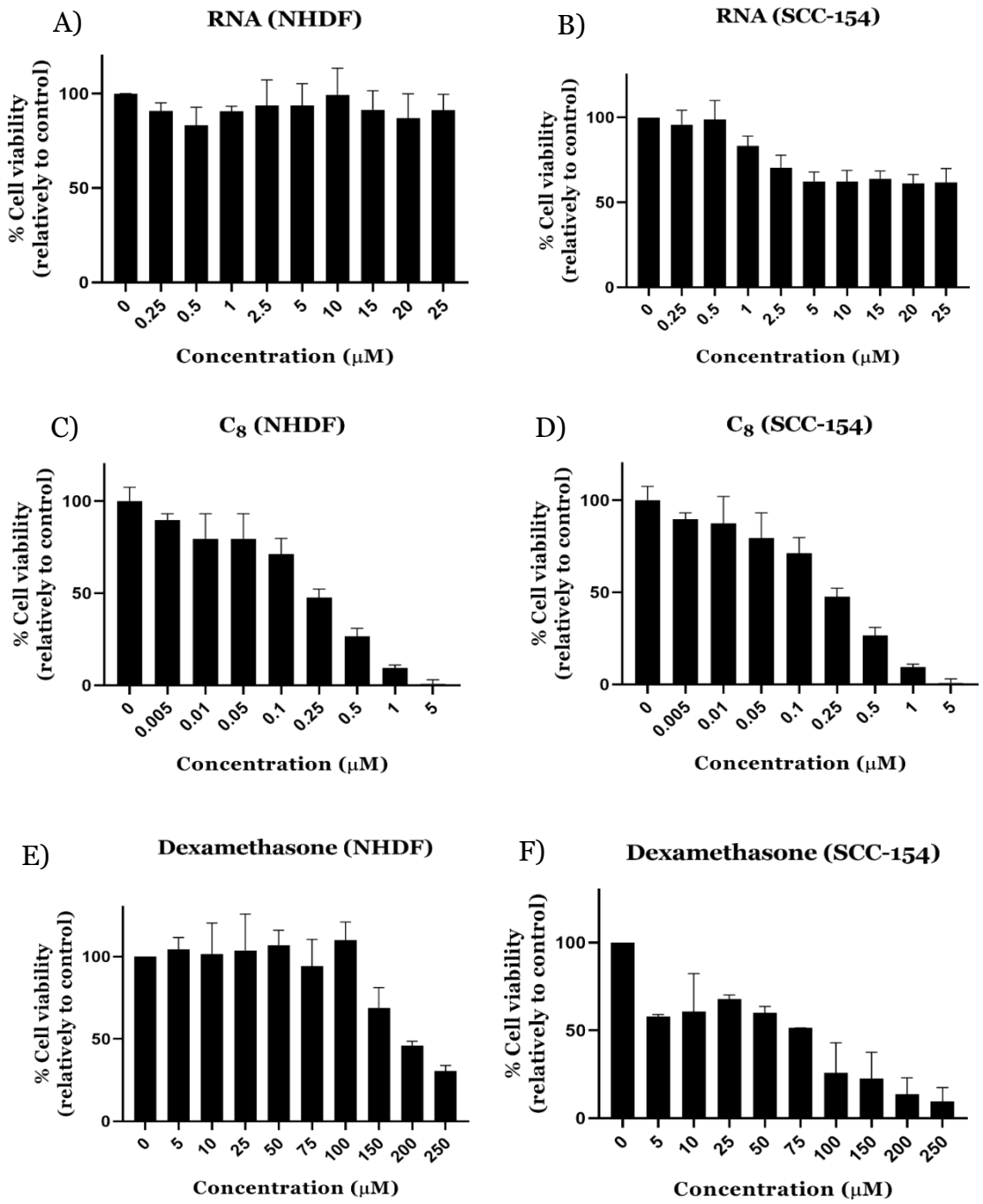

Figure 29 – MTT viability assays in NHDF and SCC-154 cells of A) RNA, B) C_8, C) dexamethasone and in SCC-154 cells of B) RNA, D) C_8 and F) dexamethasone, respectively.

After determining the IC_{50} values for C_8, dexamethasone and free RNA, MTT assays were performed for the RNA supramolecular assembled with C_8 and dexamethasone. To achieve this, a fixed RNA concentration of 5 μM was selected, which corresponds to the lowest value where some reduction in cell viability was observed in SCC-154 malignant cells, as shown in Figure 28B, and C_8 and dexamethasone concentrations were the same studied before (0.005, 0.01, 0.05, 0.1, 0.25, 0.5, 1 and 5 μM for C_8 and 5, 10, 25, 50, 75, 100, 150, 200 and 250 μM for dexamethasone). The cell viability results are displayed in Figure 30.

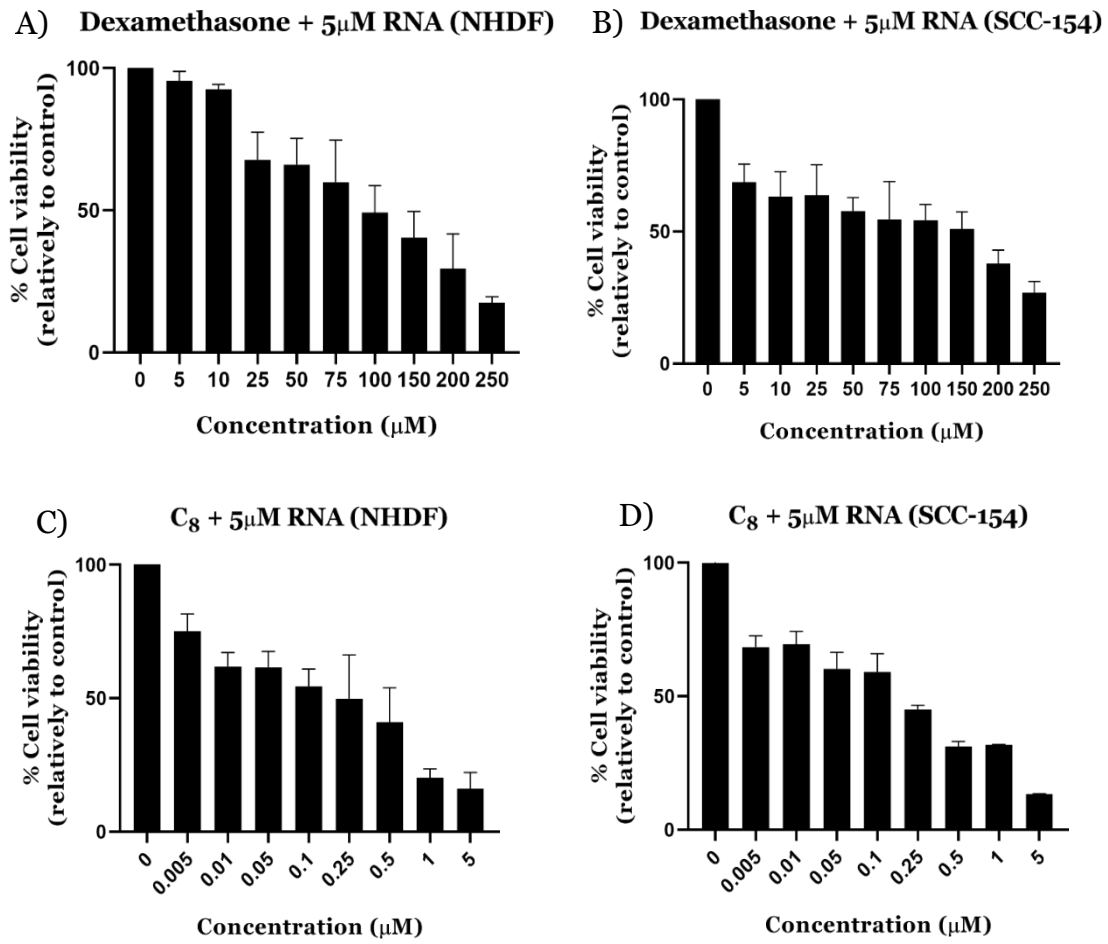

Figure 30 – MTT viability assays in NHDF of 5 μM of RNA with A) dexamethasone and C) C_8. MTT viability assays in SCC-154 cells of 5 μM of RNA with B) dexamethasone and D) C_8.

Overall, the RNA-C_8 and RNA-dexamethasone conjugates showed lower cellular toxicity in both malignant and non-malignant cells, being more evident in the case of the RNA with C_8. In addition, RNA-C_8 and RNA-dexamethasone showed similar cytotoxicity towards NHDF and SCC-154 cells. These results suggest that the RNA has an inhibitory effect on C_8 and dexamethasone cytotoxicity. Similar results were also observed in previous studies, in which aptamers were used as targeting agents [116]. For instance,

Carvalho et al. developed an aptamer (AT11-Lo)-guided acridine derivatives (C_3, C_5 and C_8) approach for cervical cancer therapy. When studying cell viability of AT11-Lo and acridine orange derivatives complexes, the obtained results were similar to the those presented in this dissertation, since the cell viability of the complexes was lower than free compounds, suggesting also an inhibitory effect from AT11-Lo [116].

Then, the in vitro cytotoxic effects of the RNA and gold nanoparticles functionalized liposomes carrying C_8 or dexamethasone were finally tested on NHDF and SCC-154 cells, using the MTT assay. However, only the results involving liposomes will be presented, since after several attempts, the assays with gold nanoparticles did not show analyzable results. Firstly, MTT assays with RNA functionalized liposomes carrying C_8 and dexamethasone were carried out. Different concentrations of encapsulated C_8 and dexamethasone were tested, and the results are displayed in Figure 31.

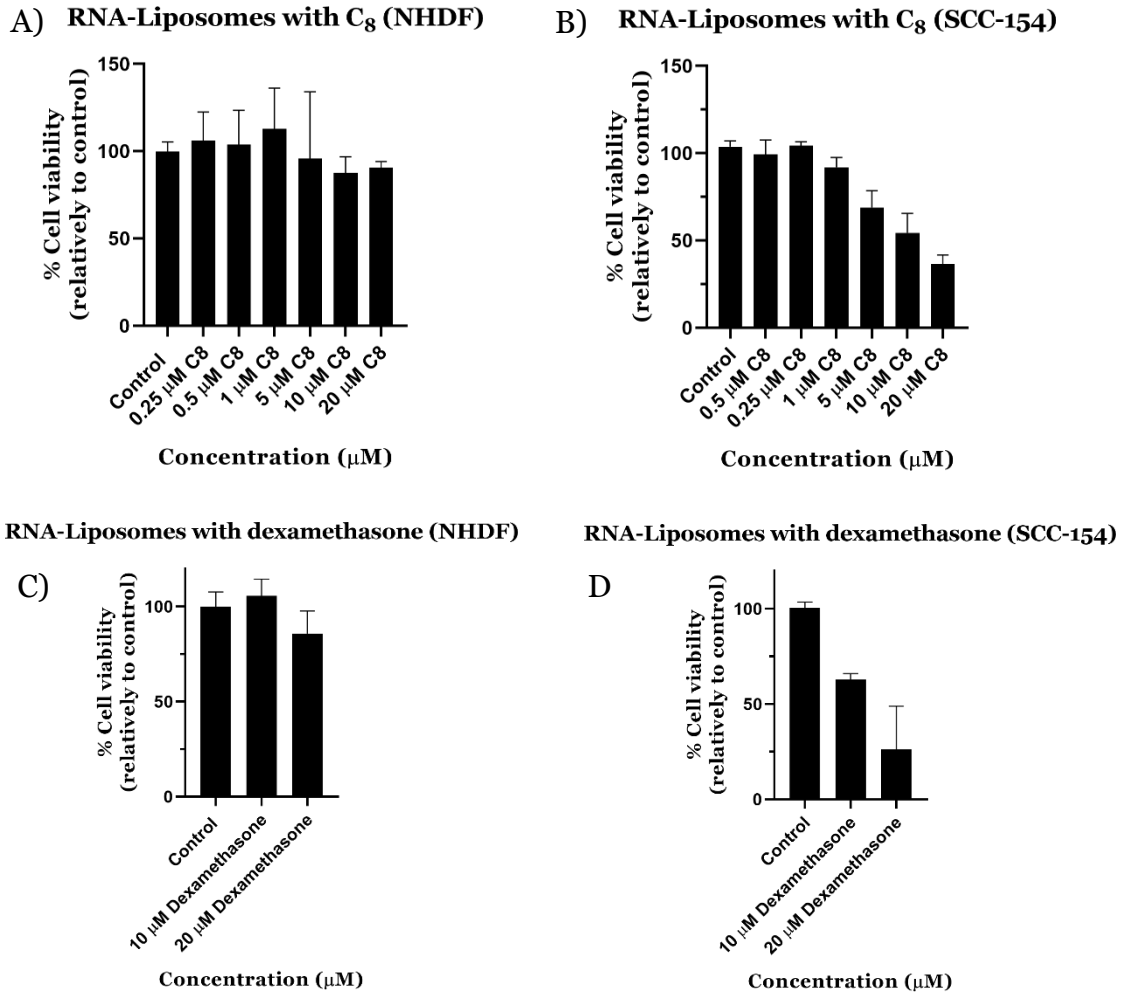

Figure 31 – MTT viability assays in NHDF (A and C) and SCC-154 cells of RNA functionalized liposomes carrying C_8 and dexamethasone.

By analyzing Figure 31, it is possible to observe that after stimulation with the RNA functionalized liposomes carrying C_8 or dexamethasone, there is a high reduction of cell viability in the malignant SCC-154 cells, while the viability of the non-malignant NHDF cells remains practically at 100%, showing that the developed drug delivery system is selective to malignant cells. Briefly, the best results were obtained with RNA functionalized liposomes carrying 20 μM of C_8 and dexamethasone.

In order to elucidate whether the cytotoxic effect was mainly due to C_8 and dexamethasone or due to the liposomes, MTT assays were performed with RNA functionalized liposomes, with the same concentration of the nucleic acid used in the previous assay with RNA functionalized liposomes carrying 20 μM of C_8 or dexamethasone. The comparative results are presented in Figure 32.

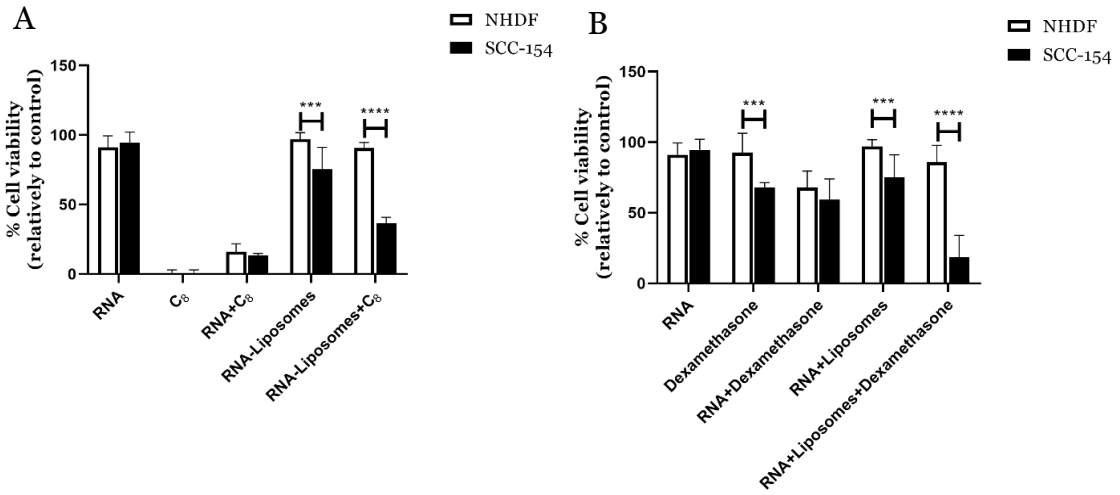

Figure 32 – Percentage of viable cells after incubation for 72 hours with RNA functionalized liposomes carrying A) 20 μM C_8 or B) 20 μM dexamethasone in NHDF and SCC-154 cells. *** $p<0.001$, **** $p<0.0001$.

By analyzing the results present in Figure 32, we can observe that there is a statistically significant difference between RNA functionalized liposomes when applied to non-malignant (NHDF) and malignant (SCC-154) cells and that difference becomes more evident when liposomes are loading C_8- or dexamethasone, suggesting a selective delivery of these molecules to SCC-154 malignant cells. In addition, in Figure 32B, it is also notable a statistically significant difference between free dexamethasone when applied to NHDF and SCC-154 cells.

Overall, MTT assays demonstrate that RNA-functionalized liposomes, besides acting as drug carrier of C_8 and dexamethasone, also presents an intrinsic therapeutic effect that

is potentiated with delivery of C_8 and dexamethasone, which present cytotoxic effect that can be controlled with their encapsulation on the liposomes.

4.3.2 Confocal Microscopy

Confocal fluorescence microscopy assays were performed on SCC-154 cells and allowed to assess the internalization and localization of the RNA within the cell, as well as to verify if the internalization was mediated by NCL. The nucleus of the cells was labeled with Hoechst 33342 (blue staining, with $\lambda_{excitation}$ = 405 nm and $\lambda_{emission}$ = 427 nm) or CyTRAK orange (red staining, with $\lambda_{excitation}$ = 555 nm and $\lambda_{emission}$ = 610 nm). NCL was labeled with Alexa Fluor 647 (red staining, with $\lambda_{excitation}$ = 650 nm and $\lambda_{emission}$ = 665 nm).To visualize the RNA, it was previously conjugated with FITC-NHS ($\lambda_{excitation}$ = 488 nm and $\lambda_{emission}$ = 515 nm).

Firstly, to verify RNA internalization, live cell imaging was performed. To achieve this, SCC-154 cells were incubated with 2 μM of Hoechst and 10 μM of RNA-FITC. By analyzing Figure 33, it is possible to note that the RNA-FITC internalized after 30 min. At the end of 1 h of incubation, RNA-FITC is observed inside the cells, namely in the cytoplasm and nucleus of the cells. After 1.5 h, internalization of the RNA-FITC is still visible, maintaining its cytoplasmic and nuclear localization. Lastly, after about 2 h most cells are stained by RNA. In summary, these results demonstrate that the RNA is able to internalize in the majority of SCC-154 malignant cells after 2 h and being located in the nucleus and cytoplasm of the cells. Similar results were also observed in the previous work developed by Magalhães et al., who developed the RNA used in this dissertation [101]. To illustrate that, Magalhães et al. incubated Min6B1, Bend3, and HeLa cells with fluorescently-labeled RNA for 1 h and then imaged cells by fluorescence microscopy [101]. The results showed punctate staining of the cells, supporting that the RNA was able to internalize and localize in the cytoplasm of the cells after 1h, however no staining of the nucleus was observed [101].

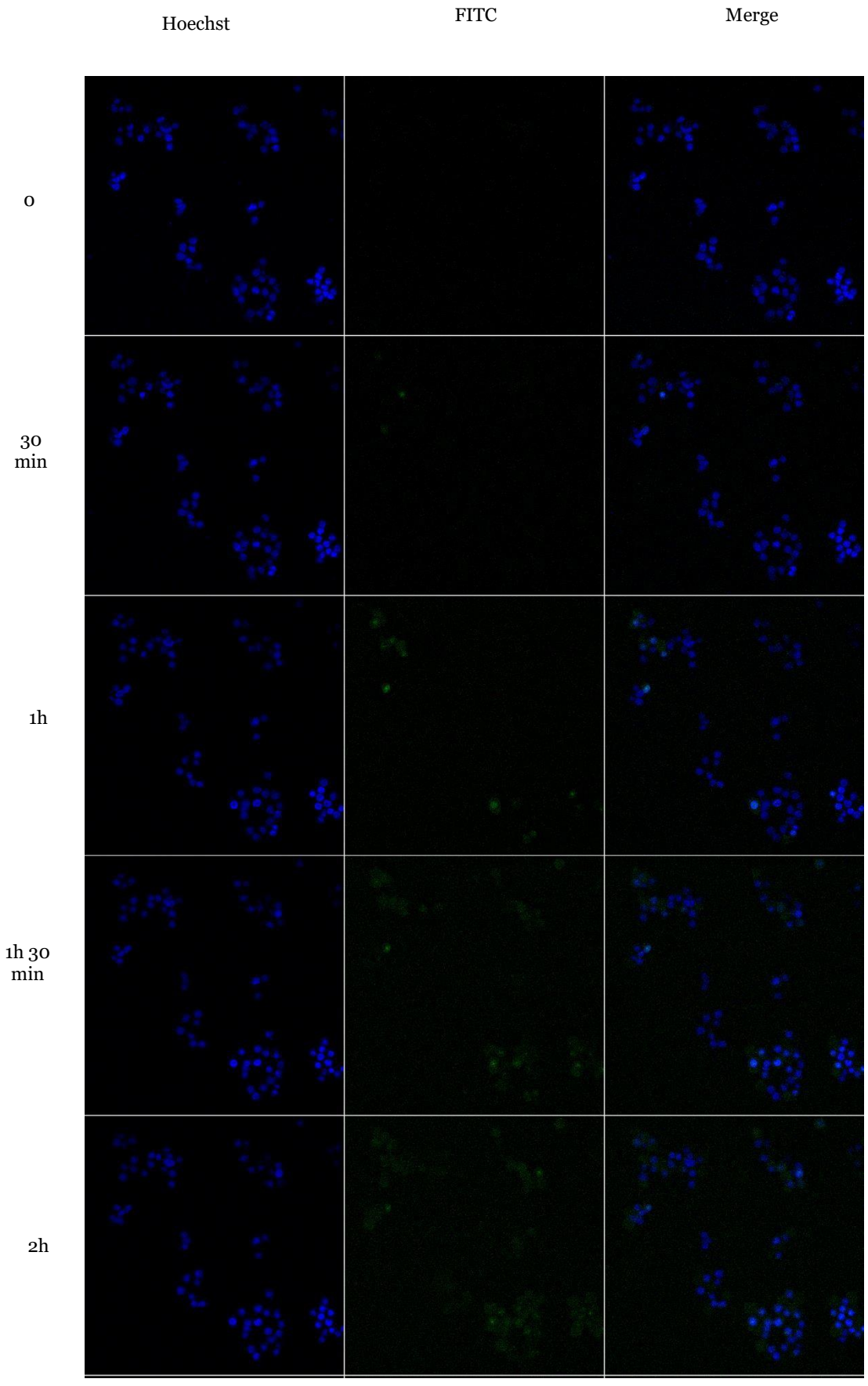

Figure 34 – Confocal microscopy live cell images of SCC-154 cells with 10 μM of RNA-FITC (green). The nuclear probe used was Hoechst 33342 (blue).

Then, to verify if the internalization was mediated by NCL, SCC-154 cells were incubated with primary anti-NCL antibody conjugated with the secondary antibody Alexa Fluor 647, to localize this protein in the cell surface. Then cells were washed and incubated with 10 μM of RNA-FITC for 2 h and with 2 μM of Hoechst, as depicted in Figure 34.

The results indicate that the RNA does not internalize into cells via NCL, and after 2 h there is no colocalization with the protein. This result is in agreement with that described by Magalhães et al., since they suggested that the mechanism of internalization on cells is via endocytosis [101]. To further elucidate the mechanism of uptake, the research group performed flow cytometry experiments with Jurkat and NHBE cells in the presence of a clathrin-mediated endocytosis (phenylarsine oxide) or a caveolin-mediated endocytosis (indomethacin). The results showed that the RNA is internalized into cells via clathrin-mediated endocytosis, since the treatment with phenylarsine oxide resulted in a slight decrease in overall fluorescent staining, that could be reduced to background levels following treatment with ribonucleases, and the treatment with indomethacin had little or no effect on the uptake into cells [101].

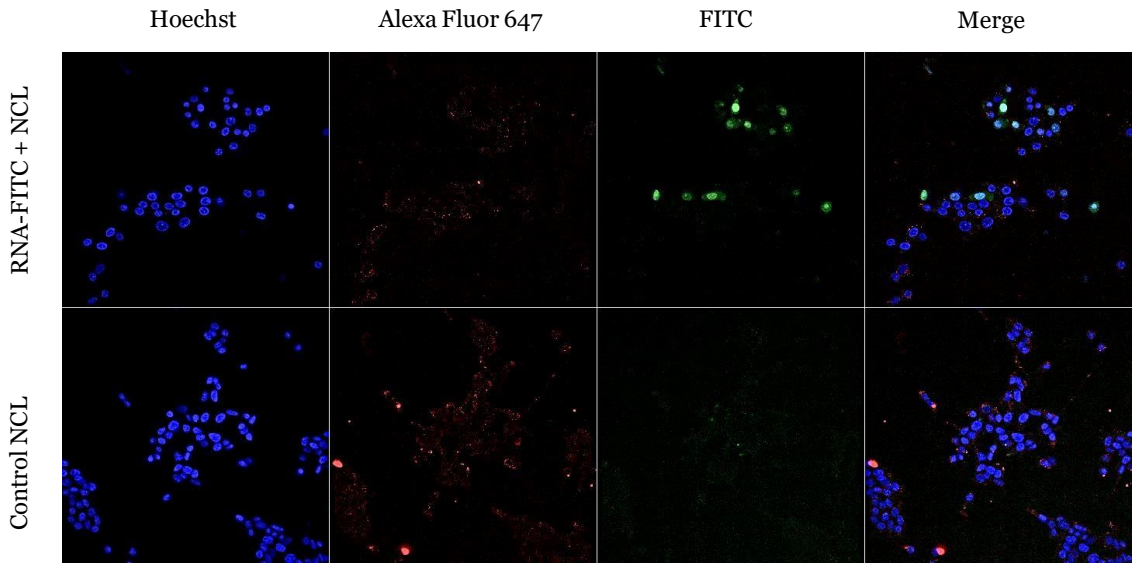

Figure 35 – Confocal microscopy images of SCC-154 cells with 10 μM of RNA-FITC (green). The nuclear probes used were the Hoechst 33342 (blue) and NCL was labeled with the primary anti-NCL polyclonal antibody (1:100) and detected with the secondary antibody against IgG conjugated with Alexa Fluor® 647 (1:1000).

Finally, SCC-154 cells were stained with 2 μM of Hoechst, 10 μM of RNA-FITC and 10 μM of CyTRAK orange in order to observe the nucleus and cytoplasm of cells. The images obtained after 2 h are presented in Figure 36.

As show in Figure 36, these results are in agreement with the previously reported in Figure 32, since the RNA was able to internalize the majority of SCC-154 malignant cells after 2 h and are localized in the nucleus and cytoplasm of the cells. Additionally, it was found that CyTRAK orange preferentially stains the nucleus, but also the cytoplasm, and may be a substitute for Hoechst.

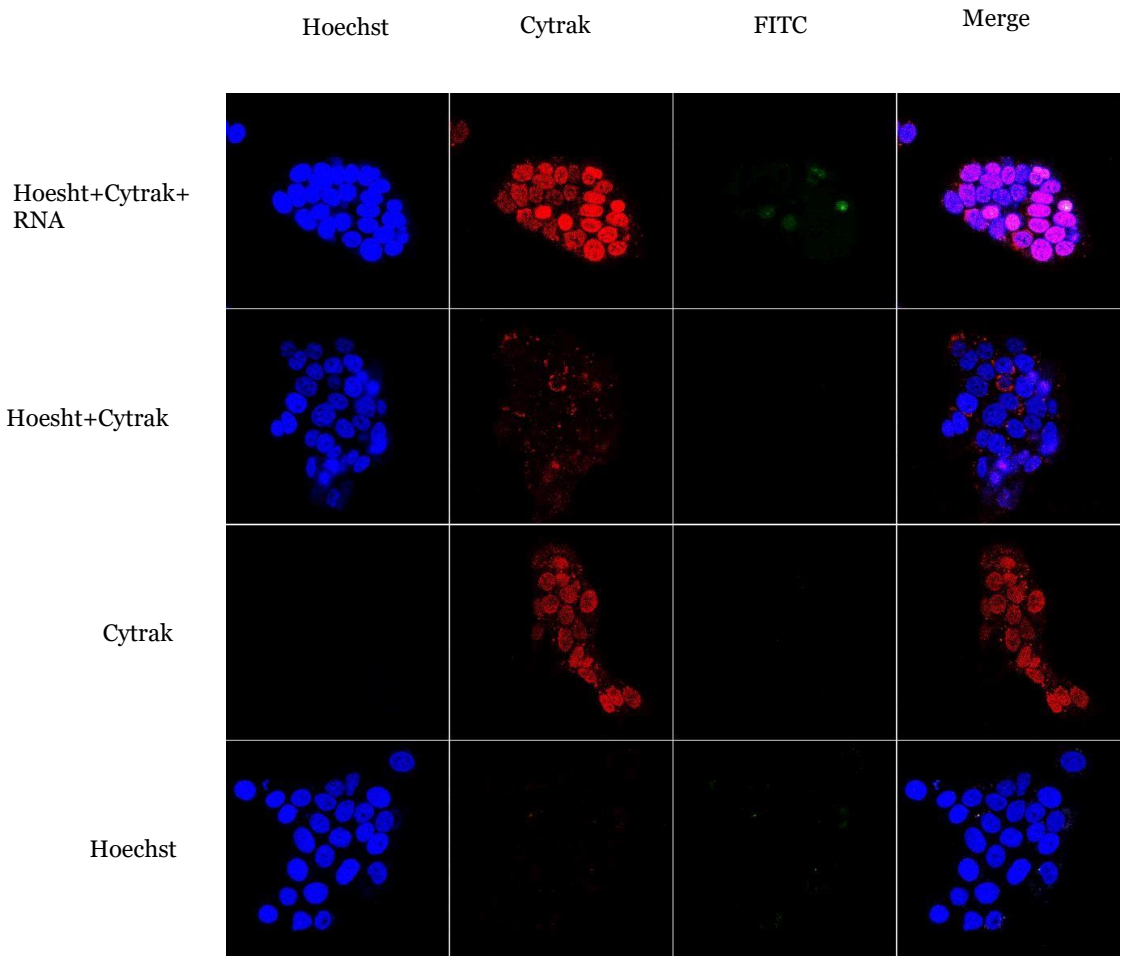

Figure 36 – Confocal microscopy live cell images of SCC-154 cells with 10 μM of RNA-FITC (green). The nuclear probes used were the Hoechst 33342 (blue) and CyTRAK orange (red), who also stains cytoplasm.

Chapter 5

5. Conclusions and Future Perspectives

The search for new targeted anticancer therapeutic approaches is one of the major focus of health science research today[117], [118]. The main objective is to increase the success rate, by targeting cancer cells, without affecting normal tissues, and thereby reducing the side effects associated with conventional therapies, such as chemotherapy, that causes severe toxicity in both normal and malignant tissues [23]. One of the most promising approaches is the application of nanotechnology for cancer therapy.

The purpose of the present work was to develop and characterize RNA-coated nanoparticles, namely liposomes and gold nanoparticles, to selectively deliver the ligands C_8 and dexamethasone to oral cancer.

The biophysical assays evidenced the formation of an RNA hairpin and duplex structure and the ligands C_8 and dexamethasone did not stabilize its structure. It was also shown that the RNA interacts and has a K_D to NCL of 1.80×10^{-6} M, which increases with the addition of C_8 and dexamethasone, with C_8 showing a more pronounced effect.

Regarding the results of the drug delivery systems' characterization, liposomes and gold nanoparticles were effectively coated with the RNA. Additionally, the ligands C_8 and dexamethasone were efficiently encapsulated, in the case of liposomes, and supramolecular assembled, in the case of gold nanoparticles.

Concerning the biological studies, and by performing MTT assay, the ligand C_8 (IC_{50} = 0.22 μM) showed a lower value relative to dexamethasone (IC_{50} = 88.01 μM), in SCC-154 cells, however dexamethasone (IC_{50} = 153.80 μM on NHDF cells) showed greater selectivity for malignant cells relatively to C_8 (IC_{50} = 0.31 μM on NHDF cells). In addition, the RNA did not display any significant effect in the viability of both NHDF and SCC-154 cell lines. The viability assays of the conjugates RNA-C_8 and RNA-dexamethasone, demonstrated in both cell lines, an increase of the cell viability relatively to free C_8 and dexamethasone. Finally, the RNA functionalized liposomes loaded with C_8, or dexamethasone presented a significant reduction in the cell viability of malignant SCC-154 cells, while maintaining viable the non-malignant NHDF cells, thus showing selectivity to malignant cells.

With respect to the confocal fluorescence microscopy assays, the results proved that the RNA was able to internalize the majority of SCC-154 cells after 2 h of incubation, and mainly localize the nucleus and cytoplasm of cells. It was also verified that the RNA did not internalize cells via NCL.

Briefly, the results showed that the C_8 and dexamethasone ligands, despite the non-stabilization of the RNA structure, increase the affinity to NCL and present considerable cytotoxic effect in SCC-154 and NHDF cells. The developed nanosystems, namely the RNA-coated liposomes carrying C_8 and dexamethasone, displayed high cytotoxicity and selectivity for SCC-154 cells in detriment of NHDF cells. Overall, the results of this dissertation can contribute to the development of new drug delivery systems for sustained and effective targeted oral cancer therapy.

Future perspectives include:

- To study the interaction between RNA and the ligands C_8 and dexamethasone by fluorescence anisotropy technique.
- To determine the mechanism of internalization of RNA-coated liposomes and the release of ligands (C_8 and dexamethasone) by incubating SCC-154 cells with the RNA-coated liposomes loading C_8 and dexamethasone and live imaging cells by confocal microscopy.
- To analyze the effect of determined proteins, such as P53 and PD-L1, before and after application of drug delivery systems by western blot technique in cancer and non-malignant cells.

6. References

[1] A. G. Knudson, "Cancer genetics," *Am. J. Med. Genet.*, vol. 111, no. 1, pp. 96–102, 2002, doi: 10.1002/ajmg.10320.

[2] R. De Souza, P. Zahedi, C. J. Allen, and M. Piquette-Miller, "Polymeric drug delivery systems for localized cancer chemotherapy," *Drug Deliv.*, vol. 17, no. 6, pp. 365–375, 2010, doi: 10.3109/10717541003762854.

[3] H. Sung *et al.*, "Global Cancer Statistics 2020: GLOBOCAN Estimates of Incidence and Mortality Worldwide for 36 Cancers in 185 Countries," *CA. Cancer J. Clin.*, vol. 71, no. 3, pp. 209–249, 2021, doi: 10.3322/caac.21660.

[4] M. Crawford, E. H. Johnson, K. Y. P. Liu, C. Poh, and R. Y. L. Tsai, "On the Cutting Edge of Oral Cancer Prevention: Finding Risk-Predictive Markers in Precancerous Lesions by Longitudinal Studies," *Cells*, vol. 11, no. 6, 2022, doi: 10.3390/cells11061033.

[5] D. I. Conway, M. Purkayastha, and I. G. Chestnutt, "The changing epidemiology of oral cancer: Definitions, trends, and risk factors," *Br. Dent. J.*, vol. 225, no. 9, p. 867, 2018, doi: 10.1038/sj.bdj.2018.922.

[6] B. F. Ferlay J, Laversanne M, Ervik M, Lam F, Colombet M, Mery L, Piñeros M, Znaor A, Soerjomataram I, "Global Cancer Observatory: Cancer Tomorrow," *Lyon, France: International Agency for Research on Cancer.*, 2020. https://gco.iarc.fr/tomorrow.

[7] T. Tanaka, M. Tanaka, and T. Tanaka, "Oral Carcinogenesis and Oral Cancer Chemoprevention: A Review," *Patholog. Res. Int.*, vol. 2011, pp. 1–10, 2011, doi: 10.4061/2011/431246.

[8] K. Matsuo and J. B. Palmer, "Anatomy and Physiology of Feeding and Swallowing: Normal and Abnormal," *Phys. Med. Rehabil. Clin. N. Am.*, vol. 19, no. 4, pp. 691–707, 2008, doi: 10.1016/j.pmr.2008.06.001.

[9] C. Rivera, "Essentials of oral cancer," *Int. J. Clin. Exp. Pathol.*, vol. 8, no. 9, pp. 11884–11894, 2015.

[10] G. Calixto, J. Bernegossi, B. Fonseca-Santos, and M. Chorilli, "Nanotechnology-based drug delivery systems for treatment of oral cancer: A review," *Int. J. Nanomedicine*, vol. 9, no. 1, pp. 3719–3735, 2014, doi: 10.2147/IJN.S61670.

[11] J. Bagan, G. Sarrion, and Y. Jimenez, "Oral cancer: Clinical features," *Oral Oncol.*, vol. 46, no. 6, pp. 414–417, 2010, doi: 10.1016/j.oraloncology.2010.03.009.

[12] M. Kumar, R. Nanavati, T. Modi, and C. Dobariya, "Oral cancer: Etiology and risk factors: A review," *J. Cancer Res. Ther.*, vol. 12, no. 2, p. 458, 2016, doi: 10.4103/0973-1482.186696.

[13] M. Keshavarzi *et al.*, "Molecular Imaging and Oral Cancer Diagnosis and Therapy," *J. Cell. Biochem.*, vol. 118, no. 10, pp. 3055–3060, 2017, doi: 10.1002/jcb.26042.

[14] S. D. da Silva, M. Hier, A. Mlynarek, L. P. Kowalski, and M. A. Alaoui-Jamali, "Recurrent oral cancer: Current and emerging therapeutic approaches," *Front. Pharmacol.*, vol. 3 JUL, no. July, pp. 1–7, 2012, doi: 10.3389/fphar.2012.00149.

[15] M. G. Kato *et al.*, "Update on oral and oropharyngeal cancer staging – International perspectives," *World J. Otorhinolaryngol. - Head Neck Surg.*, vol. 6, no. 1, pp. 66–75, 2020, doi: 10.1016/j.wjorl.2019.06.001.

[16] and R. S. Gross ND, Lee NY, Okuno S, "The oral cavity. Brockstein BE, Brizel SM, Posner MR and Fried MP, eds. Waltham, MA: UpToDate Inc.," *Treatment of early (stage I and II) head and neck cancer: The oral cavity.*, 2020. .

[17] A. K. Sah, A. Vyas, P. K. Suresh, and B. Gidwani, "Application of nanocarrier-based drug delivery system in treatment of oral cancer," *Artif. Cells, Nanomedicine Biotechnol.*, vol. 46, no. 4, pp. 650–657, 2018, doi: 10.1080/21691401.2017.1373284.

[18] F. Ketabat *et al.*, "Controlled drug delivery systems for oral cancer treatment—current status and future perspectives," *Pharmaceutics*, vol. 11, no. 7, pp. 1–29, 2019, doi: 10.3390/pharmaceutics11070302.

[19] R. M. Satava, "Emerging technologies for surgery in the 21st century.," *Arch. Surg.*, vol. 134, no. 11, pp. 1197–1202, Nov. 1999, doi: 10.1001/archsurg.134.11.1197.

[20] Y. Hussain, L. Islam, H. Khan, R. Filosa, M. Aschner, and S. Javed, "Curcumin–cisplatin chemotherapy: A novel strategy in promoting chemotherapy efficacy and reducing side effects," *Phyther. Res.*, vol. 35, no. 12, pp. 6514–6529, 2021, doi: https://doi.org/10.1002/ptr.7225.

[21] L. Barazzuol, R. P. Coppes, and P. Luijk, "Prevention and treatment of radiotherapy-induced side effects," *Mol. Oncol.*, vol. 14, no. 7, pp. 1538–1554, Jul. 2020, doi: 10.1002/1878-0261.12750.

[22] S. P. Mohan, M. K. Bhaskaran, A. L. George, A. Thirutheri, M. Somasundaran, and A. Pavithran, "Immunotherapy in Oral Cancer.," *J. Pharm. Bioallied Sci.*, vol. 11, no. Suppl 2, pp. S107–S111, May 2019, doi: 10.4103/JPBS.JPBS_31_19.

[23] Z. Edis, J. Wang, M. K. Waqas, M. Ijaz, and M. Ijaz, "Nanocarriers-mediated drug delivery systems for anticancer agents: An overview and perspectives," *Int. J. Nanomedicine*, vol. 16, pp. 1313–1330, 2021, doi: 10.2147/IJN.S289443.

[24] M. Chamundeeswari, J. Jeslin, and M. L. Verma, “Nanocarriers for drug delivery applications,” *Environ. Chem. Lett.*, vol. 17, no. 2, pp. 849–865, 2019, doi: 10.1007/s10311-018-00841-1.

[25] D. Guimarães, A. Cavaco-Paulo, and E. Nogueira, “Design of liposomes as drug delivery system for therapeutic applications,” *Int. J. Pharm.*, vol. 601, no. February, 2021, doi: 10.1016/j.ijpharm.2021.120571.

[26] Y. (Chezy) Barenholz, “Doxil® — The first FDA-approved nano-drug: Lessons learned,” *J. Control. Release*, vol. 160, no. 2, pp. 117–134, 2012, doi: https://doi.org/10.1016/j.jconrel.2012.03.020.

[27] K. J. O’Byrne *et al.*, “A phase I dose-escalating study of DaunoXome, liposomal daunorubicin, in metastatic breast cancer.,” *Br. J. Cancer*, vol. 87, no. 1, pp. 15–20, Jul. 2002, doi: 10.1038/sj.bjc.6600344.

[28] B. Salehi *et al.*, “Liposomal cytarabine as cancer therapy: From chemistry to medicine,” *Biomolecules*, vol. 9, no. 12, pp. 1–19, 2019, doi: 10.3390/biom9120773.

[29] J. Zhang *et al.*, “Paclitaxel liposome for injection (Lipusu) plus cisplatin versus gemcitabine plus cisplatin in the first-line treatment of locally advanced or metastatic lung squamous cell carcinoma: A multicenter, randomized, open-label, parallel controlled clinical st,” *Cancer Commun. (London, England)*, vol. 42, no. 1, pp. 3–16, Jan. 2022, doi: 10.1002/cac2.12225.

[30] K. Ando, K. Mori, N. Corradini, F. Redini, and D. Heymann, “Mifamurtide for the treatment of nonmetastatic osteosarcoma.,” *Expert Opin. Pharmacother.*, vol. 12, no. 2, pp. 285–292, Feb. 2011, doi: 10.1517/14656566.2011.543129.

[31] J. A. Silverman and S. R. Deitcher, “Marqibo® (vincristine sulfate liposome injection) improves the pharmacokinetics and pharmacodynamics ofvincristine.,” *Cancer Chemother. Pharmacol.*, vol. 71, no. 3, pp. 555–564, Mar. 2013, doi: 10.1007/s00280-012-2042-4.

[32] C. E. Swenson, W. R. Perkins, P. Roberts, and A. S. Janoff, “Liposome technology and the development of Myocet™ (liposomal doxorubicin citrate),” *The Breast*, vol. 10, pp. 1–7, 2001, doi: https://doi.org/10.1016/S0960-9776(01)80001-1.

[33] J. E. Frampton, “Liposomal Irinotecan: A Review in Metastatic Pancreatic Adenocarcinoma.,” *Drugs*, vol. 80, no. 10, pp. 1007–1018, Jul. 2020, doi: 10.1007/s40265-020-01336-6.

[34] K. Sztandera, M. Gorzkiewicz, and B. Klajnert-Maculewicz, “Gold Nanoparticles in Cancer Treatment,” *Mol. Pharm.*, vol. 16, no. 1, pp. 1–23, Jan. 2019, doi: 10.1021/acs.molpharmaceut.8b00810.

[35] C. Boyoglu *et al.*, "Microscopic Studies of Various Sizes of Gold Nanoparticles and Their Cellular Localizations," *ISRN Nanotechnol.*, vol. 2013, pp. 1–13, 2013, doi: 10.1155/2013/123838.

[36] P. K. Sadhu *et al.*, "A combined approach of gold nanoparticles with cannabinoids for the treatment of cancer – a review," *Int. J. Pharm. Res.*, vol. 12, no. August, pp. 393–405, 2020, doi: 10.31838/ijpr/2020.SP1.077.

[37] B. Asadishad, M. Vossoughi, and I. Alemzadeh, "Folate-Receptor-Targeted Delivery of Doxorubicin Using Polyethylene Glycol-Functionalized Gold Nanoparticles," *Ind. Eng. Chem. Res.*, vol. 49, no. 4, pp. 1958–1963, Feb. 2010, doi: 10.1021/ie9011479.

[38] B. Kim, G. Han, B. J. Toley, C.-K. Kim, V. M. Rotello, and N. S. Forbes, "Tuning payload delivery in tumour cylindroids using gold nanoparticles.," *Nat. Nanotechnol.*, vol. 5, no. 6, pp. 465–472, Jun. 2010, doi: 10.1038/nnano.2010.58.

[39] F. Wang, Y.-C. Wang, S. Dou, M.-H. Xiong, T.-M. Sun, and J. Wang, "Doxorubicin-tethered responsive gold nanoparticles facilitate intracellular drug delivery for overcoming multidrug resistance in cancer cells.," *ACS Nano*, vol. 5, no. 5, pp. 3679–3692, May 2011, doi: 10.1021/nn200007z.

[40] M. Prabaharan, J. J. Grailer, S. Pilla, D. A. Steeber, and S. Gong, "Gold nanoparticles with a monolayer of doxorubicin-conjugated amphiphilic block copolymer for tumor-targeted drug delivery.," *Biomaterials*, vol. 30, no. 30, pp. 6065–6075, Oct. 2009, doi: 10.1016/j.biomaterials.2009.07.048.

[41] Y.-J. Gu, J. Cheng, C. W.-Y. Man, W.-T. Wong, and S. H. Cheng, "Gold-doxorubicin nanoconjugates for overcoming multidrug resistance.," *Nanomedicine*, vol. 8, no. 2, pp. 204–211, Feb. 2012, doi: 10.1016/j.nano.2011.06.005.

[42] J. Li *et al.*, "The enhancement effect of gold nanoparticles in drug delivery and as biomarkers of drug-resistant cancer cells.," *ChemMedChem*, vol. 2, no. 3, pp. 374–378, Mar. 2007, doi: 10.1002/cmdc.200600264.

[43] G. F. Paciotti *et al.*, "Colloidal gold: a novel nanoparticle vector for tumor directed drug delivery.," *Drug Deliv.*, vol. 11, no. 3, pp. 169–183, 2004, doi: 10.1080/10717540490433895.

[44] E. C. Dreaden, S. C. Mwakwari, Q. H. Sodji, A. K. Oyelere, and M. A. El-Sayed, "Tamoxifen-poly(ethylene glycol)-thiol gold nanoparticle conjugates: enhanced potency and selective delivery for breast cancer treatment.," *Bioconjug. Chem.*, vol. 20, no. 12, pp. 2247–2253, Dec. 2009, doi: 10.1021/bc9002212.

[45] Y.-H. Chen *et al.*, "Methotrexate conjugated to gold nanoparticles inhibits tumor growth in a syngeneic lung tumor model.," *Mol. Pharm.*, vol. 4, no. 5, pp. 713–722, 2007, doi: 10.1021/mp060132k.

[46] C. R. Patra *et al.*, "Targeted delivery of gemcitabine to pancreatic adenocarcinoma using cetuximab as a targeting agent.," *Cancer Res.*, vol. 68, no. 6, pp. 1970–1978, Mar. 2008, doi: 10.1158/0008-5472.CAN-07-6102.

[47] P. Podsiadlo, V. A. Sinani, J. H. Bahng, N. W. S. Kam, J. Lee, and N. A. Kotov, "Gold nanoparticles enhance the anti-leukemia action of a 6-mercaptopurine chemotherapeutic agent.," *Langmuir*, vol. 24, no. 2, pp. 568–574, Jan. 2008, doi: 10.1021/la702782k.

[48] S. S. Agasti, A. Chompoosor, C.-C. You, P. Ghosh, C. K. Kim, and V. M. Rotello, "Photoregulated Release of Caged Anticancer Drugs from Gold Nanoparticles," *J. Am. Chem. Soc.*, vol. 131, no. 16, pp. 5728–5729, Apr. 2009, doi: 10.1021/ja900591t.

[49] E. M. S. Azzam and S. M. I. Morsy, "Enhancement of the antitumour activity for the synthesised dodecylcysteine surfactant using gold nanoparticles," *J. Surfactants Deterg.*, vol. 11, no. 3, pp. 195–199, 2008, doi: 10.1007/s11743-008-1072-8.

[50] M. Stiti *et al.*, "Carbonic Anhydrase Inhibitor Coated Gold Nanoparticles Selectively Inhibit the Tumor-Associated Isoform IX over the Cytosolic Isozymes I and II," *J. Am. Chem. Soc.*, vol. 130, no. 48, pp. 16130–16131, Dec. 2008, doi: 10.1021/ja805558k.

[51] L. Hosta *et al.*, "Conjugation of Kahalalide F with Gold Nanoparticles to Enhance in Vitro Antitumoral Activity," *Bioconjug. Chem.*, vol. 20, no. 1, pp. 138–146, Jan. 2009, doi: 10.1021/bc800362j.

[52] S. Dhar, W. L. Daniel, D. A. Giljohann, C. A. Mirkin, and S. J. Lippard, "Polyvalent Oligonucleotide Gold Nanoparticle Conjugates as Delivery Vehicles for Platinum(IV) Warheads," *J. Am. Chem. Soc.*, vol. 131, no. 41, pp. 14652–14653, Oct. 2009, doi: 10.1021/ja9071282.

[53] M. E. Wieder, D. C. Hone, M. J. Cook, M. M. Handsley, J. Gavrilovic, and D. A. Russell, "Intracellular photodynamic therapy with photosensitizer-nanoparticle conjugates: cancer therapy using a 'Trojan horse'.," *Photochem. Photobiol. Sci. Off. J. Eur. Photochem. Assoc. Eur. Soc. Photobiol.*, vol. 5, no. 8, pp. 727–734, Aug. 2006, doi: 10.1039/b602830f.

[54] B. Wang *et al.*, "Rose-bengal-conjugated gold nanorods for in vivo photodynamic and photothermal oral cancer therapies.," *Biomaterials*, vol. 35, no. 6, pp. 1954–1966, Feb. 2014, doi: 10.1016/j.biomaterials.2013.11.066.

[55] K. Endo *et al.*, "Tumor-targeted chemotherapy with the nanopolymer-based drug NC-6004 for oral squamous cell carcinoma," *Cancer Sci.*, vol. 104, no. 3, pp. 369–374, 2013, doi: 10.1111/cas.12079.

[56] L. Mazzarino *et al.*, "Curcumin-Loaded Chitosan-Coated Nanoparticles as a New Approach for the Local Treatment of Oral Cavity Cancer.," *J. Nanosci. Nanotechnol.*, vol. 15, no. 1, pp. 781–791, Jan. 2015, doi: 10.1166/jnn.2015.9189.

[57] I. H. El-Sayed, X. Huang, and M. A. El-Sayed, "Selective laser photo-thermal therapy of epithelial carcinoma using anti-EGFR antibody conjugated gold nanoparticles," *Cancer Lett.*, vol. 239, no. 1, pp. 129–135, 2006, doi: https://doi.org/10.1016/j.canlet.2005.07.035.

[58] S. S. Lucky *et al.*, "In vivo biocompatibility, biodistribution and therapeutic efficiency of titania coated upconversion nanoparticles for photodynamic therapy of solid oral cancers," *Theranostics*, vol. 6, no. 11, pp. 1844–1865, 2016, doi: 10.7150/thno.15088.

[59] D. Wang *et al.*, "Codelivery of doxorubicin and MDR1-siRNA by mesoporous silica nanoparticles-polymerpolyethylenimine to improve oral squamous carcinoma treatment.," *Int. J. Nanomedicine*, vol. 13, pp. 187–198, 2018, doi: 10.2147/IJN.S150610.

[60] J. Paulo, F. Longo, L. A. Muehlmann, N. V. Velloso, A. R. Simioni, and S. P. Lozzi, "Effects of Photodynamic Therapy Mediated by Liposomal Aluminumphthalocyanine Chloride on Chemically Induced Tongue Tumors," *Chemother. Open Access*, vol. 01, no. 02, pp. 2–5, 2012, doi: 10.4172/2167-7700.1000103.

[61] L. A. Muehlmann, "Aluminum-Phthalocyanine Chloride-Based Photodynamic Therapy Inhibits PI3K/Akt/Mtorpathway In Oral Squamous Cell Carcinoma Cells In Vitro," *Chemother. Open Access*, vol. 01, no. 05, pp. 1–5, 2012, doi: 10.4172/2167-7700.100107.

[62] M. J. Moura, M. H. Gil, and M. M. Figueiredo, "Delivery of cisplatin from thermosensitive co-cross-linked chitosan hydrogels," *Eur. Polym. J.*, vol. 49, no. 9, pp. 2504–2510, 2013, doi: https://doi.org/10.1016/j.eurpolymj.2013.02.032.

[63] J. Li *et al.*, "Biodegradable thermosensitive hydrogel for SAHA and DDP delivery: Therapeutic effects on oral squamous cell carcinoma xenografts," *PLoS One*, vol. 7, no. 4, pp. 2–9, 2012, doi: 10.1371/journal.pone.0033860.

[64] H. Shi *et al.*, "Au@Ag/Au nanoparticles assembled with activatable aptamer probes as smart 'nano-doctors' for image-guided cancer thermotherapy," *Nanoscale*, vol. 6, no. 15, pp. 8754–8761, 2014, doi: 10.1039/c4nr01927j.

[65] S. Menon, R. S., and V. K. S., "A review on biogenic synthesis of gold nanoparticles, characterization, and its applications," *Resour. Technol.*, vol. 3, no. 4, pp. 516–527, 2017, doi: 10.1016/j.reffit.2017.08.002.

[66] J. Han, L. Gao, J. Wang, and J. Wang, "Application and development of aptamer in cancer: From clinical diagnosis to cancer therapy," *J. Cancer*, vol. 11, no. 23, pp. 6902–6915, 2020, doi: 10.7150/JCA.49532.

[67] S. A. Moosavian and A. Sahebkar, "Aptamer-functionalized liposomes for targeted cancer therapy," *Cancer Lett.*, vol. 448, no. September 2018, pp. 144–154, 2019, doi: 10.1016/j.canlet.2019.01.045.

[68] H. Ma *et al.*, "Nucleic acid aptamers in cancer research, diagnosis and therapy," *Chem. Soc. Rev.*, vol. 44, no. 5, pp. 1240–1256, 2015, doi: 10.1039/c4cs00357h.

[69] C. Kratschmer and M. Levy, "Effect of Chemical Modifications on Aptamer Stability in Serum," *Nucleic Acid Ther.*, vol. 27, no. 6, pp. 335–344, 2017, doi: 10.1089/nat.2017.0680.

[70] M. Darmostuk, S. Rimpelova, H. Gbelcova, and T. Ruml, "Current approaches in SELEX: An update to aptamer selection technology," *Biotechnol. Adv.*, vol. 33, no. 6, Part 2, pp. 1141–1161, 2015, doi: https://doi.org/10.1016/j.biotechadv.2015.02.008.

[71] D. Xiang *et al.*, "Nucleic acid aptamer-guided cancer therapeutics and diagnostics: The next generation of cancer medicine," *Theranostics*, vol. 5, no. 1, pp. 23–42, 2015, doi: 10.7150/thno.10202.

[72] D. R. Gutsaeva *et al.*, "Inhibition of cell adhesion by anti-P-selectin aptamer: A new potential therapeutic agent for sickle cell disease," *Blood*, vol. 117, no. 2, pp. 727–735, 2011, doi: 10.1182/blood-2010-05-285718.

[73] S. Santulli-Marotto, S. K. Nair, C. Rusconi, B. Sullenger, and E. Gilboa, "Multivalent RNA Aptamers That Inhibit CTLA-4 and Enhance Tumor Immunity," *Cancer Res.*, vol. 63, no. 21, pp. 7483–7489, 2003.

[74] A. S. Barbas, J. Mi, B. M. Clary, and R. R. White, "Aptamer applications for targeted cancer therapy," *Futur. Oncol.*, vol. 6, no. 7, pp. 1117–1126, 2010, doi: 10.2217/fon.10.67.

[75] W. Jia, Z. Yao, J. Zhao, Q. Guan, and L. Gao, "New perspectives of physiological and pathological functions of nucleolin (NCL)," *Life Sci.*, vol. 186, no. July, pp. 1–10, Oct. 2017, doi: 10.1016/j.lfs.2017.07.025.

[76] X. Guo *et al.*, "Increased level of nucleolin confers to aggressive tumor progression and poor prognosis in patients with hepatocellular carcinoma after hepatectomy," *Diagn. Pathol.*, vol. 9, no. 1, p. 175, Dec. 2014, doi: 10.1186/s13000-014-0175-y.

[77] E. W. M. Ng, D. T. Shima, P. Calias, E. T. Cunningham, D. R. Guyer, and A. P. Adamis, “Pegaptanib, a targeted anti-VEGF aptamer for ocular vascular disease,” *Nat. Rev. Drug Discov.*, vol. 5, no. 2, pp. 123–132, Feb. 2006, doi: 10.1038/nrd1955.

[78] D. Zboralski, K. Hoehlig, D. Eulberg, A. Frömming, and A. Vater, “Increasing tumor-infiltrating T cells through inhibition of CXCL12 with NOX-A12 synergizes with PD-1 blockade,” *Cancer Immunol. Res.*, vol. 5, no. 11, pp. 950–956, 2017, doi: 10.1158/2326-6066.CIR-16-0303.

[79] S. C. Simmons *et al.*, “Anti-heparanase aptamers as potential diagnostic and therapeutic agents for oral cancer,” *PLoS One*, vol. 9, no. 10, 2014, doi: 10.1371/journal.pone.0096846.

[80] C. Y. Wang, B. L. Lin, and C. H. Chen, “An aptamer targeting shared tumor-specific peptide antigen of MAGE-A3 in multiple cancers,” *Int. J. Cancer*, vol. 138, no. 4, pp. 918–926, 2016, doi: 10.1002/ijc.29826.

[81] H. J. Sung *et al.*, “Inhibition of human neutrophil activity by an RNA aptamer bound to interleukin-8,” *Biomaterials*, vol. 35, no. 1, pp. 578–589, Jan. 2014, doi: 10.1016/j.biomaterials.2013.09.107.

[82] F. Schmid, “Biological Macromolecules: UV-visible Spectrophotometry,” in *eLS*, Wiley, 2001, pp. 1–4.

[83] J. L. Mergny, J. Li, L. Lacroix, S. Amrane, and J. B. Chaires, “Thermal difference spectra: A specific signature for nucleic acid structures,” *Nucleic Acids Res.*, vol. 33, no. 16, pp. 1–6, 2005, doi: 10.1093/nar/gni134.

[84] T. Santos *et al.*, “Stabilization of a DNA aptamer by ligand binding,” *Biochimie*, vol. 200, pp. 8–18, 2022, doi: 10.1016/j.biochi.2022.05.002.

[85] A. J. Miles, R. W. Janes, and B. A. Wallace, “Tools and methods for circular dichroism spectroscopy of proteins: A tutorial review,” *Chem. Soc. Rev.*, vol. 50, no. 15, pp. 8400–8413, 2021, doi: 10.1039/d0cs00558d.

[86] D. Psimadas, P. Georgoulias, V. Valotassiou, and G. Loudos, “Molecular Nanomedicine Towards Cancer :,” *J. Pharm. Sci.*, vol. 101, no. 7, pp. 2271–2280, 2012, doi: 10.1002/jps.

[87] J. Carvalho, J. A. Queiroz, and C. Cruz, “Circular dichroism of G-Quadruplex: A laboratory experiment for the study of topology and ligand binding,” *J. Chem. Educ.*, vol. 94, no. 10, pp. 1547–1551, 2017, doi: 10.1021/acs.jchemed.7b00160.

[88] D. Yang and C. Lin, *G-Quadruplex Nucleic Acids Methods and Protocols Methods in Molecular Biology 2035*. .

[89] V. Mlynárik, “Introduction to nuclear magnetic resonance,” *Anal. Biochem.*, vol. 529, pp. 4–9, 2017, doi: 10.1016/j.ab.2016.05.006.

[90] B. Fürtig, C. Richter, J. Wöhnert, and H. Schwalbe, “NMR spectroscopy of RNA,” *ChemBioChem*, vol. 4, no. 10, pp. 936–962, 2003, doi: 10.1002/cbic.200300700.

[91] H. Šípová and J. Homola, “Surface plasmon resonance sensing of nucleic acids: A review,” *Anal. Chim. Acta*, vol. 773, pp. 9–23, 2013, doi: 10.1016/j.aca.2012.12.040.

[92] O. R. Ciobotaru *et al.*, “Dexamethasone - Chemical structure and mechanisms of action in prophylaxis of postoperative side effects,” *Rev. Chim.*, vol. 70, no. 3, pp. 843–847, 2019, doi: 10.37358/rc.19.3.7017.

[93] L. Wang, W. Lu, and T. Zhou, “[Current applications of dexamethasone for cancer treatment],” *Yao Xue Xue Bao*, vol. 50, no. 10, p. 1217—1224, 2015, [Online]. Available: http://europepmc.org/abstract/MED/26837165.

[94] M. Beppu, T. Ikebe, and K. Shirasuna, “The inhibitory effects of immunosuppressive factors, dexamethasone and interleukin-4, on NF-κB-mediated protease production by oral cancer,” *Biochim. Biophys. Acta - Mol. Basis Dis.*, vol. 1586, no. 1, pp. 11–22, 2002, doi: 10.1016/S0925-4439(01)00080-1.

[95] T. Shiratsuchi, H. Ishibashi, and K. Shirasuna, “Inhibition of epidermal growth factor-induced invasion by dexamethasone and AP-1 decoy in human squamous cell carcinoma cell lines,” *J. Cell. Physiol.*, vol. 193, no. 3, pp. 340–348, 2002, doi: 10.1002/jcp.10181.

[96] A. Duarte, J. F. Mano, and R. L. Reis, “Preparation of chitosan scaffolds loaded with dexamethasone for tissue engineering applications using supercritical fluid technology,” *Eur. Polym. J.*, vol. 45, pp. 141–148, Jan. 2009, doi: 10.1016/j.eurpolymj.2008.10.004.

[97] J. Carvalho *et al.*, “Fluorescent light-up acridine orange derivatives bind and stabilize KRAS-22RT G-quadruplex,” *Biochimie*, vol. 144, pp. 144–152, 2018, doi: 10.1016/j.biochi.2017.11.004.

[98] E. Pereira *et al.*, “Evaluation of Acridine Orange Derivatives as DNA-Targeted Radiopharmaceuticals for Auger Therapy: Influence of the Radionuclide and Distance to DNA,” *Sci. Rep.*, vol. 7, no. February, pp. 1–16, 2017, doi: 10.1038/srep42544.

[99] M. T. Malik *et al.*, “AS1411-conjugated gold nanospheres and their potential for breast cancer therapy,” *Oncotarget*, vol. 6, no. 26, pp. 22270–22281, 2015, doi: 10.18632/oncotarget.4207.

[100] V. Filipe, A. Hawe, and W. Jiskoot, “Critical evaluation of nanoparticle tracking analysis (NTA) by NanoSight for the measurement of nanoparticles and protein aggregates,” *Pharm. Res.*, vol. 27, no. 5, pp. 796–810, 2010, doi: 10.1007/s11095-010-0073-2.

[101] M. L. B. Magalhães *et al.*, “A general RNA motif for cellular transfection,” *Mol. Ther.*, vol. 20, no. 3, pp. 616–624, 2012, doi: 10.1038/mt.2011.277.

[102] J. O. Trent, J. B. Chaires, J. Graham, and B. Cancer, “spectroscopy,” vol. 57, no. 24, pp. 7171–7175, 2019, doi: 10.1002/anie.201709184.G-quadruplex.

[103] S. Campagne, V. Gervais, and A. Milon, “Nuclear magnetic resonance analysis of protein-DNA interactions,” *J. R. Soc. Interface*, vol. 8, no. 61, pp. 1065–1078, 2011, doi: 10.1098/rsif.2010.0543.

[104] M. Danaei *et al.*, “Impact of particle size and polydispersity index on the clinical applications of lipidic nanocarrier systems,” *Pharmaceutics*, vol. 10, no. 2, pp. 1–17, 2018, doi: 10.3390/pharmaceutics10020057.

[105] J. Lopes-Nunes *et al.*, “Aptamer-functionalized gold nanoparticles for drug delivery to gynecological carcinoma cells,” *Cancers (Basel).*, vol. 13, no. 16, 2021, doi: 10.3390/cancers13164038.

[106] Z. Cao *et al.*, “Reversible cell-specific drug delivery with aptamer-functionalized liposomes,” *Angew. Chemie - Int. Ed.*, vol. 48, no. 35, pp. 6494–6498, 2009, doi: 10.1002/anie.200901452.

[107] H. Xing *et al.*, “Selective delivery of an anticancer drug with aptamer-functionalized liposomes to breast cancer cells in vitro and in vivo,” *J. Mater. Chem. B*, vol. 1, no. 39, pp. 5288–5297, 2013, doi: 10.1039/c3tb20412j.

[108] Z. X. Liao *et al.*, “An AS1411 aptamer-conjugated liposomal system containing a bubble-generating agent for tumor-specific chemotherapy that overcomes multidrug resistance,” *J. Control. Release*, vol. 208, pp. 42–51, 2015, doi: 10.1016/j.jconrel.2015.01.032.

[109] J. C. M. Stewart, “Colorimetric determination of phospholipids with ammonium ferrothiocyanate,” *Anal. Biochem.*, vol. 104, no. 1, pp. 10–14, 1980, doi: 10.1016/0003-2697(80)90269-9.

[110] A. Nag, G. Mitra, and P. C. Ghosh, “A Colorimetric Estimation of Polyethyleneglycol-conjugated PL.pdf,” vol. 43, no. 250, pp. 35–43, 1997.

[111] J. Carvalho *et al.*, “Aptamer-guided acridine derivatives for cervical cancer.,” *Org. Biomol. Chem.*, vol. 17, no. 11, pp. 2992–3002, Mar. 2019, doi: 10.1039/c9ob00318e.

[112] J. Figueiredo *et al.*, "AS1411 derivatives as carriers of G-quadruplex ligands for cervical cancer cells," *Int. J. Pharm.*, vol. 568, p. 118511, 2019, doi: https://doi.org/10.1016/j.ijpharm.2019.118511.

[113] J. Lopes-Nunes *et al.*, "Aptamer-Functionalized Gold Nanoparticles for Drug Delivery to Gynecological Carcinoma Cells," *Cancers (Basel).*, vol. 13, no. 16, 2021, doi: 10.3390/cancers13164038.

[114] L.-J. Wang *et al.*, "Dexamethasone suppresses the growth of human non-small cell lung cancer via inducing estrogen sulfotransferase and inactivating estrogen.," *Acta Pharmacol. Sin.*, vol. 37, no. 6, pp. 845–856, Jun. 2016, doi: 10.1038/aps.2016.39.

[115] H. S. P., F. Forouzesh, S. M., and M. Aghaei, "Synergistic Anti-proliferative Effects of Lenalidomide and Dexamethasone on the HT-29 Cell Line Through Apoptotic Genes," *Int. J. Cancer Manag.*, vol. 14, no. 8, p. e101811, 2021, doi: 10.5812/ijcm.101811.

[116] J. Carvalho *et al.*, "Aptamer-guided acridine derivatives for cervical cancer," *Org. Biomol. Chem.*, vol. 17, no. 11, pp. 2992–3002, 2019, doi: 10.1039/c90b00318e.

[117] V. M. Khot, A. B. Salunkhe, S. Pricl, J. Bauer, N. D. Thorat, and H. Townley, "Nanomedicine-driven molecular targeting, drug delivery, and therapeutic approaches to cancer chemoresistance," *Drug Discov. Today*, vol. 26, no. 3, pp. 724–739, 2021, doi: https://doi.org/10.1016/j.drudis.2020.12.016.

[118] B. Dutta, K. C. Barick, and P. A. Hassan, "Recent advances in active targeting of nanomaterials for anticancer drug delivery," *Adv. Colloid Interface Sci.*, vol. 296, p. 102509, 2021, doi: https://doi.org/10.1016/j.cis.2021.102509.

Appendixes

Appendix 1 – Accepted manuscripts

1) Figueiredo, J.; Santos, T.; Miranda, A.; Alexandre, D.; Teixeira, B.; Simões, P.; Lopes-Nunes, J.; Cruz, C. Ligands as Stabilizers of G-Quadruplexes in Non-Coding RNAs. Molecules 2021, 26,6164. doi: 10.3390/molecules26206164

Appendix 2 - Presentations of the results of the research work.

Poster Presentations

1) Simões, P.; Lopes-Nunes, J.; Tomaz C.; Cruz, C. Development of RNA Functionalized Nanoparticle for Oral Cancer Therapy. XVI Annual CICS-UBI Symposium (21/07/2021)
2) Simões, P.; Lopes-Nunes, J.; Tomaz C.; Cruz, C. Desenvolvimento de Nanopartículas Funcionalizadas com RNA para Terapia do Cancro Oral. 3º Encontro Nacional de Jovens Investigadores em Oncologia. (24/09/2021)
3) Simões, P.; Lopes-Nunes, J.; Tomaz C.; Cruz, C. Development of RNA functionalized gold nanoparticles for oral cancer therapy. UT-Austin Portugal Annual Conference 2021 (21/10/2021)

Oral Presentations

1) Simões, P.; Lopes-Nunes, J.; Tomaz C.; Cruz, C. RNA-Guided Nanoparticles for Oral Cancer Therapy. XVII Annual CICS-UBI Symposium (21/07/2022)